The Treatment of Volumetric Muscle Loss in a Clinically Relevant Large Animal Model

by

Brittany Lynn Rodriguez

A dissertation submitted in partial fulfillment
of the requirements for the degree of
Doctor of Philosophy
(Biomedical Engineering)
in the University of Michigan
2020

Doctoral Committee:

Professor Lisa M. Larkin, Chair
Professor Susan Brooks Herzog
Associate Research Scientist Dennis Claflin
Associate Professor Ariella Shikanov

Brittany L. Rodriguez

britlrod@umich.edu

ORCID iD: 0000-0003-3738-520X

Acknowledgments

The research in this dissertation was funded by the NIH National Institute of Arthritis and Musculoskeletal and Skin Diseases (1R01AR067744-01), NIH Research Supplement to Promote Diversity in Health-Related Research (3R01AR067744-02W1), and the US Department of Defense (W81XWH-16-1-0752). I would also like to acknowledge the NIH P30 support provided by the Michigan Integrative Musculoskeletal Health Core Center and support provided by the Rackham Graduate School.

Extensive contributions to the experiments in this dissertation were made by the members, past and present, of the Skeletal Tissue Engineering Laboratory at the University of Michigan, under the mentorship of Dr. Lisa Larkin. Specifically, I would like to thank my co-authors, as well as Lisa Larkin, Peggy Hogan, and Peter Macpherson for their mentorship.

Table of Contents

List of Figures

List of Abbreviations

ABAM	Antibiotic-Antimycotic
ADSC	Adipose Derived Stem Cell
ANOVA	Analysis of Variance
BMSC	Bone Marrow-Derived Stem Cell
DEX	Dexamethasone
DMEM	Dulbecco's Modified Eagle's Medium
DMSO	Dimethyl Sulfoxide
DPBS	Dulbecco's phosphate-buffered saline
ECM	Extracellular Matrix
ENC	Engineered Neural Conduit
F12K	Ham's F12 Kaighn's Modification Nutrient Mixture
FAP	Fibro-adipogenic Progenitor
FBS	Fetal Bovine Serum
FDA	Food and Drug Administration
FGFb	Fibroblast Growth Factor Basic
GMP	Good Manufacturing Practices
H&E	Hematoxylin & Eosin
HS	Horse Serum
ITSX	Insulin–Transferrin–Selenium-X
Lo	Optimal Length
Mas	Masseter Muscle
M199	Media 199
MDM	Muscle Differentiation Media
MEP	Motor End Plate
MGM	Muscle Growth Media
MHC	Myosin Heavy Chain
MRF	Myogenic Regulatory Factor
MSC	Mesenchymal Stem Cell
PT	Peroneus Tertius
SM	Semimembranosus Muscle
SMAS	Superficial Musculoaponeurotic System
SMC	Sidak's Multiple Comparisons
SMU	Skeletal Muscle Unit
Sol	Soleus Muscle
TMC	Tukey's Multiple Comparisons
VML	Volumetric Muscle Loss
ZM	Zygomaticus Major Muscle

Abstract

Volumetric muscle loss (VML) is the traumatic or surgical loss of skeletal muscle comprising 20-30% or more of the muscle volume. By definition, VML exceeds the muscle's capacity for self-repair and results in persistent functional deficits. Significantly, no treatment options exist that can fully restore native structure and function. To address the limitations of current treatments, our laboratory has developed tissue-engineered skeletal muscle units (SMUs) as a novel treatment for VML repair. SMUs have shown promising regenerative potential in a rat VML model; however, limitations of rodent models necessitated transitioning our technology to a large animal (sheep) model.

Despite substantial heterogeneity of muscle progenitor cell populations obtained from craniofacial, trunk, and limb muscle, engineered skeletal muscle tissues are almost exclusively fabricated from cells derived from hindlimb muscle, making the effects of cell source on engineered muscle tissue unknown. Thus, we conducted a comparison of the development (myogenesis), structure (histology), and function (biomechanics) of SMUs fabricated from muscle cells isolated from both craniofacial and hindlimb muscle sources. Specifically, we showed that the semimembranosus muscle was best suited for the fabrication of sheep-derived SMUs.

We also sought to develop a method to scale our SMUs to clinically relevant sizes. We developed a modular fabrication method that combines multiple smaller SMUs into a larger implantable graft. Consequently, we successfully fabricated of one of the largest engineered skeletal muscle tissues to date while avoiding the formation of a necrotic core. To treat peripheral

nerve injuries that accompany VML, we also developed engineered neural conduits (ENCs) to bridge gaps between native nerve and the injury site. We used scaled-up SMUs and ENCs to treat a 30% VML in the ovine peroneus tertius muscle. After a 3-month recovery, we performed *in situ* biomechanical testing and histological analyses on explanted muscles. Results showed that SMU-treated groups restored muscle mass and force production to a level that was statistically indistinguishable from the uninjured contralateral muscle.

Lastly, we evaluated the efficacy of SMUs in repairing craniofacial VML. Despite reported differences in the regenerative capacity of craniofacial muscle compared to limb muscle, prior to the work described herein, there were no models of craniofacial VML in either large or small animal models. Thus, we introduced the first model of craniofacial VML and evaluated the ability of SMUs to treat a 30% VML in the zygomaticus major muscle. Despite using the same injury and repair model in both implantation studies, results showed differences in pathophysiology between craniofacial and hindlimb VML. The fibrotic response was greater in the facial muscle model, and there was tissue tethering and intramuscular fat deposition that was not observed in the hindlimb study. The craniofacial model was also confounded by concomitant denervation and ischemia injuries which were too severe for our SMUs to repair.

Overall, this work significantly contributed to the field of skeletal muscle tissue engineering by evaluating the effects of muscle source on the structure and function of SMUs, creating a modular fabrication method for tissue scale-up, and introducing a new large animal model and a craniofacial model of VML. The success of this technology demonstrates its potential for treating clinical VML in the future.

Chapter I – Introduction

Some of the text and figures in this section were originally published as a textbook chapter with the following citation: Rodriguez, B. L., & Larkin, L. M. (2017). Functional three-dimensional scaffolds for skeletal muscle tissue engineering. In Y. Deng & J. Kuiper (Eds.), Functional 3D Tissue Engineering Scaffolds (pp. 279-304): Elsevier [1]. Excerpts from this textbook chapter have been included with permission from the publisher, Elsevier.

Skeletal Muscle Physiology

The Structure of Native Skeletal Muscle

The role of skeletal muscle is to produce force that facilitates movement. When muscle receives a signal from the nervous system, it is stimulated to contract. The force of the contractions is relayed to the skeleton to produce motion or to maintain the skeleton in a certain position. Skeletal muscle consists of several tissue types including muscle fibers, connective tissue, nerve, and vasculature, which are arranged into a highly organized structure that is necessary for skeletal muscle function.

Mature skeletal muscle cells (i.e. muscle fibers) are cylindrical, elongated, and are linearly aligned along the length of the muscle (Figure 1 [2]). A hierarchy of connective tissues integrate the muscle fibers: the endomysium surrounds each muscle fiber, the perimysium encapsulates bundles of muscle fibers into fascicles, and the epimysium envelops the entire muscle. While these connective tissues account for approximately 10% of the muscle volume, muscle fibers account for the remaining 90% [3]. The bulk of each muscle fiber consists of myofibrils which are made

up of an arrangement of contractile protein filaments including actin and myosin. Myofibrils run along the entire length of the muscle fiber and are organized into repeating functional units called sarcomeres. The repeating pattern created by the sarcomeres is visible as striations when skeletal muscle is observed microscopically. Because myofibrils make up the bulk of the cytoplasmic contents of the muscle fiber, the multiple nuclei in a mature muscle fiber are located peripherally, just beneath the muscle fiber cell membrane (i.e. the sarcolemma). In contrast, the nuclei in damaged or diseased muscle are often centrally located [4, 5].

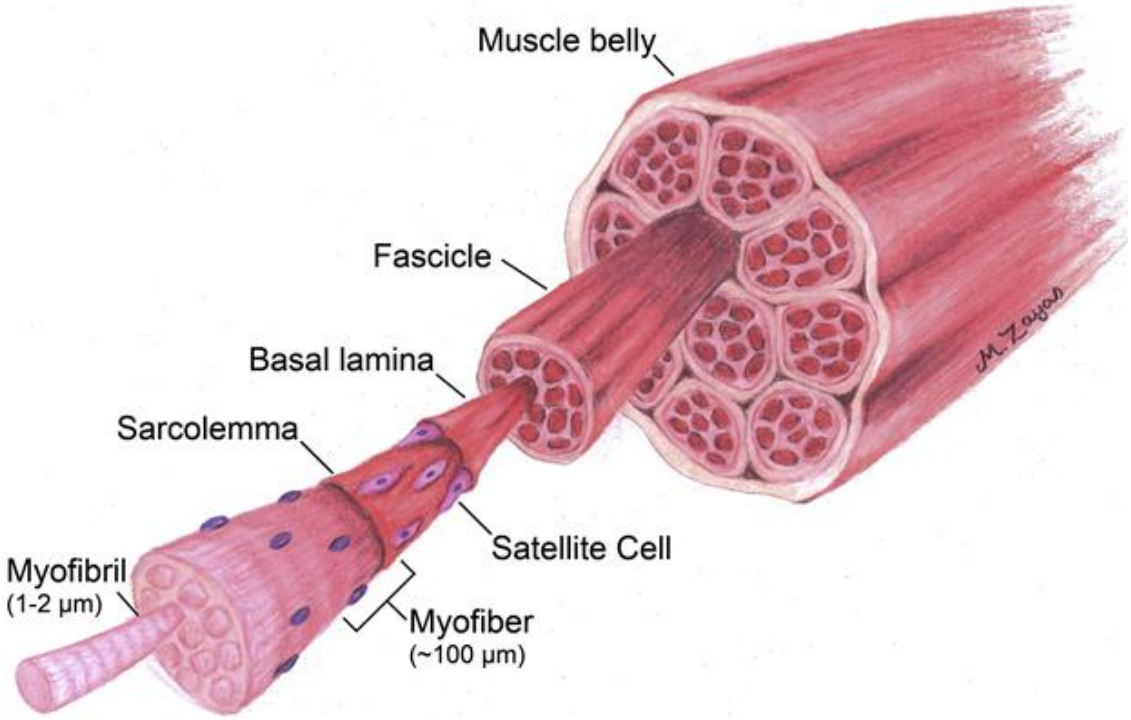

Figure 1. The Structure of Skeletal Muscle.

Muscle is a highly organized, anisotropic tissue. A single muscle cell, called a myofiber, is made of up of bundles of myofibrils that span the length of the cell. Satellite cells are situated adjacent to the myofiber cell membrane, called the sarcolemma. Bundles of myofibers form fascicles which make up the belly of the muscle. Image adapted from Grasman et al. Acta Biomater, 2015 [2] and reproduced with permission from Elsevier.

Mechanical Properties of Native Skeletal Muscle

During movement, the sarcomeres shorten to generate a force parallel to the longitudinal axis of the myofibril. Muscle fibers are either linearly aligned along the force-producing (longitudinal) axis or are oriented at an angle to the axis, called the pennation angle. Muscles in which the fibers have a pennation angle produce 2D force vectors during contraction. The pennation angle increases the functional cross-sectional area of the muscle by allowing a greater number of fibers to be packed within the muscle [6]. Thus, the functional cross-sectional area is a function of the muscle volume (V), the fiber length (L_f), and the pennation angle ($\emptyset$). Alternatively, volume can be calculated by dividing the muscle mass (m) by the density of mammalian skeletal muscle (ρ), so that functional cross-sectional area (CSA_f) is equal to [7]:

$$CSA_f = \frac{V \cdot \cos(\emptyset)}{L_f} = \frac{m \cdot cos(\emptyset)}{\rho \cdot L_f}$$

Specific force, also referred to as specific tension, is the force production per unit cross-sectional area of muscle. Unlike force normalizations to muscle mass, specific force values take the architecture of the muscle into account and is a measure of the intrinsic force production capabilities of the muscle [6-8]. Specific force is a value used to indicate muscle health, as healthy muscle has a relatively constant specific force value (~22.5 N/cm^2 [9]). For example, specific force has been shown to decrease with denervation [10, 11], with disease [12], with unloading due to muscle injury/trauma [13] and other unloading [14, 15]. However, these values can vary in instances that are not related to disease or injury. In fact, there have been observed differences in specific force between different muscles of the same species [16, 17], across species [8, 9, 18-21], with exercise training [22-26], and with age [27-29]. Differences in specific force can also vary

across individuals [26]. Reported specific force values range from 15-30N/cm^2 [9], but variability in reported values between studies is also influenced by variations in methodology [18].

While maximum force production of a muscle is a function of the number of sarcomeres in parallel, shortening velocity is a function of the number of sarcomeres in series. Thus, longer muscles that have more sarcomeres in length can produce contractions more rapidly. This is because the length of time for one sarcomere to shorten is constant but the addition of multiple sarcomeres shortening simultaneously increases the distance that a muscle can shorten in a single unit of time. When the number of sarcomeres in series is constant, the length at which the muscle is held during a contraction also has an impact on the magnitude of force generated by the muscle. Maximum isometric force is produced when the muscle is held at its optimal length. Increasing the number of sarcomeres in series increases the optimal length of the whole muscle [30].

Myogenic Cells

Native muscle repair mechanisms involve muscle precursor cells including satellite cells and myoblasts. Satellite cells are multipotent cells found in skeletal muscle and are responsible for muscle regeneration following injury and for the donation of nuclei to existing muscle fibers during normal muscle growth and development. Satellite cells are typically myogenic but have demonstrated osteogenic and adipogenic potential *in vitro* [31]. *In vivo,* satellite cells proliferate and differentiate into myoblasts which fuse to form multinucleated myofibers as part of the normal physiological response to both trauma and microinjury (Figure 2 [32]) and are essential for native muscle regeneration [33]. They remain quiescent in the basal lamina until they are activated by various growth factors and signaling pathways. Satellite cells are identified through the expression of Pax7, a transcription factor that regulates myogenic proliferation. Once committed, satellite cells express Pax7 and Myf5, a myogenic regulatory factor (MRF), and undergo proliferation. The

cells will then differentiate into myoblasts and will additionally express MyoD, another MRF that promotes terminal differentiation. At this point, the cell is committed to becoming a muscle fiber. The expression of a third MRF, myogenin, promotes the fusion of myogenic precursor cells into multinucleated myotubes. Once fully differentiated, the cells will express additional structural proteins including desmin, α-actinin, and myosin heavy chain to form fully developed sarcomeric structures.

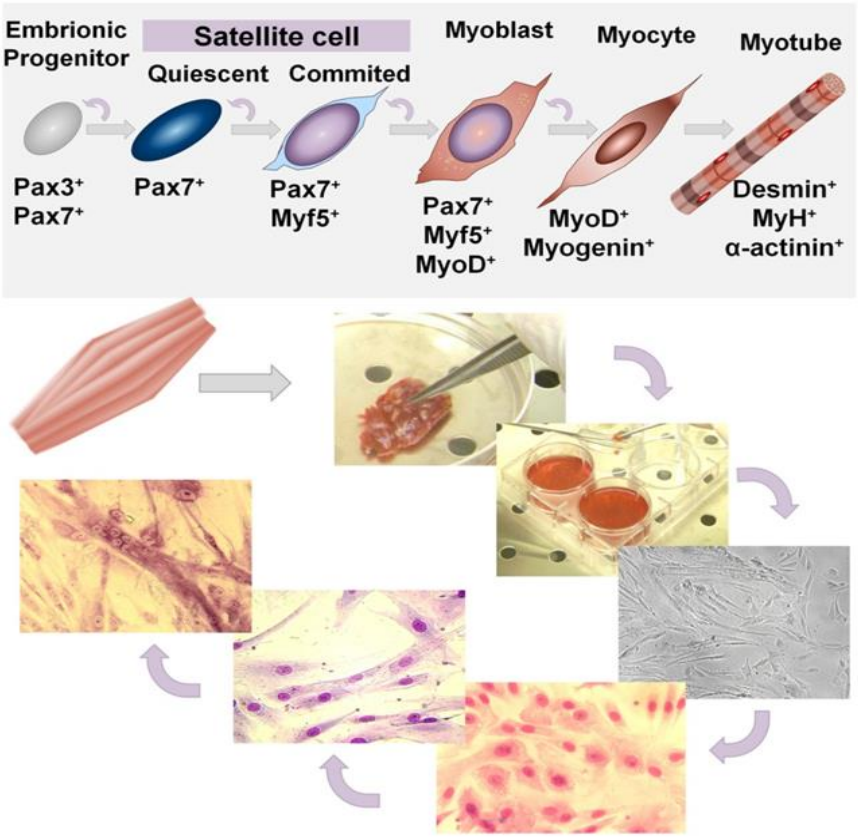

Figure 2. Myogenic Differentiation.

Satellite cells are multipotent cells found in skeletal muscle and are responsible for muscle regeneration following injury and for the donation of nuclei to existing muscle fibers during normal muscle growth and development. Satellite cells proliferate and differentiate into myoblasts that fuse to form multinucleated myofibers as part of the normal physiological response to both trauma and microinjury. During each stage of myogenesis, the cells can be identified through the expression of different markers, including Pax3, Pax 7, Myf5, MyoD, myogenin, desmin, myosin heavy chain (MyH), and α-actinin. The process of myogenesis can be recapitulated *in vitro* by isolating myogenic precursor cells, expanding them, and differentiating them in culture. Functional muscle tissue can then be re-implanted into humans or animals to treat muscle injuries. Image adated from Zouraq et al. Regen Med and Tissue Eng. 2013 [32] and reproduced with the courtesy of InTech Open. Available from: http://www.intechopen.com/books/regenerative-medicine-and-tissue-engineering/skeletal-muscle-regeneration-for-clinical-application.

There are also other populations of multipotent precursor cells found in native muscle that have myogenic differentiation capabilities and may contribute to muscle regeneration following injury. One of these cell populations are pericytes which reside in the walls of microvasculature [34]. Pericytes have demonstrated myogenic potential *in vitro* [35, 36] and have a variety of roles and phenotypes *in vivo* [37-40]. *In vivo*, pericytes secrete paracrine factors that are responsible for vessel maintenance and permeability but can have various roles depending on their tissue location [37]. For example, pericytes in the CNS can regulate the blood brain barrier [41] while pericytes in skeletal muscle can contribute to myogenesis during muscle regeneration [42]. Despite their myogenic potential, perivascular cells including pericytes have limited use in skeletal muscle tissue engineering technologies as they make up only 0.9% of cells isolated from fetal skeletal muscle and 0.3% of cells isolated from adult skeletal muscle [43]. This is in contrast to satellite cells which make up 5-10% of the cells isolated from adult skeletal muscle [44]. Other resident cells with myogenic potential include myoendothelial cells, mesoangioblasts, muscle-derived stem cells (MDSCs), and side population cells which lack markers to define them as another cell type [45-47]. Although all of these cell types have demonstrated myogenic potential, their specific role in native muscle repair and regeneration is not well understood.

Additionally, there are several types of non-resident cells with demonstrated myogenic potential [47-49]. Bone marrow-derived stem cells (BMSCs) can contribute to host-mediated muscle regeneration by differentiating and entering the satellite cell pool [50, 51]. Other cell types do not contribute to muscle regeneration naturally but have demonstrated myogenic potential *in vitro*. These include induced pluripotent stem cells, umbilical cord mesenchymal stem cells, embryonic stem cells, and adipose-derived stem cells (ADSCs). ADSCs are nonhematopoietic stem cells with demonstrated myogenic potential and have gained popularity in tissue engineering

and regenerative medicine due to the relatively high availability of their source tissue [52, 53]. However, safety concerns regarding the implantation of multipotent cells reduces their use clinically. With the exception of BMSCs, these cell types all have myogenic differentiation capabilities and are used in tissue engineering and regenerative medicine applications but are not a source of regenerative cells for native muscle regeneration.

Other Resident Cell Types Involved in Muscle Regeneration

Fibro-adipogenic progenitors (FAPs) are multipotent stem cells that are critical to muscle regeneration in that they provide trophic support to satellite cells following muscle injury [54-56]. They are responsible for secreting factors that regulate satellite cell differentiation as well as maintain the satellite cell pool [57]. Like satellite cells, FAPs are usually quiescent and become activated in response to muscle injury [56, 58]. However, despite the support provided to satellite cells, FAPs also contribute to muscle degeneration following disease or injury by contributing to fibrotic tissue deposition, fatty infiltration, and ossification [56, 59-61]. FAPs have been noted to have fibroblastic, adipogenic, chondrogenic, and osteogenic lineages [61]; however, FAPs have not been noted to have myogenic differentiation capabilities. Nevertheless, they are important regulators of the satellite cell niche and likely play a role in satellite cell support *in vitro* as well.

Myofibroblasts, while not myogenic, are also involved in the wound-healing response, especially with regard to trauma [62]. They are formed when fibroblasts receive signals from soluble factors or changes to their mechanical microenvironment that occur during trauma-induced tissue damage. These signals cause them to differentiate into myofibroblasts; however, they can also be derived from other cell types including epithelial cells, endothelial cells, and mononuclear cells [63]. Myofibroblasts are contractile cells that are characterized by the expression of α-smooth muscle actin [62, 64]. They reside in the ECM and are responsible for secreting collagen during

wound healing and scar formation; however, overactivity of myofibroblasts can also contribute to pathology, including fibrosis and the formation of contractures [63, 65, 66]. For these reasons, they likely play a role in volumetric muscle loss by contributing to the fibrotic response that is a hallmark of the injury.

Volumetric Muscle Loss (VML)

Prevalence and Costs

Musculoskeletal disorders are associated with $800B in annual domestic healthcare costs and have significant effects on a patient's quality of life [67-69]. One of these disorders is volumetric muscle loss (VML) which is the loss of skeletal muscle comprising 20-30% of the total muscle volume. Volumetric muscle loss is common in both civilian and military medicine and often leads to permanent disability when associated with extremity trauma [70-73]. Specifically, VML accounts for 60-65% of military disability patients for which the estimated lifetime disability cost is $340k-440k per patient [70, 71]. Because VML is not a billable condition, the exact incidence of VML is unknown and likely underestimated. VML is often also accompanied by cosmetic deformity which further contributes to the negative impacts of VML, as a lack of satisfaction with physical appearance has a significant effect on quality of life and social functioning, including a lower frequency of interpersonal behavior [74].

Pathophysiology of VML

VML occurs when a large volume of skeletal muscle is lost as the result of acute trauma or surgery which leads to functional impairment [72]. By definition, a VML injury exceeds the body's inherent capacity for self-repair and results in persistent functional deficits. There are several factors that account for this inability to fully recover. First, the loss of muscle is accompanied both by the loss of extracellular matrix (ECM) and by a loss of resident satellite cells. With a diminished

population of satellite cells, the regenerative capacity of the muscle is reduced, as satellite cells are responsible for and are crucial to muscle regeneration and repair following injury [33, 75, 76]. The ECM also plays an essential role in the regeneration of muscle fibers by providing a guide for de novo fiber formation, serving as a repository for various pro-regenerative growth factors, and regulating the satellite cell niche [75-78]. Thus, the loss of the ECM in the defect site prevents its involvement in regenerative processes.

Second, a hallmark of VML injuries is the overwhelming inflammatory response following injury. This chronic inflammatory response is characterized by an upregulation of pro-inflammatory genes that results in large amounts of fibrotic tissue deposition in the defect [79, 80]. This fibrotic tissue deposition can result in muscle tethering that can reduce force production, increase tissue stiffness, and decrease range of motion. As a result, the loss of force production exceeds what can be accounted for by the loss of muscle alone [81]. Furthermore, clinical manifestations of VML have shown that the injury progressively worsens with time [82].

The loss of skeletal muscle often involves the destruction of other tissue types, specifically the peripheral nerve and vasculature associated with the muscle. The loss of these tissues exacerbates the effects of the injury and can have significant impacts on the health of the remaining muscle. The loss or destruction of major blood vessels, if not immediately addressed, can result in ischemia leading to the death of the remaining muscle (i.e. coagulative necrosis). Additionally, the loss or destruction of the nerves innervating the muscle results in an immediate loss of function and subsequent loss of muscle mass as well as atrophy of the muscle fibers [83]. Prolonged denervation causes a disruption in sarcomeric organization, degeneration of muscle fibers, and replacement of the muscle tissue by fibrotic connective tissue and fat [83]. Additionally, denervation injuries are a substantial contributor to chronic pain [84, 85]. Thus, effective treatment

options not only need to replace lost muscle but require the repair or replacement of lost nerve and vasculature as well.

Limitations of Current Treatments

The persistent impairment of muscle function and accompanying cosmetic disfigurements that are characteristic of VML usually necessitate surgical intervention, which traditionally includes muscle flaps and grafts (Figure 3 [86]), as well as fillers and prostheses [86, 87]. Traditional standards of care for VML also include physical therapy, but physical therapy has limited clinical success [81, 88]. Muscle flaps and grafts involve the transplantation of healthy muscle tissue from an autogenic (self) or allogenic (other) donor into the defect site. Because these often require large amounts of tissue, these treatments are limited by tissue availability and donor site morbidity [86, 87]. Muscle transplantation is further limited by size and shape mismatches between the grafted muscle and the defect site which prevents the complete repair of cosmetic deformity and can negatively impact functional recovery. Additionally, major complications, including necrosis and infection, occur in about 20% of free flap transfers, and complete graft failure occurs in up to 5% of cases [89]. In severe cases, failure of the flap can lead to amputation [90].

The use of fillers and prostheses addresses the issue of cosmetic deformity and provides alternative methods of restoring muscle function. Fillers and prostheses involve the injection or implantation of biomaterials into the defect to correct contour deformities, but these often require repeat injections [87]. An example of these technologies, specifically decellularized ECM implants, are used to bridge functional gaps in the muscle and restore the force-producing axis [91-95]. However, the use of xenogenic materials, which are the most common choice, can be limited by suboptimal integration of the material and sustained inflammatory response [87, 96].

Significantly, despite this multitude of options, *no treatments exist that can produce fully normalized structure and function* [96].

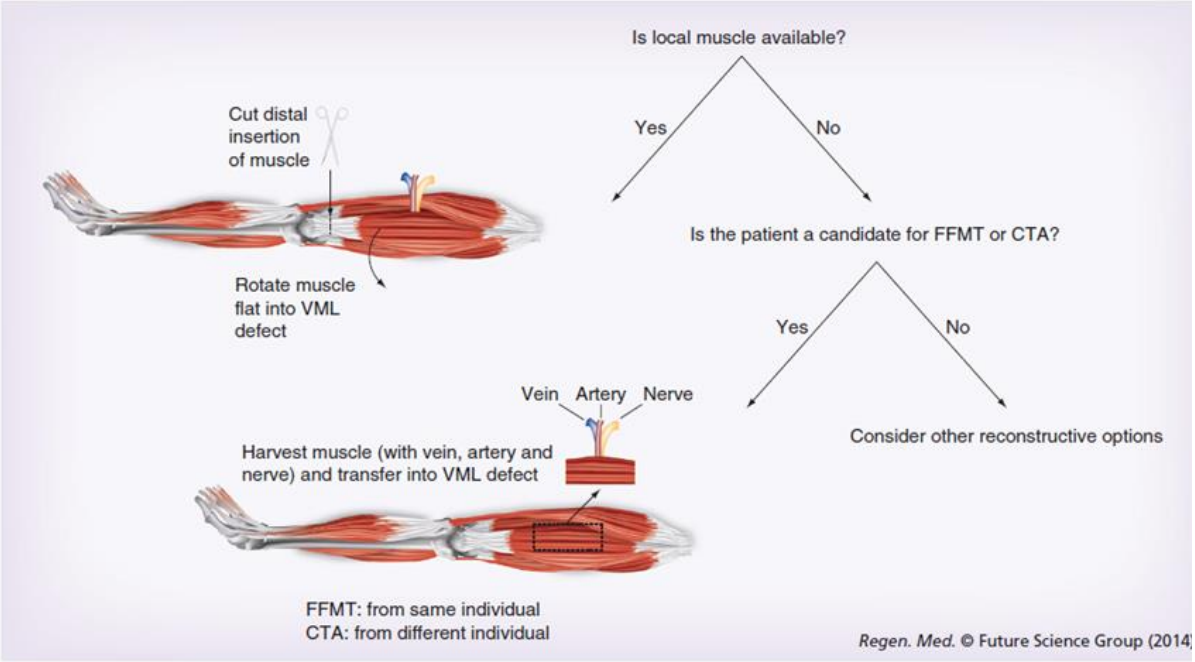

Figure 3. Current Surgical Techniques to Repair Volumetric Muscle Loss.

If healthy muscle tissue is available close to the repair site, a surgeon may choose to cut the distal insertion of the healthy muscle and rotate the healthy tissue into the defect. Alternatively, the patient may undergo free functional muscle transfer (FFMT) or composite tissue allotransplantation (CTA) in which healthy muscle tissue along with its vasculature is excised and transplanted to fill the defect. The donor tissue can come from the patient (FFMT) or from another individual (CTA). Image adapted from Mertens et al. Regen Med, 2014 [86] and reproduced with permission from permission from Future Medicine.

Models of VML

Because of the many limitations of current treatments, many groups are investigating alternative therapies for VML. The US Department of Defense in particular has dedicated funding for research regarding tissue engineering and regenerative medicine therapies for combat injuries including VML [97]. With many groups developing therapies for VML treatment, an obstacle to assessing the success of these treatments is the multitude of VML models being employed which makes it difficult to compare the efficacy of different therapies. For example, the VML models

being used in research remove anywhere from 10-50% of the total muscle mass [98]. The location and geometry of these injuries also varies; some VML models involve the resection of a longitudinal (tendon to tendon) portion of muscle, while others involve a full-thickness resection or a “hole punch” in which tissue is removed from the midsubstance portion of the muscle. Tissue engineering and regenerative medicine technologies have also been developed to repair muscle damage following ischemia [99-102] or crush injuries [103]. These non-VML injuries trigger a different regenerative mechanism because the basal lamina remains intact, which is not the case in a VML model; however, these studies are still relevant as ischemia and crush injuries often occur as comorbidities in clinical manifestations of VML.

VML models also vary in the choice of muscle receiving the injury. The latissimus dorsi (trunk), tibialis anterior (hindlimb), peroneus tertius (hindlimb), and gastrocnemius (hindlimb) muscles are the most common choices in VML studies [98]; however, differences in developmental origin between trunk and limbs muscles and craniofacial muscles results in differences in phenotype which suggests that craniofacial VML may present additional challenges to repair. For example, the increased amount of nerve and vasculature in the face relative to the trunk and extremities means that craniofacial injuries are more likely to affect multiple tissue types simultaneously [96]. Additionally, skeletal muscle’s contribution to facial expression requires more complex motion and synchrony than other areas of the body that results in differences in its ECM, and thus differences in its repair mechanisms [104]. One of these ECM differences is manifested in the existence of the superficial musculoaponeurotic system (SMAS) which is a fibrous tissue network that integrates multiple facial muscles to amplify facial expressions [105, 106]. Indeed, these phenotypic differences include differences in regeneration; craniofacial

muscles have been noted to have reduced regenerative capacities relative to limb muscles following both exogenous and endogenous injuries [107].

Despite these significant differences, there are currently no animal models of craniofacial VML; studies to date have solely involved VML of the trunk and extremities [98]. There is a study which sought to treat VML of the tongue in a rat model [108], but this study did not truly capture the unique characteristics of facial VML, as the tongue has the same developmental origin as trunk and limb muscle and would not fully represent the phenotypic differences of craniofacial muscle [109]. This highlights the need for an VML model that can adequately represent the differences in regenerative capabilities of facial muscle and differences in the pathophysiology of craniofacial VML.

Currently, there is also a lack of large animal models of volumetric muscle loss. Large animal models are especially important for both clinical relevance and to address the limitations of rodent models. Specifically, rodents do not typically present the clinical manifestations of fibrosis seen in humans, and the small sizes of rodent models do not pose a significant challenge to vascular and neural regeneration and growth into the injury site [71, 81, 110]. Furthermore, the FDA recommends testing in both large and small animal models when seeking regulatory approval for a new technology [111]. Besides the sheep models used in our lab, the only large animal volumetric muscle loss models that exist are pigs [80, 112, 113], although one VML study was performed in dogs [114]. Diversity of animal models is important, as it provides more thorough insights into disease pathology as well as mechanisms of repair and regeneration.

Tissue Engineering Approaches for the Treatment of VML

Tissue engineering is defined by the National Institutes of Health as the process of combining any or all of the following—cells, scaffolds, and bioactive molecules—to produce a

construct that is intended to restore, maintain, or improve the function of damaged tissues or organs [115]. These functional tissues can be used for *in vitro* studies of physiology, clinical drug testing, or *in vivo* implantation. The overall approach taken when engineering skeletal muscle tissue is to recapitulate myogenesis. Additionally, tissue engineering strategies aim to promote innate repair mechanisms *in vivo*, often by recruiting native regenerative cells to the repair site. In general, muscle precursor cells are typically seeded onto a scaffold to support their growth and development and are treated with various bioactive compounds to mimic the satellite cell niche and promote the differentiation of the satellite cells into a native muscle phenotype.

Strategies in tissue engineering and regenerative medicine include delivery of exogenous myogenic or other regenerative cells, the implantation of acellular scaffolds, and the implantation of tissue-engineered muscle constructs [86, 116]. Limitations of these strategies include low viability and poor localization of implanted cells [45, 116-121], low levels of scaffold integration into native tissue [122], and regulatory and economic barriers [116, 123-125]. However, the strengths of tissue engineering and regenerative medicine make them the most appealing options for the future of VML treatment. Current methods using acellular scaffolds have been shown to restore the force-producing axis and fill spatial defects [91, 94, 95], while cellular muscle constructs have the ability to donate new muscle fibers to the repair site [126, 127]. Furthermore, these approaches can restore muscle function, recruit native regenerative cells, and integrate with native tissue while addressing the caveats of morbidity associated with traditional surgical treatments [116, 127].

Scaffold-Free Approach to Tissue Engineering

Some researchers take a scaffold-free approach to tissue-engineering in which the muscle precursor cells are often combined with fibroblasts which secrete protein fibers comprising the

extracellular matrix [126-130]. Growth and development of the combined myogenic and fibroblast cells ultimately results in the formation of either a functional three-dimensional construct or a "cell sheet" [129-132]. Three-dimensional constructs are anchored by constraint pins or sutures, which provide passive tension that promotes myotube alignment [133-135] while cell-sheet technologies can promote myotube alignment by micropatterning [129-131]. Overall, scaffold-free constructs are inherently force-producing, biocompatible, and they integrate well with native tissue [127, 128]. Still, even scaffold-free technologies require a substratum, and many approaches have been taken to manipulate the substratum to foster myotube growth and development [126, 127, 136-138].

Instead of attempting to control every design parameter of the cells' three-dimensional microenvironment, the scaffold-free approach allows the cells to create and regulate their own microenvironment through the secretion of extracellular matrix proteins and growth factors. This greatly reduces the cost of the technology by reducing the number of design parameters that would otherwise have to be controlled and regulated. Despite the advantages of scaffold-free technologies, the lack of control over scaffold design parameters can also be seen as a disadvantage. Additionally, this lack of control can produce constructs that are inconsistent in their structure and function.

The Body as a Bioreactor

Tissue-engineered technologies often cannot be fabricated *in vitr*o to match the exact structural, chemical, and mechanical properties of native tissue, but *in vivo* implantation can advance the tissue towards a native-like phenotype [127, 139, 140]. This process of using implantation to advance construct phenotype is known as the concept of "the body as a bioreactor" [141-144]. For example, our lab's constructs possess fetal-like muscle characteristics *in vitro*, but

in vivo implantation has been shown to improve their structure, specifically by producing uniaxially aligned fibers with advanced sarcomeric structure and an extensive extracellular matrix [126, 127, 145]. These studies have also shown that implantation increases the force production of our engineered muscle tissue and that vasculature and nerve readily infiltrate the construct [127, 145].

Current Challenges in Tissue Engineering

There are still many technological, economic, and regulatory obstacles that prevent tissue-engineered skeletal muscle from obtaining widespread clinical use [123, 146-148]. Among these are cell sourcing concerns. Engineered tissues require a large number of cells of the correct phenotype as well as the ability to maintain that phenotype *in vitro*. The use of stem and multipotent progenitor cells addresses the quantity issue, as stem cells have unlimited potential for self-renewal; however, there are safety concerns associated with the use of multipotent cells [149, 150]. Specifically, it is difficult to ensure 100% conversion into differentiated cells *in vitro* and implanted cells that retain potency pose the risk of teratoma formation [149].

Another technical hurdle involves ensuring biocompatibility of the implanted tissue. Biocompatibility is a multi-faceted term; a material is deemed biocompatible if it does not produce a foreign body response (governed by innate immunity), immunogenic response (governed by adaptive immunity), and is not cytotoxic. Cytotoxicity is typically ruled out early in the design process as most biomaterials are well-tested, and their degradation products are well characterized. Immune responses, however, present a greater concern as they cannot be tested until the construct is implanted. Even if the material is biologically inert, it can still produce a foreign body response. A foreign body response is characterized by the presence of pro-inflammatory macrophages and foreign body giant cells as well as the formation of a fibrotic cap around the material [151]. This

type of response is most common in materials that are not adequately degradable. An immunogenic response occurs when adaptive immune cells encounter foreign material. This response can be prevented if the construct is free of antigenic epitopes, including foreign cells and DNA. With the exception of autografts and acellular, synthetic constructs, the possibility of an immunogenic response cannot be ruled out but can be mitigated.

One of the most significant technological challenges of the field to date is the issue of scale-up. Engineered tissues need to be scaled to clinically relevant sizes if they are to be practical for human use. Engineered tissues are typically avascular, so they rely on diffusion alone to allow adequate nutrient delivery and waste removal; however, nutrient penetration depth is limited to several hundred microns in avascular tissue [152]. Thus, as construct size increases, nutrient availability decreases, and the viability of the cells within the construct is threatened. If allowed extended time *in vitro*, large 3D constructs that lack appropriate architecture often form a necrotic core in which cells in the center of the construct die off because nutrients cannot penetrate into the core of the developing tissue [153, 154].

Thus, porosity, pore architecture, and thickness of a 3D muscle construct are the main factors affecting nutrient transport through avascular tissue and have a profound influence on *in vitro* cell viability as a result. Construct thickness in particular is a critical design parameter, as packed cells cannot survive more than 150-200μm from a nutrient source [155]. Avascularity poses additional problems to the constructs once implanted, as the success of *in vivo* implantation is highly dependent on the rapid formation of a vascular network within the construct [156]. To overcome this obstacle, researchers have seeded endothelial cells [129, 130] and pericytes [157] in their constructs, and included pro-vascular growth factors [102] in an effort to pre-vascularize their constructs. *In vitro* prevascularization is the primary approach taken to scale up; however, it

has been described as “one of the greatest unsolved yet intensely investigated areas in the field” [158]. This is primarily due to the inefficiency and length of time required to prevascularize a construct [156]. Although prevascularization has been shown to increase survivability of implanted engineered tissues [159], there remains the challenge of integrating or anastomosing the microvasculature of engineered tissues with the much larger vessels of the host [160]. Spontaneous integration has only been successful in thin tissues [160] and failure to quickly integrate the two vascular systems renders prevascularization a wasted effort. Furthermore, there are difficulties in directing vessel growth in an organized manner to reflect the hierarchical structure of native vasculature [161]. This can be manifested by redundancies in the network which can lead to vessel regression [162].

Alternatively, some researchers have taken a modular approach to scale-up in which smaller tissues are fabricated and then combined just prior to implantation [163-169]. In the past, our lab has used modularity to overcome the obstacle of nutrient delivery by fusing thin tissue units side-by-side just prior to implantation. This method ensures diffusion distances and critical thicknesses are maintained in one dimension and necrotic cores are not an issue. We have previously demonstrated the effectiveness of the modular approach in a rat VML model [166] and in sheep models of VML [170], tendon [167], and ligament repair [168, 169]. Other modular approaches use the technique, not only for the purpose of scale up, but to reliably recreate tissue microstructures that can then be modularly combined to create larger tissues [163, 164].

Summary

In sum, volumetric muscle loss presents a significant clinical challenge in that no treatment options can fully restore function and produce adequate levels of patient satisfaction. VML is difficult to treat due to the loss of several skeletal muscle tissue components that are critical to the

regenerative process (i.e. satellite cells and ECM) as well as the destruction of multiple tissue types including nerve and vasculature which are crucial to muscle health and homeostasis. Engineered tissues pose a promising option for VML treatment in that they can replace lost tissue without the significant limitation of donor site morbidity. Specifically, engineered tissues have been shown to restore muscle function by recruiting native regenerative cells to the repair site as well as donating new muscle fibers to the repair site. The complexity of native muscle structure and function makes it difficult to recapitulate; however, the demonstrated success of engineered tissues has made them promising options for the future of VML treatment.

The coming chapters will address some of the knowledge gaps that have been described in Chapter I. Chapter II addresses the heterogeneity of muscle progenitor cell populations in the fabrication of engineered skeletal muscle tissue. Specifically, in this chapter we evaluated the development, structure, and function of skeletal muscle units (SMUs) fabricated from cells derived from both craniofacial and hindlimb muscle sources. Chapter III addresses the challenges associated with the scale-up of engineered tissues by describing a modular method of scale-up that avoids the formation of a necrotic core. This chapter also addresses the lack of large animal VML models by introducing the sheep as a new large animal model of VML. Additionally, this chapter describes the ability of our engineered tissues to restore muscle mass and force production in a hindlimb VML model following a 3-month recovery. In Chapter IV, we address the lack of craniofacial VML models by introducing the first animal model of craniofacial VML. This chapter also describes pathophysiological differences between hindlimb and facial VML and discusses the characteristics of VML models (i.e. injury size, location, and geometry) and how they affect the severity of the injury.

Chapter II – A Comparison of Ovine Facial and Limb Muscle as a Primary Cell Source for Engineered Skeletal Muscle

The entirety of this chapter was originally published with the following citation: Rodriguez, B. L., Nguyen, M. H., Armstrong, R. E., Vega-Soto, E. E., Polkowski, P. M., & Larkin, L. M. (2019). A Comparison of Ovine Facial and Limb Muscle as a Primary Cell Source for Engineered Skeletal Muscle. Tissue Eng Part A. doi: 10.1089/ten.TEA.2019.0087 [44]. This article has been reproduced with permission from the publisher, Mary Ann Liebert, Inc. The figures have been reformatted and/or reproduced in color.

Introduction

Maxillofacial surgery is the third most common reconstructive procedure performed in the US. In 2017, over 200,000 reconstructive maxillofacial surgeries were conducted to repair facial disfigurements, some of which were performed to treat volumetric muscle loss (VML) [171]. Volumetric muscle loss, which is defined as the degenerative, traumatic, or surgical loss of skeletal muscle, contributes to the prevalence of facial deformities and to the number of soft tissue injuries that necessitate reconstructive surgery [172, 173]. Skeletal muscle inherently has a high regenerative capacity in response to injury [174, 175], but this innate capacity is overwhelmed in the case of VML. VML is characterized by a significant impairment of physical function and, as a result, usually necessitates surgical intervention [176]. Surgical intervention includes the transplantation of muscle flaps and grafts which are limited by tissue availability and donor site morbidity, as well as the implantation of fillers and prostheses which are limited by suboptimal

integration of the material and sustained inflammatory response [86, 87]. Furthermore, these treatment options do not always fully restore function and often fail to produce adequate levels of patient satisfaction [177].

Research in tissue engineering and regenerative medicine has aimed to address the caveats of traditional surgical approaches. A living tissue-engineered muscle construct has the ability to restore muscle function, donate new muscle fibers to the repair site, recruit native regenerative cells, and integrate with native tissue while addressing the issue of morbidity associated with current surgical treatments [116, 127]. However, because the source of muscle progenitor cells for tissue engineering applications is traditionally hindlimb muscle, a potential obstacle to the engineering of facial muscle specifically is the distinct difference in developmental origin between trunk and limb muscle and craniofacial muscle. This difference is related to variations in phenotype between cell populations, including satellite cells [107, 178-180]. The difference in developmental origin between facial and limb muscle prompts the question as to whether the difference in cell populations between these sources affects their ability to form engineered muscle tissues *in vitro.*

Studies have shown that satellite cells derived from craniofacial muscle exhibit differences in regenerative capacity, satellite cell density, and gene expression compared to trunk and limb satellite cells [107, 179, 181]. What has not been elucidated is whether these differences would affect the characteristics of the muscle constructs they produce. Furthermore, there is evidence to suggest that developmental origin alone cannot account for the heterogeneity of satellite cell populations and thus their potential use in tissue engineering applications [107, 178]. For example, satellite cells isolated from multiple hindlimb muscles exhibit different regenerative rates when transplanted into an identical host environment [181]. Thus, properties of satellite cell populations appear to exist as a continuum with a range of proliferative and regenerative capacities, cell

densities, and differentiation timelines [107, 178, 179], so the choice of the optimal cell source for the engineering of skeletal muscle for repair of facial VML necessitates an empirical comparison of cell populations derived from various muscle sources.

Currently, skeletal muscle tissue engineering is almost exclusively performed using muscle progenitor cell populations derived from limb muscles. This includes work from our lab, which to date, has solely involved cell populations derived from hindlimb muscles with the intention of treating VML in other hindlimb muscles [126-128]. Recently, we have begun experiments addressing VML in facial muscle, and because of the apparent heterogeneity of satellite cell populations, we find it appropriate to explore the potential difference in craniofacial versus hindlimb muscle-derived cell populations. Thus, the purpose of this study is to compare the proliferative capacity and differentiation capabilities of cell populations derived from both craniofacial and hindlimb muscle sources. This will not only provide insight into innate regenerative mechanisms of varied skeletal muscle sources but will also give our team the information necessary to determine which cell source is best suited for skeletal muscle tissue engineering.

Specifically, in this study we assessed the development, structure, and function of our lab's skeletal muscle units (SMUs) derived from four muscle sources, including two hindlimb muscles (i.e. soleus and semimembranosus) and two craniofacial muscles (i.e. zygomaticus major and masseter). The soleus muscle is a postural muscle located in the hindlimb and is primarily composed of type I fibers in humans [182]. Due to the higher satellite cell density in the muscle, the soleus muscle has been the muscle source of choice for our previous rat SMU studies [126-128]. The semimembranosus is also a hindlimb muscle and is commonly used in ovine satellite cell studies [183-185] due to the reduced amount of connective tissue and the relative ease of

access compared to the soleus. In humans, the semimembranosus is relatively evenly divided between type I and type II fibers [186]. The masseter is a mastication muscle located in the jaw and is primarily composed of type I fibers in humans [187, 188]. The zygomaticus major is a superficial muscle used in facial expression and is primarily composed of type II fibers in humans [188, 189].

We expect satellite cell density to correlate to the fiber type composition of the muscle, with the muscles predominantly composed of type I fibers having a higher satellite cell density, as has been observed previously [190]. Furthermore, it is likely that the muscles with the highest myogenic cell densities will have the greatest myogenic potential and thus produce the SMUs with the greatest myotube density, most advanced structure, and greatest force production. However, there are other aspects to consider in addition to myogenic potential. For example, it is likely that muscles with more connective tissue will yield a higher number of fibroblasts during enzymatic digestion which is not ideal for our construct fabrication. Thus, we hypothesized that muscles with higher amounts of visible connective tissue will produce constructs with lower force production and lower myotube density compared to other muscle sources.

Methods

Experimental Design

To elucidate the effects of the muscle progenitor cell source, we cultured sheep muscle isolates from four muscle sources (i.e. soleus (Sol), semimembranosus (SM), zygomaticus major (ZM), and masseter (Mas) muscles) and evaluated the SMU development throughout the fabrication process. Specifically, we evaluated the development (myogenesis), structure (histology), and functional outcomes (biomechanics) of the resultant SMUs. The experimental timeline is summarized in Figure 4 and was identical for each group.

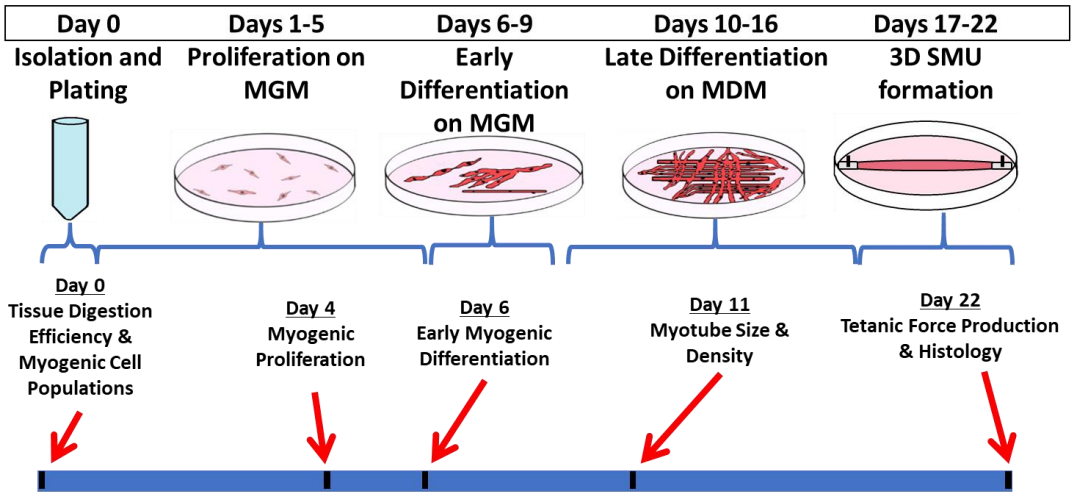

Figure 4. Summary of Experimental Design.

To compare constructs fabricated from different muscle sources, we cultured sheep muscle isolates and evaluated the development, structure, and function of our SMUs at different timepoints throughout the fabrication process. MGM stands for Muscle Growth Medium, MDM stands for Muscle Differentiation Medium. These assessments were completed on each of four experimental groups: zygomaticus major (ZM), masseter, soleus, and semimembranosus (SM) muscle sources.

Muscle Biopsy Collection

All animal care procedures followed *The Guide for Care and Use of Laboratory Animals* [191], according to a protocol approved by the University's Institutional Animal Care & Use Committee. Polypay sheep between 10 and 13 months old (Oswalt Farms, Vicksburg, MI) were anesthetized through the administration of intravenous propofol (8 mg/kg) and gaseous isoflurane at concentrations between 2-5% to maintain a deep plane of anesthesia. Midsubstance biopsies from the semimembranosus, soleus, masseter, and zygomaticus major muscles of were collected under aseptic conditions. After tissue dissection, animals were subsequently euthanized through the administration of a lethal dose of Beuthansia-D Special (195mg/kg) and subsequent bilateral pneumothorax. The biopsies were transported to the laboratory in chilled DPBS supplemented with 2% antibiotic-antimycotic (ABAM) (Gibco, cat. no. 15240-062).

Cell Isolation

Muscle biopsies between 0.8 and 0.9g were sanitized in 70% ethanol and finely minced with a razor blade. The minced muscle was placed under UV light for 5 minutes and subsequently added to a digestion solution composed of 2.3 mg/mL dispase (Thermo Fisher, cat. no. 17105-041) and 0.3 mg/mL collagenase type IV (Thermo Fisher, cat. no. 17104-019). The digestion was incubated for a total of 2.25 hours at 37°C with constant agitation. The resulting suspension was then filtered through a 100μm mesh filter (Fisher Scientific, cat. no. 22-363-549) followed by filtration through a 40μm mesh filter (Fisher Scientific, cat. no. 22-363-547) and centrifuged. The supernatant was discarded, and the cells were re-suspended in muscle growth medium (MGM) as described previously [127, 128, 192].

Digestion Efficiency

After enzymatic digestion of the muscle biopsies, the undigested tissue captured by the 100μm mesh filter was blotted and weighed to provide insight into the digestion efficiency of each type of muscle. Additionally, cell counts were taken from the isolation's resultant cell suspension and normalized to the mass of muscle digested to provide insight into the cell yield per unit mass of muscle. An aliquot of the cell suspension was stained with acridine orange and propidium iodide (AO/PI) and counted using a LUNA-FL Cell Counter (Logos Biosystems, Annandale, VA).

Characterization of Starting Cell Populations

After completion of the cell isolation, cells that were not immediately seeded onto tissue culture plastic were cryogenically preserved in media containing 10% dimethyl sulfoxide. To obtain samples for immunocytochemistry (ICC), the cells were thawed and diluted in DBPS to a concentration of $1\text{-}2\times10^6$ cells/mL. 200μL aliquots of the resultant cell suspension were adhered to glass microscope slides by way of the cytospin technique. The samples were then

immunocytochemically stained for Pax7 (DHSB, cat. no. Pax7c) and MyoD (Abcam cat. no. ab16148) to identify satellite cells and other myogenic cells, as well as vimentin (Abcam cat. no. ab45939) to identify mesenchymal cells including fibroblasts. DAPI was used to identify total cell nuclei (Thermo Fisher, cat. no. P36935). A combination of antigen retrieval and the use of a Tyramide SuperBoost Kit (Thermo Fisher cat. No. B40912) was used to identify Pax7 and MyoD.

Briefly, the samples were fixed in 4% paraformaldehyde, washed in DPBS, and then treated with the 100X H_2O_2 solution according to the SuperBoost kit instructions. The samples then underwent an antigen retrieval step in which the samples were submerged in 10mM citrate buffer, maintained at 92ºC for 11 minutes and then allowed to cool. The samples were then blocked with 10% goat serum in DPBS for 1 hour. Primary antibodies for Pax7, MyoD, and vimentin were diluted in 10% goat serum blocking solution at a ratio of 1:100. The samples were incubated with the primary antibody at 4ºC overnight. The following day, the slides were washed and then incubated with goat anti-mouse poly HRP antibody according to SuperBoost kit instructions for 1 hour. The samples were then washed in DPBS and subsequently treated with tyramide working solution for 10 minutes, followed by treatment with Stop Reagent for 3 minutes, according to SuperBoost kit instructions. The samples were then washed in DPBS and subsequently incubated with a goat anti-rabbit secondary antibody for 1 hour. The samples were then washed and then mounted with a coverslipping medium containing DAPI.

The entirety of the cytospin samples were imaged automatically at 10X magnification on a Zeiss Apotome microscope set to capture a 10% image overlap. Fully stitched images were analyzed using ImageJ/Fiji. The total number of DAPI-stained nuclei were enumerated using the Analyze Particles function in ImageJ/Fiji. Positive staining for Pax7/MyoD that co-localized with nuclei were enumerated to determine the percentage of myogenic cells relative to total cells. We

also enumerated the number of cells expressing vimentin, and the number of cells expressing both vimentin and Pax7/MyoD in the same manner.

Proliferative Capacity

To assess the cells' proliferative capacity, muscle cell isolates were seeded onto 35mm laminin-coated Sylgard plates at a density of 200,000 cells/plate. Plate preparation was completed as described previously [127, 128]. Three days after initial seeding, the cells were treated with BrdU labeling reagent (Thermo Fisher, cat. no. 000103) at a concentration of 1:100 to identify proliferating cells. On day 4, 24 hours after BrdU treatment, the plates were fixed in -20°C methanol for 10 minutes. Immunostaining for BrdU (Abcam, cat. no. ab92837) and MyoD (Abcam, cat. no. ab16148), a myogenic transcription factor that identifies myogenic proliferating cells, allowed us to determine the number of MyoD+ cells and the number of BrdU+ cells per unit area. The plates were imaged and the cells with positive staining were enumerated.

Early Differentiation

To assess the cells' degree of early differentiation, muscle cell isolates were seeded onto 35mm laminin-coated Sylgard plates at a density of 200,000 cells/plate. Six days after initial seeding, the plates were fixed in -20°C methanol for 10 minutes. Immunostaining for myogenin (Abcam, cat. no. ab103924), a myogenic transcription factor present in differentiating myogenic cells, was used to determine the number of differentiating myogenic cells per unit area. The plates were imaged and the cells with positive staining were enumerated.

Late Differentiation

To evaluate late differentiation, we measured myotube size and density. Muscle cell isolates were plated on 60mm laminin-coated Sylgard plates at a seeding density of 600k cells/plate. The cells were allowed to expand in culture until day 7, at which point the culture

media was switched to promote further differentiation, as described previously [127, 128]. On day 11, six representative images were taken of monolayers using light microscopy. These images were used to evaluate myotube size (diameter) and density using the ImageJ software package. Myotube density is defined as the number of myotubes per unit area.

Function

On day 10, minutien pins were anchored to the developing monolayers described in the *Late Differentiation* section. The monolayers were scored around the outside edges 17 days after initial seeding to promote delamination around the anchors. Over the course of days 18-21, the monolayers fully rolled up around the pins to produce cylindrical 3D constructs. On day 22, a minimum of 24 hours after 3D construct formation, tetanic isometric force production was measured to evaluate functionality, as described previously [127, 128, 134]. Briefly, the pin anchoring one end of the construct was adhered to an optical force transducer and released from the Sylgard. Platinum wire electrodes were placed on either side of the construct for electrical field stimulation. Throughout the duration of testing, the temperature and hydration of the construct was maintained in media heated to 37°C. Tetanic isometric forces were elicited with a 1 second square wave stimulus with a 5ms pulse and 90mA amplitude, at 60, 90, and 120 Hz. Force measurements were collected and analyzed using LabVIEW 2012 (National Instruments).

Structure

Immediately after force testing, constructs were coated in Tissue Freezing Medium (Fisher Scientific, cat. no. 15-183-13) and quickly frozen in dry ice-chilled isopentane before being stored at -80°C until sectioning. 10µm cross-sectional and longitudinal samples of the SMUs were cryosectioned for structural analysis and gross morphology. Prior to immunostaining, the slides were fixed in -20°C methanol. Muscle structure was analyzed through immunohistochemical

staining with antibodies for myosin heavy chain (MF20) (DSHB, cat. no. MF 20-c), and laminin (Abcam, cat. no. 7463). Hematoxylin and Eosin (H&E) and Masson's trichrome staining were also completed to provide a qualitative assessment of overall structure.

Statistics

For all graphs, bars indicate mean ± standard deviation. Differences between groups were assessed with one-way ANOVA with post-hoc multiple comparisons test. Significance was established at $P<0.05$. Evaluations of histological samples of 3D constructs were solely qualitative.

Results

Digestion Efficiency

Comparing the mass of undigested tissue and the cell yields of each muscle group provided insight into the digestion efficiency of each type of muscle. This characteristic is important to consider when assessing the clinical relevance of each muscle group as a source of primary cells. Comparisons of the mass of undigested tissue showed a significant difference between groups ($P<0.0001$, n=14 for ZM, n=16 for others). The post-hoc multiple comparisons test showed that all groups were significantly different from each other, with the zygomaticus major having the least efficient digestion (largest amount of undigested tissue) and the semimembranosus having the most efficient digestion (Figure 5A). This same level of significance was not as apparent for the cell yield per mass of muscle digested, although there was a significant difference between groups ($P=0.0313$, n=10 for each group) (Figure 5B). The masseter muscle yielded the largest number of cells per unit mass of muscle digested, but this was only significantly different from the ZM which yielded the fewest cells ($P=0.0278$). Taking these two metrics into consideration, overall, the ZM had the least efficient digestion, making it the least promising cell source in regard to cell yield.

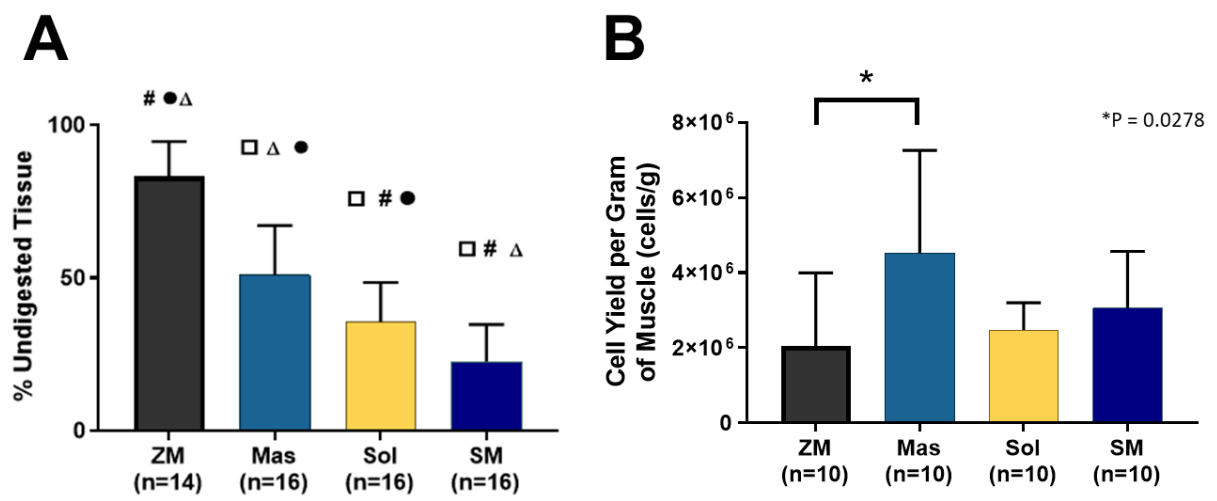

Figure 5. Tissue Digestion Efficiency.

(A) After allowing the tissue to enzymatically digest for 2.25 hours, the undigested tissue was filtered out and weighed to provide insight into the digestion efficiency of each muscle group. There was a statistically significant difference in digestion efficiency between groups ($P<0.0001$, n=14 for ZM, n=16 for others) and all groups were significantly different from each other. Symbols indicate statistically significant differences: □ from zygomaticus major, # from masseter, Δ from soleus, and ● from semimembranosus. (B) Upon completion of enzymatic digestion, cell counts were taken and normalized to the mass of muscle digested. There was a statistically significant difference in cell yield between groups ($P=0.0313$, n=10 for each group). The masseter yielded a significantly higher number of cells than the ZM ($P=0.0278$).

Characterization of Starting Cell Populations

We immunocytochemically stained aliquots of the muscle isolates to evaluate the starting cell populations of each muscle group. We co-stained for Pax7 and MyoD to identify myogenic cells and found that there was no significant difference in the number of myogenic cells between groups ($P=0.7525$, n=2 for soleus, n=4 for others) (Figure 6A). All groups had an average myogenic cell population between 5-10% of the total isolated cells with the soleus having the lowest percentage on average and the SM having the highest. Specifically, the percentage of myogenic cells was 9.18 ± 2.74%, 7.63 ± 3.54%, 6.47 ± 2.06%, and 9.50 ± 3.59% for the ZM, masseter, soleus, and SM, respectively. We also stained for vimentin to identify mesenchymal cells including fibroblasts. The vimentin-positive cells made up ~30-40% of the total cell population. Again, there was no significant difference in the number of vimentin positive cells

between groups (P=0.5596, n=2 for soleus, n=3 for SM, n=4 for others) (Figure 6B). Specifically, the percentage of vimentin-positive cells was 40.8 ± 7.57%, 34.1 ± 10.90%, 32.6 ± 6.84%, and 30.8 ± 3.59% for the ZM, masseter, soleus, and SM, respectively. We also enumerated the percentage of cells expressing both Pax7/MyoD and vimentin and found that these values mirrored the trend seen in the percentage of vimentin-positive cells; however, there was no significant difference between groups (P=0.4802, n=2 for soleus, n=4 for others) (Figure 6C).

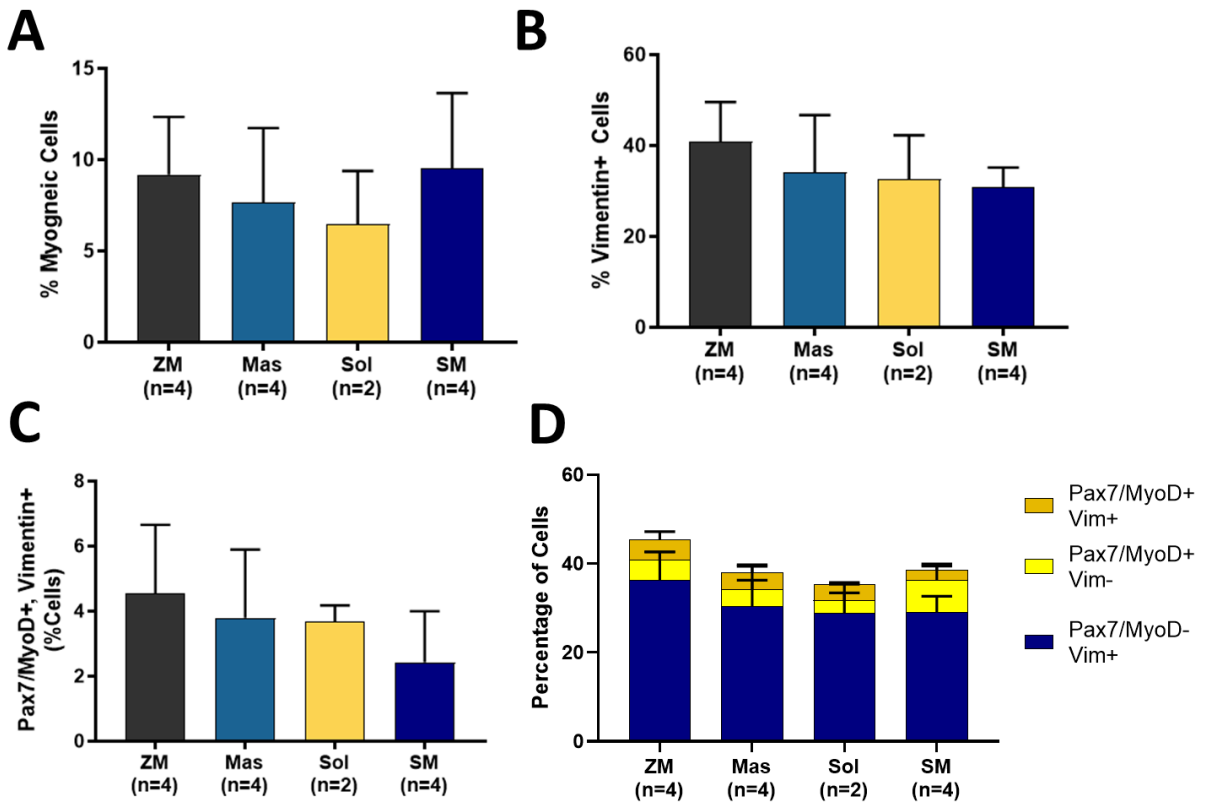

Figure 6. Characterization of the Isolated Cell Populations.

The isolated cells were characterized to determine the percentage of (A) myogenic cells (expressing Pax7 and/or MyoD) and (B) mesenchymal cells (expressing vimentin), (C) the percentage of cells expressing both Pax7/MyoD and vimentin, and (D) a stacked bar representation of the cell composition of the cell isolate. (A) There was no significant difference in the percentage of myogenic cells between groups (P=0.7525, n=2 for soleus, n=4 for others). (B) There was no significant difference in the percentage of vimentin+ cells between groups (P=0.5596, n=2 for soleus, n=3 for semimembranosus, n=4 for others). (C) There was no significant difference in the percentage of cells expressing both Pax7/MyoD and vimentin between groups (P=0.4802, n=2 for soleus, n=4 for others).

Proliferative Capacity & Early Differentiation

Comparing the proliferative capacities and early differentiation capabilities of the cells, we found that there were no significant differences in the number of MyoD+ cells/mm^2 between experimental groups, but there was a significant difference in BrdU+ cells between groups (P=0.0093, n=9 for soleus, n=11 for others) (Figure 7A). The SM plates had a significantly higher number of BrdU+ cells/mm^2 than both the ZM (P=0.0089) and the masseter (P=0.0037) on day 4 (mean of 17.5 cells/mm^2 versus 10.2 cells/mm^2 and 9.5 cells/mm^2, respectively). Immunostaining for myogenin was completed 6 days after initial plating. There was a statistically significant difference in the number of myogenin+ cells/mm^2 between groups (P= 0.0292, n=10 for ZM, n=11 for masseter, n=12 for soleus, and n=13 for SM), with the zygomaticus major having a statistically higher number of myogenin+ cells/mm^2 than the masseter (mean of 616.5 cells/mm^2 versus 364.1 cells/mm^{2,} P=0.0326) (Figure 7B). While the semimembranosus had more proliferating BrdU+ cells/mm^2 than the masseter and ZM, these cells were not necessarily myogenic cells, or at least were not expressing MyoD at this timepoint. The ZM, soleus, and SM showed no difference in the number of myogenin+ cells/mm^2 on day 6, but the ZM did express a significantly higher number of cells than the masseter. However, this trend was not reflected in assays performed at later timepoints (i.e. myotube size and density and force production).

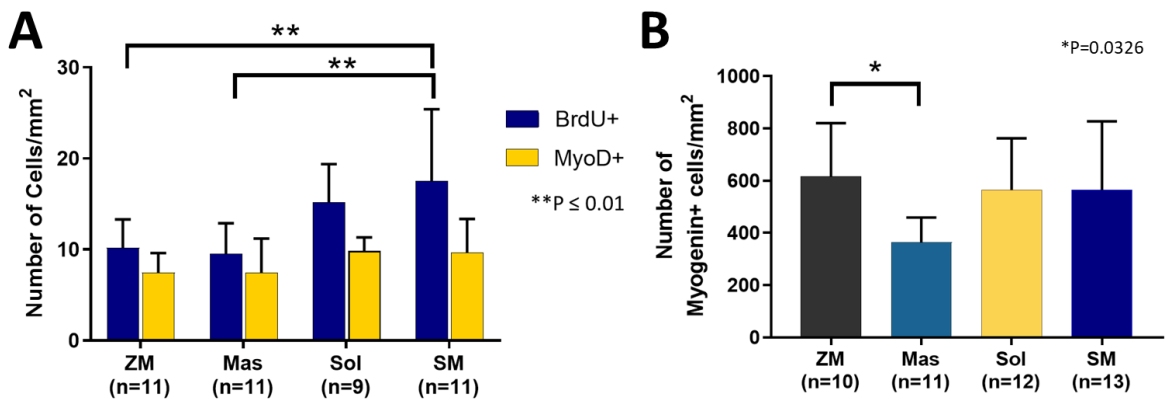

Figure 7. Myogenic Proliferation and Early Differentiation.

(A) A BrdU assay coupled with immunostaining for MyoD was completed four days after initial plating. There were no significant differences in the number of MyoD+/mm^2 cells between groups, but there was a significant difference in BrdU+ cells between groups (P=0.0093, n=9 for soleus, n=11 for others). The semimembranosus plates had a significantly higher number of BrdU+ cells/mm^2 than both the zygomaticus major (P=0.0089) and the masseter (P=0.0037) on day 4. (B) Immunostaining for myogenin completed 6 days after initial plating. There was a statistically significant difference in the number of myogenin+ cells/mm^2 between groups (P= 0.0292, n=10 for ZM, n=11 for masseter, n=12 for soleus, and n=13 for SM), with the zygomaticus major having a statistically higher number of myogenin+ cells/mm^2 than the masseter (P=0.0326).

Late Differentiation

Measures of myotube size and density revealed that there were significant differences between groups in both myotube size (diameter) and density (number of myotubes/mm^2) on day 11 (Figure 8). These results are further reflected in the representative images of the developing monolayers (Figure 8A-D). As can be noted from the images, the monolayer fabricated from zygomaticus major-derived cells appears to have a less dense myotube network and more fibroblast overgrowth compared to the other groups. Images such as these were used to evaluate myotube size and density on day 11. The masseter had significantly larger myotubes than the ZM (P=0.0002) and the SM (P=0.0034) (mean of 27.8μm versus 22.1μm and 23.5μm, respectively), and the soleus also had significantly larger myotubes than the ZM (mean of 25.5μm versus 22.1μm, P=0.0202) (Figure 8E). There was also a significant difference in the number of myotubes/mm^2

between groups: the semimembranosus had significantly more myotubes/mm^2 than the ZM (P=0.0029), soleus (P=0.0055), and masseter (P=0.0007) (mean of 32.3 myotubes/mm^2 versus 25.5, 26.0, and 24.4 myotubes/mm^2, respectively) (Figure 8F).

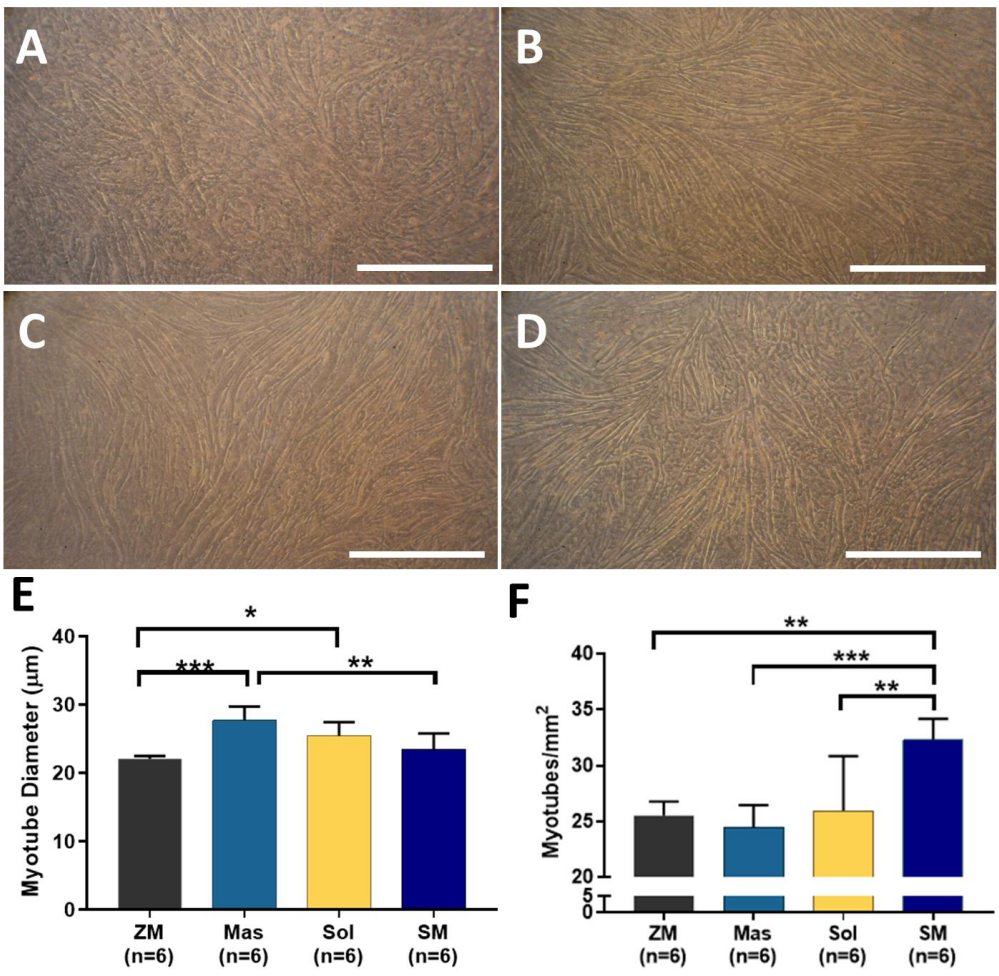

Figure 8. Late Differentiation.

Light microscopy images of the monolayers were taken prior to 3D construct formation in order to visualize the development of the myotubes. The images depicted show representative 10X images of monolayers fabricated from (A) zygomaticus major, (B) masseter, (C) soleus, and (D) semimembranosus muscle sources. As can be noted from the images, the zygomaticus major group exhibited a less dense myotube network and more fibroblast overgrowth compared to the other groups. Scale bars = 500µm. (E-F) Images such as these were used to evaluate myotube size (diameter) and density (number of myotubes/mm^2) on day 11. (E) There was a significant difference in myotube size between groups (P=0.0002, n=6 for each group). The masseter had significantly larger myotubes than the ZM (P=0.0002) and the SM (P=0.0034). The soleus also had significantly larger myotubes than the ZM (P=0.0202). (F) There was also a significant difference in the number of myotubes/mm^2 between groups (P=0.0005, n=6 for each group). The semimembranosus had significantly more myotubes/mm^2 than the ZM (P=0.0029), soleus (P=0.0055), and masseter (P= 0.0007). * indicates $P \leq 0.05$; ** indicates $P \leq 0.01$; *** indicates $P \leq 0.001$.

Function

After formation of the 3D construct, measures of maximum tetanic force production were taken to assess the SMUs' functionality (Figure 9). An ordinary one-way ANOVA revealed that there was a significant difference in force production between groups (P=0.0156, n=22 for ZM, n=25 for masseter, n=26 for soleus, and n=25 for SM). A post-hoc multiple comparisons test revealed that SMUs fabricated from masseter muscle produced significantly higher forces than those fabricated from the zygomaticus major (mean of 61.7μN versus 10.4μN, P=0.0110). However, there were no significant differences in force production between SMUs fabricated from the masseter, soleus, or semimembranosus muscles. Out of these three groups, the SMUs fabricated from the masseter muscle experienced the highest standard deviation, indicating high SMU variability within this group.

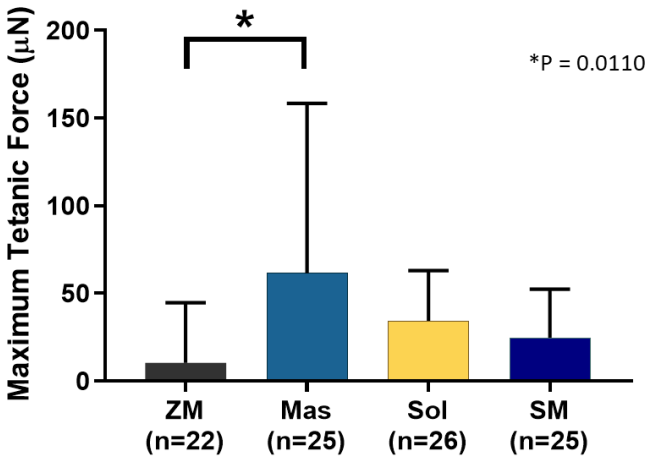

Figure 9. Maximum Tetanic Force Production.

Isometric force production in response to a tetanic electrical stimulus was measured 24 hours after 3D construct formation. There was a significant difference in force production between groups (P=0.0156, n=22 for zygomaticus major, n=26 for soleus, n=25 for others). The SMUs fabricated from masseter produced significantly more force than those fabricated from the zygomaticus major (P=0.0110).

Structure

Cross-sections of 3D constructs provided some insight into the composition of the SMUs. Masson's trichrome staining of SMU cross-sections revealed similarly abundant collagen deposition in all groups (Figure 10A-D). The collagen deposition is important in that it contributes to the structural integrity of the constructs. In the IHC staining, laminin co-stained with myosin heavy chain (MF20) similarly to the way the basal lamina surrounds each muscle fiber in native muscle tissue (Figure 10E-H). Qualitatively, compared to the other muscle sources, the SMUs fabricated from ZM appeared to have less MF20 staining relative to the number of nuclei in the construct (Figure 10I-L). This hypercellularity compared to the other groups was noted in all stains. Furthermore, SMUs fabricated from ZM had less-organized laminin protein. The combination of hypercellularity of MF20-negative cells and less organized laminin likely contributed to the decreased force production of that group. Additionally, the masseter and soleus groups appeared to have more evenly dispersed MF20 staining.

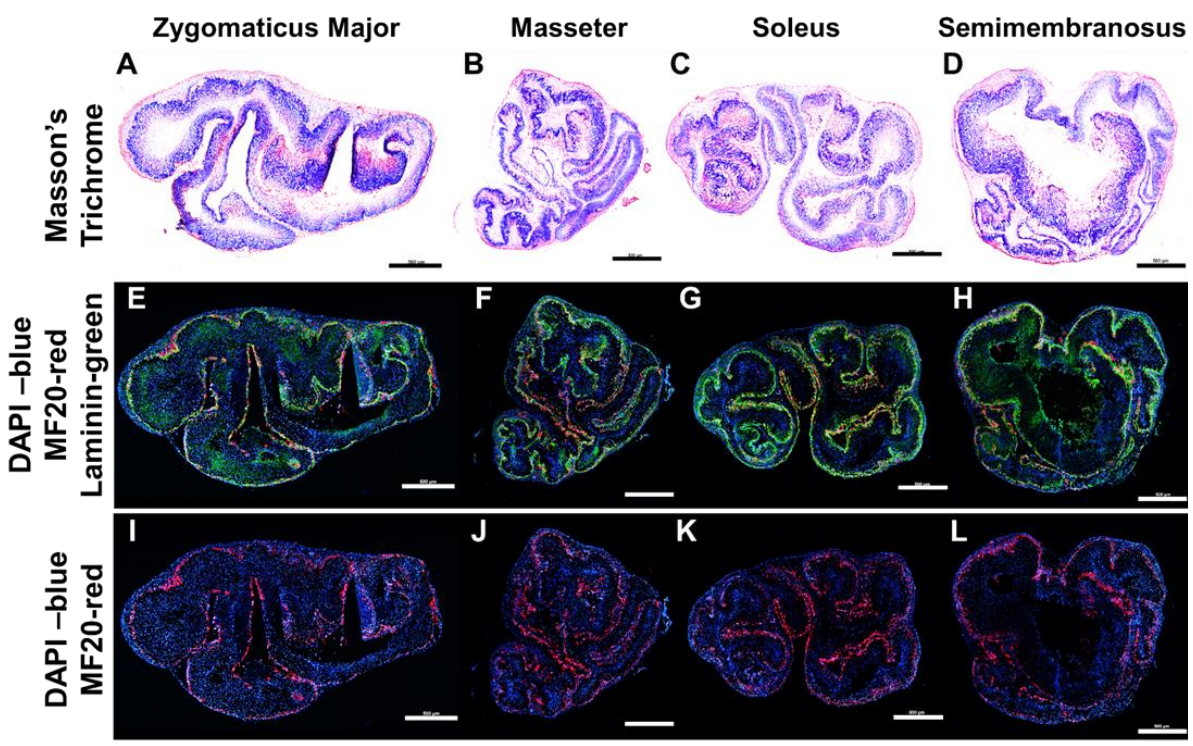

Figure 10. Visualization of Myotubes withing 3D SMUs.

Histology was conducted on cross-sections of the three-dimensional constructs. The images depicted show representative images of SMUs fabricated from (A,E,I) zygomaticus major, (B,F,J) masseter, (C,G,K) soleus, and (D,H,L) semimembranosus muscle sources. Masson's trichrome (A-D) was performed to visualize collagen (blue), as well as muscle (red) and other cellular material (red). IHC (E-L) was performed to visualize the presence of laminin protein (green), muscle fibers (MF20, red) and cell nuclei (DAPI, blue). As can be noted from the images, the SMU fabricated from the zygomaticus major appeared to exhibit hypercellularity and less defined laminin staining compared to the other groups. Scale bars = 500µm.

Staining of longitudinal sections of 3D constructs was conducted to determine the degree of structural organization and anisotropy of each group (data not shown). The hypercellularity of constructs from the ZM groups was also noted in these H&E and IHC stains. MF20 and laminin staining revealed myotube-like structures oriented longitudinally throughout the constructs in all groups; however, there appeared to be a lower degree of alignment present in the ZM group compared to the other groups, which were relatively equivalent in their alignment. This observation may explain why the ZM group had the lowest average force production, as a high degree of myotube alignment is important to maximize the force production capabilities of the

constructs. Additionally, nuclei were present throughout the entire thickness of the construct in all groups. Because the constructs were not fully fused, we believe this characteristic helped prevent the formation of a necrotic core.

Discussion

Overall, this study aimed to evaluate both craniofacial and hindlimb muscles as the source of muscle-derived progenitor cells for the fabrication of tissue-engineered skeletal muscle. Inhomogeneity of cells, especially satellite cells, between craniofacial and limb sources has been well documented in the literature [107, 178-181]. In this study, we sought to evaluate myogenic potential of cells derived from the ovine zygomaticus major, masseter, soleus, and semimembranosus muscles throughout the SMU fabrication process.

It is important to keep translatability and clinical relevance in mind when designing engineered tissue. In general, when starting with a fresh tissue biopsy as a cell source, yielding the greatest number of muscle progenitor cells possible from the smallest biopsy is of the utmost importance in terms of economic efficiency and reducing the potential for donor site morbidity from a live biopsy. While the masseter muscle yielded the most cells per unit mass of muscle digested, this value was not significantly different from the cell yield for the soleus or the SM. Overall, the ZM had the poorest digestion efficiency, with the largest amount of undigested tissue and the lowest overall cell yield. Use of the ZM as a muscle source would require much larger biopsies, making it more costly and more inconvenient, especially considering the small size of the muscle. The fact that the ZM was more difficult to digest and yielded fewer cells is potentially due to the involvement of the superficial musculoaponeurotic system (SMAS) which is described as a fibrous connective tissue network that integrates with facial muscles to amplify their activity in facial expression. With regard to the ZM, the SMAS is described as horizontal fibrous

connective tissues that envelop the zygomaticus musculature [105, 106]. This could explain the large amounts of connective tissue observed during the cell isolation process, as well as the poor digestion efficiency of the ZM overall.

While we did observe a significant difference in the overall number of cells harvested during digestion of the tissue, we did not observe a significant difference in the percentage of myogenic cells yielded between muscle groups. In all muscles tested, the average percentage of myogenic cells yielded was approximately 5-10% of the total cells. We expected the myogenic cell composition to correlate with the fiber type of the muscle; specifically, we expected the muscles with a higher percentage of type I fibers to yield a greater percentage of satellite cells, as described in the literature [190]. However, our data did not support this and was characterized by variability within groups. Each data point represented an individual animal, so this variability could be attributed to variation between animals.

Individual variability, including the effects of sex, age, and castration on skeletal maturity, muscle fiber type composition, and satellite cell density are well-documented in the literature [187, 193-200]; however, the effects vary across species. For example, in mice, the decrease in satellite cells that occurs with age is dependent on fiber type [197, 198], while this decrease in satellite cells with age has not been noted in type I fibers in humans [200]. In sheep, Cancellara et al. found that age has a significant effect on the fiber type composition of muscles, as well as the gene expression [193]. They found that the fiber type composition of the masseter progressively switches to a slow phenotype, while the semimembranosus progressively switches to fast phenotype over the course of the first six months of age [193]. This variability between animals was also noted in ZM fiber type composition data that was collected as part of an unrelated study. We found that type II fibers made up 54.35 ± 11.07% of the fibers, with 3 out of 11 animals having

a type II fiber composition of less than 50%. This contrasts with a study by Schwarting et al. which collected data on four humans and found the ZM to have a type I fiber composition of 66% [189]. A similar level of individual variability may have been present in the other muscle groups, which could explain the differences in the percentage myogenic cells within muscle groups.

These studies support the idea that many factors could have contributed to the variability noted within groups and could have potentially affected myogenic cell yield and quality. This is especially true for the characterization of the starting cell population because we did not control for sex, age, or breed of the animals used in this assay. In all other assays, the cells used came from animals that were the same sex and breed and were within 3 months of age of each other.

Measures of myogenic proliferation showed that all groups were statistically equivalent on day four. While, the SM group demonstrated the highest overall proliferative capacity, this value was not significantly different from the soleus group. Measures of early myogenic differentiation revealed that the ZM, soleus, and SM groups were not significantly different, and the masseter had significantly fewer myogenin+ cells/mm^2 than the ZM on day 6. There was a large difference between the number of cells that were BrdU-positive or MyoD-positive on day 4 and the number of cells that were myogenin-positive on day 6. We believe this difference can be attributed to several factors. First, on day 4 the total cell count was roughly 100 cells/mm^2, whereas only ~5-15% of cells were expressing BrdU or MyoD at this timepoint. In contrast, on day 6 the total cell count was roughly 1,500 cells/mm^2 and the cells expressing myogenin usually made up ~25-35% of the total cells. It is worth noting that there are several cell types on the plates, each with different growth rates. Second, another reason the growth rates may have been so high between days 4 and 6 is that the cells are fed for the first time on day 4. During the feeding, much of the debris from the initial isolation is removed. We believe the presence of isolation debris may inhibit cell growth,

and its removal on day 4 may accelerate the proliferation rate. The plates used for the BrdU/MyoD assay were fixed and stained prior to the first feeding which may contribute to the difference in total cell number.

Furthermore, differences in the differentiation timelines of cell populations from different muscle sources has been noted in the literature [107, 178, 179], and it is possible that the timepoints that were evaluated in this study did not demonstrate the optimal timepoint for that muscle source, especially with regards to the expression of molecular myogenic markers. For example, Ono et al. found that mouse satellite cells derived from the masseter muscle "proliferate more and differentiate later than those from limb muscles" [179]. Our data supports this observation; we found that the masseter had the lowest average of number myogenin+ cells/mm^2 on day 6. Thus, data collected from timepoints later in the fabrication process (i.e. myotube size and density and force production, and histology) are more relevant for comparing groups.

Later timepoints in the fabrication process showed that monolayers fabricated from SM-derived cells had significantly more myotubes/mm^2 than all other groups, with the average number of myotubes/mm^2 being 24-32% higher than the other groups. However, these myotubes were not necessarily as large in diameter as those in other groups. In terms of functionality, forces produced by constructs fabricated from the masseter, soleus, and semimembranosus muscles were statistically equivalent. However, the forces in the masseter group had a high level of variability. This variability could be attributed to differences in individual animal donors. Histological findings supported force production data; SMUs in the ZM group were characterized by hypercellularity, less defined laminin staining, and reduced MF20 staining, as well as less aligned myotubes. All of these factors would have translated to reduced force production. Notably, no qualitative histological differences between SMUs from the other groups were observed.

Conclusions

Ultimately, while this study did not clearly reveal an optimal cell source, what is clear from the results is that the ZM is the least suitable source for harvesting muscle-derived progenitor cells. The ZM group also experienced the least efficient digestion, the lowest average force production, and histologically, experienced the least aligned myosin heavy chain staining. With regards to the size of the muscle, there is also low tissue availability making it less clinically relevant, although the small muscle size is also true for the masseter muscle. For the most part, the soleus performed on par with the SM group, with the exception of myotube density. However, the soleus is less clinically relevant than the SM because it is not a superficial muscle and biopsies would be more invasive. Overall, the SM is the muscle that seems to be best suited as a cell source for muscle-derived cells, although the soleus is also well-suited.

Chapter III – A Tissue Engineering Approach for Repairing Volumetric Muscle Loss in the Ovine Peroneus Tertius

The entirety of this chapter was originally published with the following citation: Novakova, S. S. and. Rodriguez, B. L., Vega-Soto, E. E., Nutter, G. P., Armstrong, R. E., Macpherson, P. C. D., & Larkin, L. M. (2020). Repairing Volumetric Muscle Loss in the Ovine Peroneus Tertius Following a 3-Month Recovery. Tissue Eng Part A. doi: 10.1089/ten.TEA.2019.0288. This article has been reproduced with permission from the publisher, Mary Ann Liebert, Inc. The figures have been reproduced and/or reformatted in color.

Introduction

Musculoskeletal disorders are a major problem in regenerative medicine that accounts for $800 billion dollars in annual health care costs in the United States alone [67]. Volumetric muscle loss (VML) is one of these disorders and significantly affects both military and civilian trauma patients [70-73]. Specifically, VML accounts for 60-65% of military disability patients and results in an estimated lifetime disability cost of $340,000 to $440,000 per patient [70, 71]. VML is defined as the traumatic or surgical loss of a large volume of skeletal muscle resulting in sustained functional impairment and which in many cases is accompanied by peripheral nerve injuries or physical deformity [72]. While skeletal muscle has an innate capacity for regeneration, that capacity is overwhelmed in the case of VML, and instead, fibrotic scar tissue develops in the defect site [71, 201]. The current standard of care for VML injury involves replacing the lost muscle by translocating autogenic tissue from a donor site into the wound. This technique is limited by donor

site morbidity and graft tissue availability [86]. Other treatment techniques use specialized powered bracing in combination with physical therapy [86, 116]. Multiple factors may prevent complete recovery, including the severity of the injury, poor vascularization, denervation, and fatty infiltration. Therefore, despite promising advancements in surgical techniques, results are variable and often fail to restore full functionality in patients [86, 116, 127], and in severe cases, repair failure can lead to amputation [90].

Thus, the restoration of function is critical to improving clinical outcomes for patients with VML injuries. As such, various tissue engineering and regenerative medicine strategies are being developed to address the limitations of current treatment options and promote functional healing. These strategies include the delivery of myogenic cells, the implantation of acellular scaffolds, and the implantation of tissue-engineered skeletal muscle, including both scaffold-based and scaffold-free approaches. A living tissue-engineered muscle construct has the ability to restore muscle function, donate new muscle fibers to the repair site, recruit native regenerative cells, and integrate with native tissue while addressing the issue of morbidity associated with current surgical treatments [116, 127]. The strengths of scaffold-free engineered tissues make them one of the most appealing options for the future of VML treatment. Scaffold-free technologies possess specific advantages over scaffold-based and cell therapy techniques in that they do not incur the foreign body response associated with synthetic scaffolds, the potential immunogenicity associated with naturally derived scaffolds, or the low cell viability common to cell therapy techniques. Previous work in our lab has demonstrated the success of the scaffold-free technique: using our engineered skeletal muscle units (SMUs) to repair a 30% VML injury in a rat tibialis anterior resulted in significantly greater force production compared to unrepaired negative controls after a 28 day recovery, although these forces were still significantly lower than the uninjured contralateral

muscles [8]. Our results have also demonstrated the ability of our SMUs to donate new muscle fibers to the repair site and integrate with host tissue, as evidenced by vascularization and innervation throughout the construct [127, 140, 166].

The success of these studies has prompted our lab to scale up our SMUs for use in a more clinically relevant large animal (sheep) model of VML repair. One of the most significant obstacles preventing tissue-engineered technologies from achieving widespread use in the clinic is the fabrication of tissues of clinically relevant sizes. This is because in an avascular engineered tissue, nutrient availability is limited to diffusion, and prolonged time *in vitro* can result in the formation of a necrotic core. Currently, *in vitro* prevascularization is the primary approach taken to address the limitations of tissue scale-up, but this technique is limited by inefficiency and length of time required to prevascularize an engineered tissue [156]. To circumvent these challenges, herein we designed a modular scale-up of our existing SMU technology with vascularization driven in vivo by the host tissue. In this approach, prior to implantation, we place single SMUs side-by-side allowing lateral fusion and scale-up of the tissue width while still maintaining the original thickness of a single SMU, such that nutrient diffusion distance is unchanged in that dimension and necrotic cores are not an issue. We have previously demonstrated the effectiveness of the modular approach in a rat VML model [166] and in sheep models of tendon [167] and ligament repair [168, 169]. Similarly, in this study we expected to be able to modularly fuse larger SMUs into a single larger graft tissue and apply it to a sheep model of VML.

Treatments for traumatic musculoskeletal injuries often involve rerouting native nerve to the injury site; however, this is impossible when there is not enough native nerve available to span the distance to the repair site. To address this limitation, we have developed an engineered neural conduit (ENC) to bridge this spatial gap and direct neuronal growth to the repair site. In this study,

we simulated this situation by dissecting 1cm of a re-routed native nerve and used an ENC to bridge the 1cm gap between the native nerve and the repair site.

ENCs are primarily composed of collagen and are devitalized prior to implantation. In general, they serve as a scaffold or guide for regenerating axons to migrate from a damaged nerve toward the targeted muscle and to prevent neuroma formation, which can manifest when axon regrowth occurs in an unorganized pattern leading to poorly vascularized and dense fibrotic formations [202-205]. The neural influence on skeletal muscle is well evidenced by the occurrence of muscular atrophy in instances of denervation due to nerve damage [83]. Consequently, ensuring timely innervation of the SMUs is essential to prevent atrophy of SMU myofibers and increase the likelihood of functional recovery.

Thus, the goal of this study was to develop a fabrication method for scaled-up, allogeneic SMUs and ENCs, evaluate the SMUs and ENCs *in vitro*, and to test the efficacy of our SMUs and ENCs in restoring muscle function in a clinically relevant large animal model: sheep receiving a 30% VML injury in a load-bearing hindlimb, specifically the peroneus tertius (PT) muscle, following a 3-month recovery period.

Methods

Animal Care

All animal care procedures followed The Guide for Care and Use of Laboratory Animals [191], according to a protocol approved by the University's Institutional Animal Care & Use Committee. In all instances, animals were first sedated through the administration of intramuscular xylazine (0.2 mg/kg) and then anesthetized through the administration of intravenous propofol (8 mg/kg) and gaseous isoflurane at concentrations between 2-5% to maintain a deep plane of anesthesia. For survival procedures, the animals were fasted and a fentanyl patch (75 mcg/h) was

administered 24hrs prior to surgery. Perioperatively, an intravenous dose of cefazolin (20 mg/kg) was administered. The animals received an intramuscular dose of flunixin (2.2 mg/kg) immediately after surgery with a subsequent dose administered 24hrs post-op as supplementary analgesia. The fentanyl patch was removed 48hrs after surgery. The animals were monitored daily for 10-14 days after surgery by University of Michigan veterinary staff. As a part of this daily health monitoring, the animals' gait was monitored to see if the animals were favoring the surgical leg or exhibiting "toe-touching", a sign of pain. Surgical staples were removed 10-14 days after surgery. For terminal procedures, all animals were euthanized through the administration of a lethal dose of sodium pentobarbital (195mg/kg) and subsequent bilateral pneumothorax.

Muscle Biopsy Collection

A total of three four-month-old female Polypay sheep weighing ~35kg (Oswalt Farms, Vicksburg, MI) were anesthetized and whole muscle dissections of the semimembranosus muscles were completed under aseptic conditions. After the dissection was complete, animals were subsequently euthanized. The biopsies were transported to the laboratory in chilled Dulbecco's phosphate-buffered saline (DPBS) supplemented with 2% antibiotic-antimycotic (ABAM; Gibco, cat. no. 15240-062).

Muscle Progenitor Cell Isolation

Muscle progenitor cells were isolated as described previously [126-128, 166, 206-208]. Briefly, 3.5g muscle biopsies were sanitized in 70% ethanol and finely minced with a razor blade. The muscle then underwent enzymatic digestion in a solution composed of 2.3 mg/mL dispase and 0.3 mg/mL collagenase type IV at 37ºC with constant agitation for 2.5 hours. Following enzymatic digestion, the resultant suspension was filtered through a 100μm mesh filter followed by a 40μm mesh filter and centrifuged. The supernatant was discarded, and the cells were resuspended in

freezing medium (70% Dulbecco's Modified Eagle's Medium (DMEM; Gibco, cat. no. 11995-065), 20% horse serum, 10% dimethyl sulfoxide, supplemented with 1% ABAM), frozen to -80ºC at a rate of -1ºC /minute and stored in liquid nitrogen until plating. Alternatively, a subset of the cell isolates was resuspended in muscle growth media (MGM) (60% F-12 Kaighn's Modification Nutrient Mixture (Gibco, cat. no. 21127-022), 24% DMEM, 15% fetal bovine serum (FBS; Gibco, cat. no. 10437-028), 2.4 ng/mL basic fibroblast growth factor (FGFb) (PeproTech, Rocky Hill, NJ, cat. no. 100-18B), 1% ABAM, and supplemented with an additional 10μL/mL 1μM dexamethasone (DEX; Sigma, cat. No. D4902)) [126-128, 140, 206, 207] and seeded immediately for SMU fabrication.

Modular SMU Fabrication

Cells were plated in MGM at a density of 10,000 cells/cm^2 onto 500cm^2 tissue culture plates. After seeding, the cells were left undisturbed for 5 days and subsequently fed MGM every 2 days. The media was replaced with muscle differentiation media (MDM) (70% M199 (Gibco, cat. no. 11150-059), 23% DMEM, 6% FBS, 1% ABAM, 10μL/mL 1μM DEX, 1μL/mL insulin–transferrin–selenium-X (Sigma, cat. no. I1884), and 0.72μL/mL 50mM ascorbic acid 2-phosphate (Sigma, cat. no. A8960)) [126-128, 140, 206, 207] when the plates were 100% confluent and elongating myotubes began to form a network (approximately 7 days post seeding). Light microscopy images of representative monolayers were taken 10 days after initial plating and prior to monolayer delamination. After 5-7 days on MDM, the monolayers delaminated off the cell culture surface and were transferred to Sylgard-coated plates which were fabricated as described previously [126-128, 140, 166, 206, 207]. Minutien pins were used to pin the monolayer into a 3D cylindrical construct at lengths of 14 ± 1cm and approximately 1cm in diameter. Henceforth, this construct is referred to as a "single scaled-up SMU". To achieve the desired size to fill the VML

defect, a modular approach was used in which 2-4 single scaled-up SMUs were placed side-by-side and allowed to fuse. These constructs are referred to as "modularly fused SMUs". It should be noted that after delamination of the monolayer, the SMUs (both single and modularly fused) are not attached to the culture substrate and are actually suspended in the culture media by the pins. After approximately one week *in vitro*, the modularly fused SMU was ready for either implantation or *in vitro* characterization. An overview of this fabrication process is shown in Figure 11. Notably, the SMUs were allografts and were not devitalized or decellularized prior to implantation.

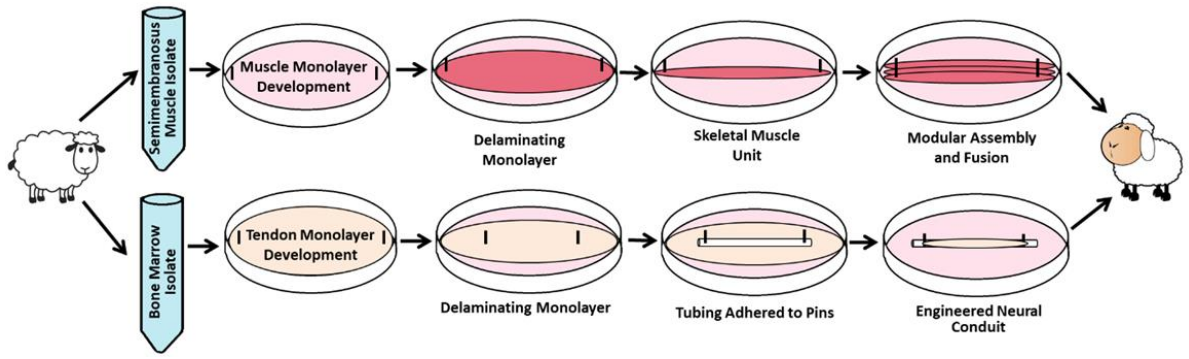

Figure 11. Construct Fabrication Process.

Semimembranosus muscle and bone marrow biopsies were collected from a donor animal. Muscle progenitor cells were isolated from the semimembranosus biopsies and driven down a muscle lineage in culture. After 10 days in culture, the monolayer spontaneously delaminated to form a 3D skeletal muscle unit (SMU). Several SMUs were then combined in a modular fashion and allowed to fuse together before they were implanted into an animal. Similarly, mononuclear cells were isolated from a bone marrow biopsy and driven down a tendon lineage in culture. Several monolayers were wrapped around a piece of nylon tubing to create a lumen. The monolayers were then allowed to fuse in culture to produce a 3D engineered neural conduit (ENC). The ENC was then devitalized by freezing and then implanted into an animal.

In Vitro *Characterization of SMUs*

A subset of each cohort of the SMUs fabricated was reserved for *in vitro* characterization including biomechanical testing and histology. Approximately 24-48 hours after 3D formation, contractile properties of the SMUs were measured as described previously [126-128, 134, 140, 206-208]. Briefly, contractions were elicited through field stimulation with a platinum electrode

and measured by an optical force transducer (World Precision Instruments, cat. no. SI-KG7A) secured to one end of the construct. Tetanic forces were elicited using a 1s train of 2.5ms pulses at 600 to 800 mA and 60, 80, 120, and 150 Hz and measured using custom LabVIEW 2012 software (National Instruments). Following contractile testing, SMUs were coated in Tissue Freezing Medium (Fisher Scientific, cat. no. 15-183-13) and frozen in dry ice-chilled isopentane and subsequently cryosectioned at 10μm. Cryosections of SMUs were stained with hematoxylin and eosin (H&E) and Masson's trichrome (Polysciences Inc., cat. no. 25088-1) to examine morphological characteristics of the SMUs, as well as immunohistochemically stained to identify the presence of myosin heavy chain (5μg/mL dilution, DSHB, cat. no. MF-20c), laminin (5μg/mL dilution, Abcam, cat. no. ab7463), α-actinin (15μg/mL dilution, Abcam, cat. no. ab18061), and Pax7 (1μg/mL dilution, DHSB, cat. no. Pax7c) as described previously [44, 127, 140, 166, 208].

ENC Fabrication

Bone marrow stromal cells were harvested from an iliac crest marrow aspiration of one adult female sheep and mononuclear bone marrow stromal cells were then isolated from the bone marrow as described previously [139, 167-169, 209-211]. Following an established protocol [167-169, 209, 210], isolated cells were induced to a tendon lineage and expanded for five passages. The cells were then trypsinized and seeded at a density of 21,000 cells/cm^2 onto tissue culture dishes with embedded constraint pins. As a confluent monolayer began to spontaneously delaminate off the cell culture surface, the monolayer was wrapped around a 5cm long piece of super soft nylon 11 tubing, creating a lumen (outer diameter 5/32", Freelin-Wade cat. no. 1J-261-10). The tubing was adhered to the dish by pinning it to the embedded constraint pins. A total of four monolayers were wrapped around the tubing and allowed to fuse. The resultant nerve conduits were approximately 4mm in diameter and 7cm in length. Seven days after the last monolayer was

added, media was removed, and ENC was frozen at -80°C to devitalize the cells in the construct and allow for the preservation of the ECM until implantation or *in vitro* characterization. Just prior to implantation, the tubing was removed from the ENC. A subset of the ENCs were coated in Tissue Freezing Medium and frozen in dry ice-chilled isopentane for histology. Cryosections of the ENCs were stained with H&E and Picrosirius Red (Polysciences, Inc., cat. no. 24901-500) to visualize their morphology. An overview of the ENC fabrication process is shown in Figure 11.

Surgical Procedures

Animals used for the surgical implant procedures were 7-month-old Polypay wethers (castrated males) weighing 45-55kg. The animals were randomly divided into three experimental groups: VML only (n=15), VML+SMU (n=15), and VML+SMU+ENC (n=15) (Figure 12). On the day of surgery, the animals were weighed and then placed under a deep plane of anesthesia. A 15cm incision was made along the front of the lower left leg (surgical side) to expose the peroneus tertius (PT) muscle and peroneal nerve. The experimental and control limbs were not randomized; the surgical leg was always the left leg. Gross measurements of the muscle were taken, and a custom algorithm using a 3D model of the PT muscle was used to calculate the muscle mass constituting 30% of the total muscle volume. Subsequently, a full-thickness longitudinal portion of the PT constituting the calculated muscle mass was dissected. The VML only animals (negative control) received the injury without a repair; the fascia and skin were closed with suture and the skin was stapled along the incision. In the VML+SMU group, the injury was immediately repaired by suturing an SMU within the defect. Additionally, the distal branch of the peroneal nerve was transected and re-routed to the SMU to aid the process of reinnervation. In the VML+SMU+ENC group, the VML injury was also repaired with an SMU; however, in this group, 1cm of the re-routed peroneal nerve was dissected to simulate a nerve injury which often accompanies VML.

The gap between the SMU and the peroneal nerve was then bridged with an ENC. 4-0 prolene was used to suture the re-routed nerve and ENC, while 4-0 PDS II was used to suture the SMU, fascia, and skin. All animals were monitored daily for 10-14 days after surgery and then returned to herd housing. The animals were allowed to recover for three months before we assessed functional recovery and performed muscle histological analyses.

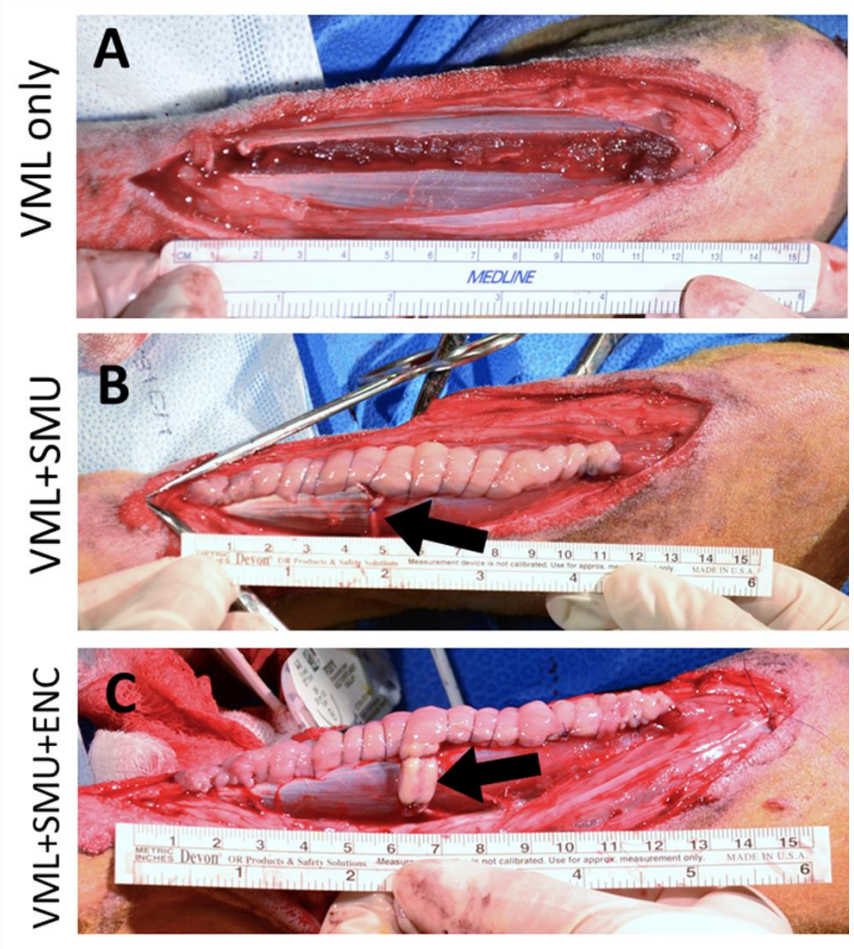

Figure 12. Sheep PT Study: Experimental Groups.

In all groups, a full-thickness longitudinal portion of the PT constituting 30% of the total muscle volume was dissected. (A) The VML only animals (negative control) received the injury without a repair. (B) In the VML+SMU group, the injury was immediately repaired by suturing an SMU within the defect. Additionally, the distal branch of the peroneal nerve was transected and re-routed to the SMU to aid the process of reinnervation (black arrow). (C) In the VML+SMU+ENC group, the VML injury was also repaired with an SMU. Additionally, 1cm of the re-routed peroneal nerve was dissected to simulate a nerve injury. The gap between the SMU and the peroneal nerve was then bridged with an ENC (black arrow).

In Situ Biomechanical Testing

We conducted *in situ* biomechanical testing of both the contralateral and surgical PTs using a custom biomechanical testing system. We chose to perform *in situ* biomechanical testing as opposed to *in vitro* testing because in an initial subset of animals, we were unable to get accurate results through *in vitro* testing. This was because the muscle became hypoxic before completion of testing. Indeed, this has been evidenced in the literature, as the size of the sheep PT exceeds the recommended size of muscles for which *in vitro* biomechanical testing would be acceptable (i.e. hypoxia would not occur if appropriately perfused) [212-214]. Furthermore, it has been observed that absolute forces of muscles tested *in vitro* can be significantly lower than those tested *in situ* [214]. Thus, we performed *in situ* biomechanical testing of the PT muscles and excluded the data collected through *in vitro* testing. For this reason, there is a reduced n number in the analyses involving force measurements.

Following the 3-month recovery, animals were weighed and then placed under anesthesia. Both the contralateral and surgical PTs were dissected leaving the proximal origin intact. To secure the knee, a metal rod was inserted through the femoral epicondyles and secured to a rig mounted to the surgical table. Additionally, adjacent nerves and musculature were severed so as not to interfere with testing. The distal tendon of the PT was secured to a custom strain gauge force transducer (Vishay Precision Group, Malvern, PA) to measure the force of the muscle contractions. Contractions were elicited by stimulating the nerve innervating the PT (i.e. a branch of the deep peroneal nerve) with a bipolar platinum wire electrode. Biomechanical testing of the muscles was conducted as described previously [127, 215, 216]. Briefly, the muscle was placed in the slack position and single 0.1ms pulses of increasing current amplitudes (i.e. 60, 70, 80, 90, 100, 110, and 120mA) were delivered until peak twitch force was reached. Maintaining the current, the

muscle length was subsequently adjusted to the length at which twitch force was maximal. The length of the muscle at which twitch force was maximal was defined as the optimal length (Lo). The stimulus was then switched to a tetanus in which a 600ms train of 0.1ms pulses were delivered. The frequency of these pulses was increased (i.e. 60, 80, 100, 120Hz) until isometric tetanic force was maximal. Data was recorded using custom LabVIEW 2018 software. This process was then repeated on the contralateral (uninjured) PT muscle. Immediately after biomechanical testing, both the contralateral and surgical PTs were fully dissected, weighed, and prepared for histology. The animals were subsequently euthanized.

Histology & Collagen Content

After dissection, the muscles were weighed, and gross measurements were taken. The muscles were then divided into segments and prepared for histology in one of two ways; the sample was either coated in Tissue Freezing Medium and frozen in dry ice-chilled isopentane or fixed in 10% formalin for 24hrs and then embedded in paraffin. Frozen samples were cryosectioned at 10μm and then immunohistochemically stained to identify myosin heavy chain (5μg/mL dilution, DSHB, cat. no. MF-20c) and laminin (5μg/mL dilution, Abcam, cat. no. ab7463) as described previously [127, 140, 166, 208]. Longitudinal samples were immunohistochemically stained for acetylcholine receptors (α-bungarotoxin, 1:2000 dilution, Life Technologies, cat. no. B1601), synaptic vesicle protein-2 (2μg/mL dilution, DSHB, cat. no. SV2c), and neurofilament (0.5μg/mL dilution, BioLegend, cat. no. 837904) to identify the presence of neuromuscular junctions.

Paraffin-embedded cross-sectional samples were sectioned at 5μm and stained with H&E, Picrosirius Red, and Masson's trichrome. To quantitatively evaluate the collagen content of the muscles, a cross-section from the midbelly at the widest portion of the contralateral and surgical PT muscles was stained with Picrosirius Red. These samples were imaged and the percentage of

positive staining relative to the total cross-sectional area (percent collagen) was measured using ImageJ/Fiji (NIH).

Statistical Analysis

Statistical analyses were performed using GraphPad Prism 7 software. Statistical differences between groups in which the contralateral muscle was compared to the surgical PT muscle were assessed with a two-way ANOVA with repeated measures (two-way RM ANOVA) and Sidak's multiple comparisons (Sidak's MC) tests. Statistical differences between groups in which the values were normalized to the contralateral side were assessed with a one-way ANOVA with Tukey's multiple comparisons (Tukey's MC) test. Results were significant at $P<0.05$. Bars on graphs indicate mean ± standard deviation.

Results

SMU Graft Scale-up

We successfully scaled-up SMUs grown from allogeneic ovine muscle progenitor cells by using a larger cell culture surface to produce single scaled-up SMUs which were then combined in a modular fashion to produce modularly fused SMUs. Single scaled-up SMUs were increased in size by approximately 350% when fabricated on 245mm X 245mm tissue culture plates compared to the 100mm diameter tissue culture plates used in our previous study [140]. By day 10 in the fabrication process, monolayers exhibited 100% confluence and were comprised mainly of highly aligned myotubes (Figure 13B). It is important to note that the scaled-up monolayers did not exhibit an overgrowth of fibroblasts, demonstrating similar morphology to SMUs fabricated on 100mm dishes. Utilization of our scaled-up fabrication method resulted in 3D cylindrical constructs that were 14 ± 1cm in length and approximately 1cm in diameter (Figure 13A). These single scaled-up SMUs were then modularly fused for implantation.

Histological Characterization of SMUs

To examine general morphological characteristics of the engineered constructs *in vitro*, staining with H&E and Masson's Trichrome was performed. Histological analyses of stained longitudinal sections revealed that single scaled-up SMUs were composed of linearly aligned muscle fibers surrounded by a collagen extracellular matrix (Figure 13C, G). Additionally, Figure 13E shows that the core of the single scaled-up SMUs was not necrotic, as indicated by the presence of DAPI-stained cells throughout the entire thickness of construct. The presence of cells throughout the construct suggests that there was adequate nutrient delivery and waste removal during the construct fabrication and maturation process.

In order to characterize the SMU structural composition, immunohistochemical (IHC) staining was performed with antibodies specific to myosin heavy chain and laminin (Figure 13D, H). Staining shows that SMU fibers were surrounded by a distinct laminin-rich extracellular matrix, much like the basal lamina surrounding native muscle fibers. Additionally, IHC was performed with antibodies specific to α-actinin to visualize the organization of Z-discs. Staining revealed sarcomeric organization and striations characteristic of native skeletal muscle (Figure 13I). Additionally, we performed IHC staining for Pax7+ satellite cells and found that the SMUs contained a population of muscle progenitor cells prior to implantation (Figure 13F).

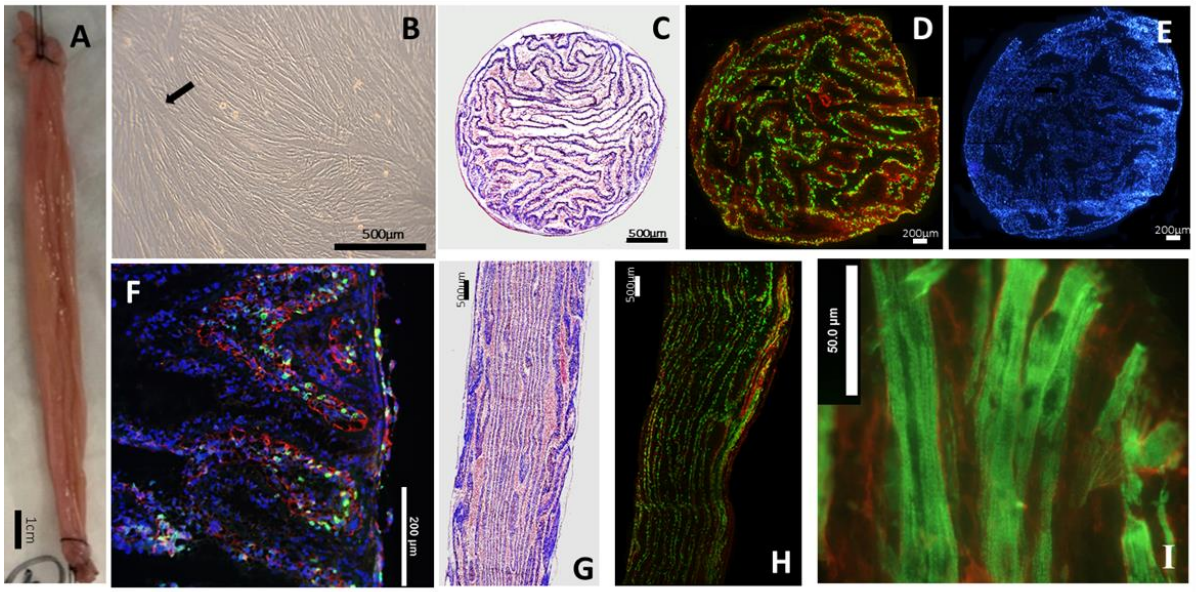

Figure 13. **In Vitro *SMU Characterization.***

(A) Grossly, modularly fused SMUs are about 14cm long prior to implantation. (B) Images of representative monolayers were taken 10 days after initial plating, prior to the delamination of the monolayer. Arrow indicates a fused myotube. Masson's trichrome staining of a single scaled-up SMU cross-section (C) and longitudinal section (G) show that the ECM is composed of collagen (blue) and collagen fibers are oriented parallel to the longitudinal axis. Immunostaining for myosin heavy chain (MF20, green) and laminin (red) of an SMU cross-section (D) and longitudinal section (H) reveal the presence of muscle fibers dotted throughout the SMU. (E) Nuclear staining with DAPI in cross section shows the absence of a necrotic core. (F) We noted the presence of satellite cells (Pax7, green), laminin (red), and nuclei (DAPI, blue) in the single scaled-up SMUs in vitro. (I) Additional staining for α-actinin (green) and laminin (red) reveal the presence of an organized sarcomeric structure and striations characteristic of native muscle.

Biomechanical Testing of SMUs

For each of the modularly fused SMUs that were implanted, it was necessary to fabricate sentinel constructs using smaller 60mm diameter dishes and measure force production *in vitro* to ensure the quality of our cell isolation and culture conditions. Ultimately, we were limited by our *in vitro* force testing equipment since the construct length and size of the scaled-up SMUs exceeded our *in vitro* testing capabilities. Thus, we fabricated smaller sentinel SMUs using the same protocol and media supplies for *in vitro* mechanical testing.

After the monolayers delaminated and were organized in 3D form, the maximum isometric tetanic force production of each sentinel SMU was measured (n=22 total). Force testing indicated

an average isometric tetanic force of 992μN with the minimum and maximum tetanic force produced by a single SMU fabricated on a 60mm dish ranging from 132μN and 4,587μN, respectively. For SMUs of this size, our release criterion stipulates that SMUs need to produce a tetanic force of at least 100μN to be suitable for implantation. Based on years of historical data from our lab, we have observed that SMUs that do not meet the 100μN requirement are not successful when implanted and show little muscle regeneration. Notably, all of the constructs met this implantation requirement. We then used this data to estimate the force production of our single scaled-up SMUs. We first calculated the force per cross-sectional area of each of these sentinel SMUs and found that the average force per cross-sectional area for the sentinel SMUs was 1,180μN/mm^2 with the minimum and maximum being 22.4μN/mm^2 and 5840μN/mm^2, respectively. We then multiplied this value by the average cross-sectional area of the single scaled-up SMUs. Using this estimation, we found that the average tetanic force for the single scaled-up SMUs was predicted to be 8,370μN with a minimum and maximum value of 158μN and 41,300μN, respectively, and the 95% confidence interval for the tetanic force of a single scaled-up SMU was predicted to be 3,090-13,600mN.

Histological Characterization of ENCs

H&E staining was performed for qualitative morphological assessment of the ENCs and indicates that the wall thickness of the ENCs were approximately 1.5-2mm and contained densely packed nuclei (Figure 14A-B). Picrosirius red staining was used to characterize the content and alignment of collagen within the engineered ENC prior to implantation (Figure 14C-D). When imaged under polarized light, the collagen birefringence showed that the ENCs demonstrated a semi-organized collagen fiber framework with regions of aligned collagen bands similar to a

native-like collagen crimp pattern (Figure 14E). Grossly, the ENCs are approximately 7 cm in length before implantation (Figure 14F).

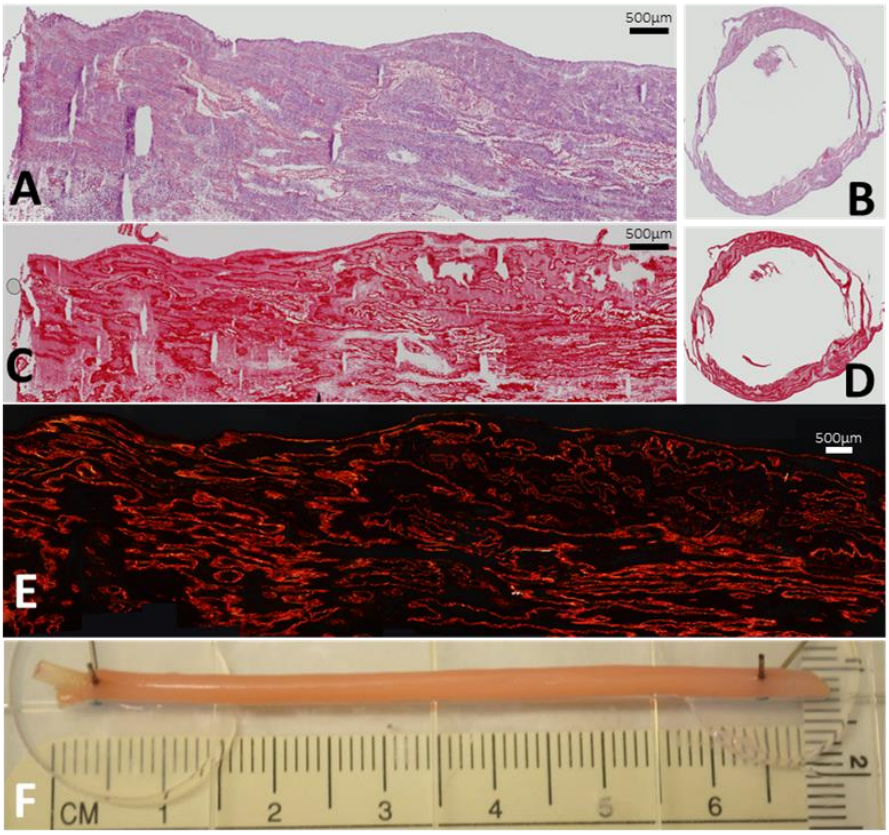

Figure 14. **In Vitro** ***ENC Characterization.***

H&E staining of (A) longitudinal sections and (B) cross-sections of ENCs show general morphology, particularly the hollow lumen (B) resulting from placement of the nylon tubing. Picrosirius Red staining of (C) longitudinal sections and (D) cross-sections show the ENCs are primarily composed of collagen, and under polarized light (E), the collagen displays parallel structure. (F) Grossly, the constructs are approximately 7cm in length before implantation.

Surgical Procedures

Across all groups, the average percentage of VML that was created was 27.9 ± 3.26% and the actual mass removed was 5.26 ± 0.76g. The variability in the weights removed is due to differences in size of the PT muscles between individuals. There was no significant difference in the magnitude of the VML injury between groups (one-way ANOVA: P=0.1909, n=15 per group).

Specifically, the VML injury was equal to 27.0 ± 3.08% in the VML only group, 27.7 ± 3.26% in the VML+SMU group, and 29.1 ± 3.38% in the VML+SMU+ENC group (Figure 15A).

Body Mass and Muscle Mass Recovery

Animals were awake, alert, and weight-bearing within two hours of completing surgery. None of the animals were observed to have abnormal gait after surgery; however, n=2 animals did exhibit "toe-touching" up to 24 hours following surgery, but subsequently showed no signs of "toe-touching". Additionally, animals experienced mild to moderate swelling at the injury site for up to two weeks post-op. 89% of animals gained weight normally during the 3-month recovery period and there was no significant difference in the animals' body weight between experimental groups (two-way RM ANOVA: experimental group: P=0.2528, n=45) (Figure 15B). This indicates that the experimental group did not significantly impact the health of the animals during this 3-month recovery period. Additionally, no signs of rejection were observed in the sheep. Bloodwork taken at the time of explant revealed no signs of a chronic immune response, although one animal did exhibit monocytosis.

Gross observations at the time of explant revealed larger amounts of connective tissue in the surgical PTs of all animals relative to what was observed in the uninjured contralateral. No muscle unit tethering was noted. At the time of explant, we compared the weights of the surgical and graft PTs. Notably, there were no significant differences in muscle mass between the contralateral and surgical PTs in the VML+SMU and the VML+SMU+ENC groups (Sidak's MC: P=0.1406 and P=0.0555, respectively, n=15 per group) (Figure 15C). In contrast, there was a significant muscle mass deficit in the VML only group (Sidak's MC: P=0.0003, n=15) indicating a lack of muscle mass recovery. The mass deficit experienced by the VML only group was expected, as the defect in the VML only group was not repaired with a construct or any other filler.

Specifically, the mean difference in muscle weight between the contralateral and surgical PTs in the VML only, VML+SMU, and VML+SMU+ENC groups was 2.82g, 1.34g, and 1.62g, respectively. We also compared groups after normalizing the weight of each surgical PT muscle to the contralateral muscle. Represented as a percentage of the contralateral, there were no significant differences in PT weight between groups (one-way ANOVA: P=0.2613) (Figure 15D). On average, the VML only, VML+SMU, and VML+SMU+ENC groups experienced an 8.24%, 4.10%, and 5.28% muscle mass deficit, respectively.

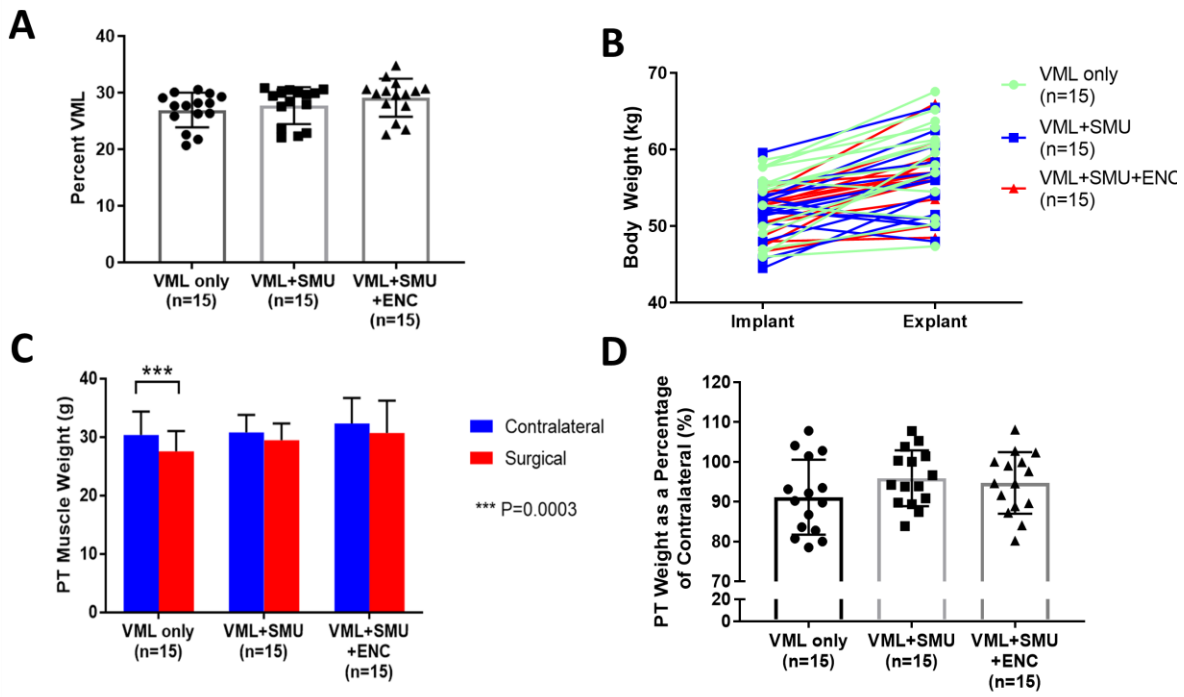

Figure 15. VML Injury and Mass Recovery.

(A) Across all animals, the average percentage of VML was 27.9 ± 3.26%. There was no significant difference in the magnitude of the VML injury between groups (P=0.1909). (B) The majority of the animals gained weight normally during the 3-month recovery period. The surgical group did not significantly affect the animals' body weight over time (P=0.2528, n=45). (C) We assessed the ability of our grafts to restore lost muscle mass by comparing the weights of the contralateral and surgical PTs at the time of explant. The VML only group exhibited a significant difference in muscle mass between the contralateral and surgical sides (P=0.0003, n=15), indicating a lack of mass recovery. Conversely, there was no significant difference in muscle mass observed between the contralateral and surgical PTs of the VML+SMU and the VML+SMU+ENC groups (P=0.1406 and P=0.0555, respectively). (D) Expressed as a percentage of the contralateral, the mass deficit in the VML only group is more apparent, albeit not significant.

Force Recovery

To assess force recovery, we compared the maximum tetanic force of the surgical PT to that of the contralateral PT (Figure 16A). Notably, only the VML only group had a significant difference in maximum force production between the surgical and contralateral PTs (Sidak's MC: $P<0.0001$, $n=11$) indicating a lack of force recovery. In contrast, the VML+SMU and VML+SMU+ENC groups produced forces that were not significantly different from the contralateral side (Sidak's MC: $P=0.0613$, $n=9$, and $P=0.5755$, $n=11$, respectively). Specifically, the mean difference in maximum tetanic force between the contralateral and surgical PTs in the VML only, VML+SMU, and VML+SMU+ENC groups was 71.4N, 39.0N, and 17.0N, respectively. Represented as a percentage of the contralateral, the VML+SMU+ENC group produced significantly higher forces than the VML only group (Sidak's MC: $P=0.0320$) (Figure 16B). On average, the VML only, VML+SMU, and VML+SMU+ENC groups experienced a 30.0%, 17.5%, and 7.78% force deficit, respectively. Additionally, the data shows no significant variability in the frequency required to produce a maximum tetanus. For the uninjured contralateral, maximum tetanus was achieved at 82.6 ± 13.2 Hz and for the surgical legs, maximum tetanus was achieved at 85.2 ± 11.3 Hz. Specifically, the frequency was 84.5 ± 9.9Hz, 91.1 ± 12.9Hz, and 80.9 ± 9.0Hz for the VML Only, VML+SMU, and VML+SMU+ENC groups, respectively. Statistically, there is no significant difference between these groups (one-way ANOVA: $P=0.2623$).

Because of the complex muscle architecture of the PT muscle, we were not able to calculate specific force in the traditional sense, by dividing the maximum force by the physiological cross-sectional area. Instead, we normalized the maximum force to the muscle weight (Figure 16C-D). The trends noted previously were again present in this normalized data. Once again, the VML only

group experienced a significant deficit in force per gram of muscle between the surgical and contralateral PTs (Sidak's MC: P=0.0018, n=11) while the VML+SMU and the VML+SMU+ENC groups had no significant differences between the contralateral and surgical PTs (Sidak's MC: P=0.1225, n=9 and P=0.9596, n=11, respectively) (Figure 16C). Specifically, the mean difference in force per gram of muscle between the contralateral and surgically repaired PTs in the VML only, VML+SMU, and VML+SMU+ENC groups was 1.91N/g, 1.16N/g, and 0.22N/g, respectively. Represented as a percentage of the contralateral, there were no significant differences in the force per gram of muscle between groups (one-way ANOVA: P=0.0783) (Figure 16D). On average, the VML only, VML+SMU, and VML+SMU+ENC groups experienced a 22.55%, 15.88%, and 3.17% normalized force deficit, respectively.

Although we did not notice any muscle unit tethering, we did observe changes in the optimal length (Lo) of the muscle when comparing the surgical to the contralateral PT. A Sidak's multiple comparisons test revealed that there was a significant difference in the optimal length of the muscles between the contralateral and surgical PTs of the VML only group (P=0.0025, n=10) and in the VML+SMU+ENC group (P=0.0222, n=11), but not in the VML+SMU group (P=0.0868, n=9) (Figure 16E). Represented as a percentage of the contralateral, there was no significant difference in the percentage of optimal length between the groups (one-way ANOVA: P=0.6939) (Figure 16F). This reduction in Lo suggests a change in the tissue's mechanical properties and the gross architecture of the muscle.

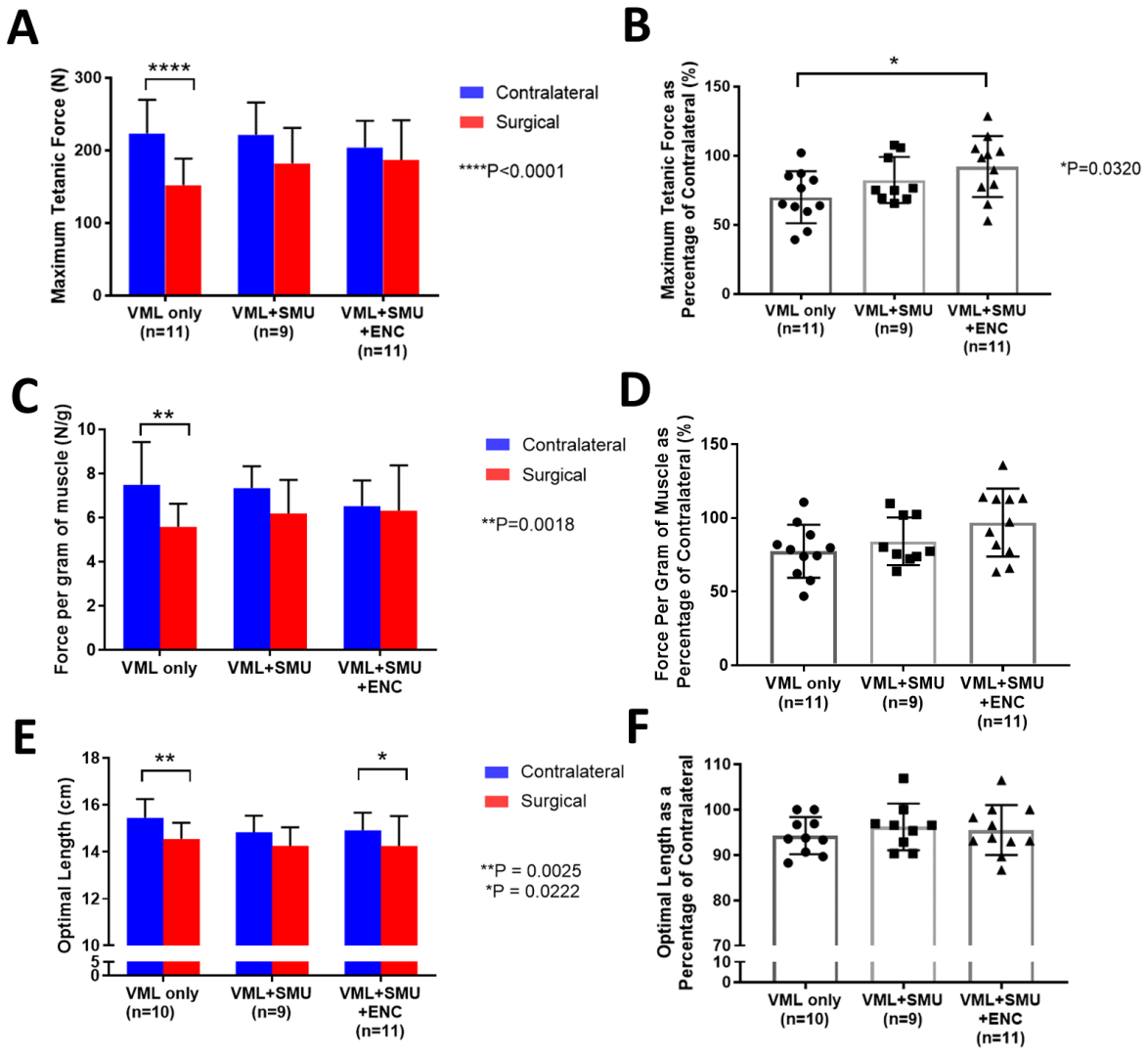

Figure 16. Restoration of Force Production.

Tetanic isometric forces elicited by an electrical stimulus were measured from both the surgical and contralateral PT muscles. (A) In the VML only group, the maximum force production of the surgical PT was significantly lower than the contralateral PT (P<0.0001, n=11). In contrast, there was no distinguishable difference in force production in the VML+SMU group (P=0.0613, n=9) or the VML+SMU+ENC group (P=0.5755, n=11). (B) When the force capability of the injured muscles is expressed as a percentage of the contralateral, it is apparent that the VML+SMU+ENC group experienced the greatest restoration of force production and was significantly higher than the VML only group (P=0.0320). Maximum isometric tetanic forces were also normalized to muscle mass. (C) In the VML only group, the force per gram of muscle of the surgical PT was significantly lower than the contralateral PT (P=0.0018, n=11). In contrast, there was no distinguishable difference in force production in the VML+SMU group (P=0.1225, n=9) or the VML+SMU+ENC group (P=0.9596, n=11). (D) When the force per gram of muscle of the surgical PTs is expressed as a percentage of the contralateral, it is apparent that the VML+SMU+ENC group experienced a greater normalized force than the VML only group, but this was not significantly different (P=0.0783). (E) There was a significant difference in the optimal length of the muscles between the contralateral and surgical PTs of the VML only group (P=0.0025, n=10) and in the VML+SMU+ENC group (P=0.0222, n=11), but not in the VML+SMU group (P=0.0868, n=9). (F) Represented as a percentage of the contralateral, there was no significant difference in the percentage of optimal length between the groups (P=0.6939).

In addition to stimulating the nerve innervating the PT, we also sought to elicit a muscle contraction by stimulating the nerve that was transected and re-routed to the surgical site. Direct stimulation of the re-routed nerve resulting in a muscle contraction occurred in 25% (three out of twelve) animals in the VML+SMU group and 75% (nine out of twelve) animals VML+SMU+ENC group. This direct stimulation produced a contraction through the center of the muscle at the site of the initial injury. This suggests that the re-routed nerve was able to successfully form neuromuscular junctions in the injury site, and notably, the ENC was able to effectively bridge the gap between the re-routed nerve and the surgical site in the majority of animals.

Histological Analysis of Muscles

We performed qualitative and quantitative histological analyses on midbelly PT cross-sections of both contralateral and surgical PT muscles. In all surgical groups, the repair site was characterized by a fibrotic region, as evidenced by the H&E staining (Figure 17A-D) and Masson's trichrome staining (Figure 17E-H). The blue regions in the sections stained with Masson's trichrome demonstrate the collagen deposition in the repair site. Immunostaining for myosin heavy chain and laminin (Figure 17I-L) showed that there was also laminin in the repair site. We did not qualitatively observe an obvious difference in the abundance of positive MF20 staining between groups when observing the muscle as a whole.

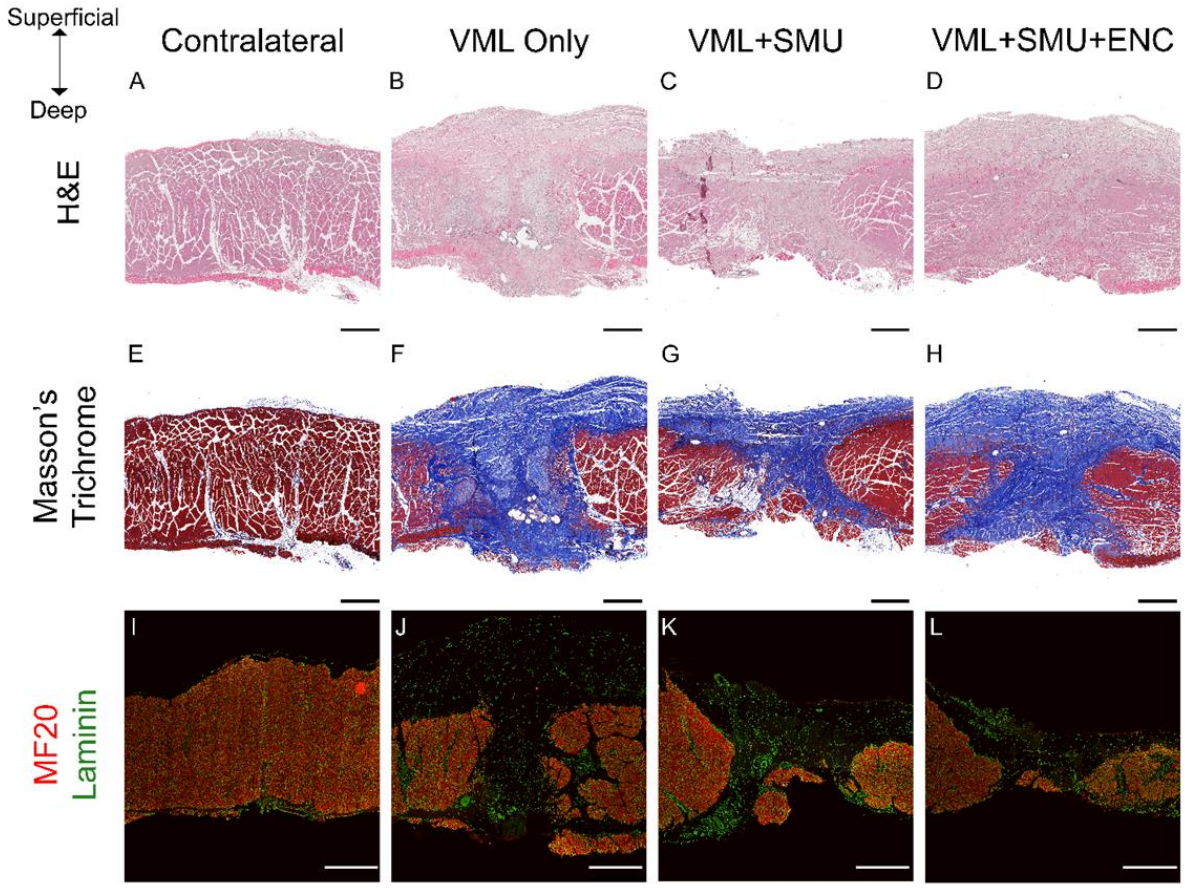

Figure 17. Gross Morphology of Explanted Muscle.

Cross sections of explants from contralateral (A,E,I), VML only (B,F,J), VML+SMU (C,G,K), and VML+SMU+ENC (D,H,L) groups were taken from the midbelly of the muscle. Tissues stained with H&E (A-D) show that the surgical site is characterized by the presence of disorganized, hypercellular tissue. Serial sections stained with Masson's trichrome (E,F,G,H) indicates that there are large fibrotic regions, evidenced by positive collagen staining (blue) that spans between the native muscle (red) in all surgical groups. (I,J,K,L) Immunostaining for myosin heavy chain (MF20, red) and laminin (green) show that muscle is absent in a large portion of the surgical site. Scale bars = 2 mm.

At higher magnifications, we noticed the presence of vasculature in the repair site of the H&E-stained sections of all experimental groups (Figure 18A-D). We also observed the presence of intramuscular fat near the repair site of the surgical groups, but not in the uninjured contralateral muscle (Figure 18A-D). Immunohistochemical staining for myosin heavy chain (MF20) and laminin revealed the presence of small muscle fibers within the repair site in the VML only, VML+SMU and VML+SMU+ENC groups (Figure 18E-H). The presence of these small muscle

fibers suggests that our SMUs are promoting muscle regeneration; however, the origin of these fibers has not been determined. We also noted the presence of neuromuscular junction formation in all experimental groups as evidenced by positive staining for acetylcholine receptors, synaptic vesicle protein-2, and neurofilament in longitudinal sections of the repair site (Figure 18I-L).

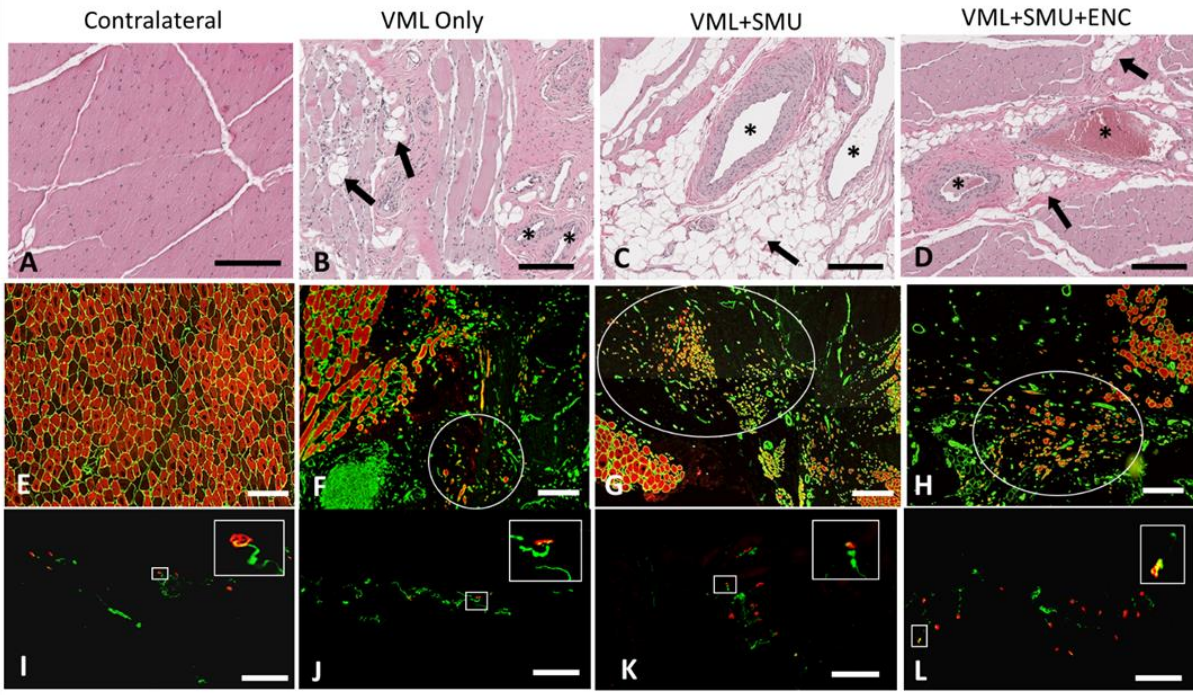

Figure 18. Microstructures of Explanted Muscle.

H&E-stained cross-sections of the repair site demonstrated the presence of fat (black arrows) in all surgical groups (B-D) compared to the contralateral (A). Furthermore, tissues stained with H&E (A-D) show that the repair site is characterized by what appears to be an increase in vasculature (asterisks) in all experimental groups compared to the contralateral muscle, although this was not quantified. Immunohistochemical staining for myosin heavy chain (MF20, red) and laminin (green) (E-H) revealed the presence of small muscle fibers within the repair site in the VML only (F), VML+SMU (G) and VML+SMU+ENC (H) as indicated by the white circle. (I-L) We noted the presence of neuromuscular junctions in the contralateral muscle as well as the surgical site of all experimental groups through immunostaining longitudinal sections for acetylcholine receptors (red), synaptic vesicle protein-2 (red), and neurofilament (green). The inserts show zoomed-in images of the neuromuscular junctions. Scale bars = 200 μm.

To quantitatively evaluate the collagen content of the muscles, we measured the percentage of positive Picrosirius Red staining (percent collagen) in midbelly cross-sections of the PT muscles (Figure19). We first verified this method by evaluating the collagen content of the uninjured contralateral muscles and found that they have very little variability in the percent collagen.

Specifically, the average percent collagen in the uninjured contralateral PTs was 17.6 ± 2.76% (n=23). In contrast, the average percent collagen in the surgical PTs was 46.0 ± 8.53%, 36.5 ± 4.54%, and 39.6 ± 9.18% for the VML only (n=7), VML+SMU (n=6), and VML+SMU+ENC (n=10) groups, respectively. The percent collagen of the surgical PT of the VML only group was significantly higher than the VML+SMU group (Sidak's MC: P<0.0323), which indicates that there was significantly more connective tissue deposition in the VML only group compared to the VML+SMU groups (Figure 19E).

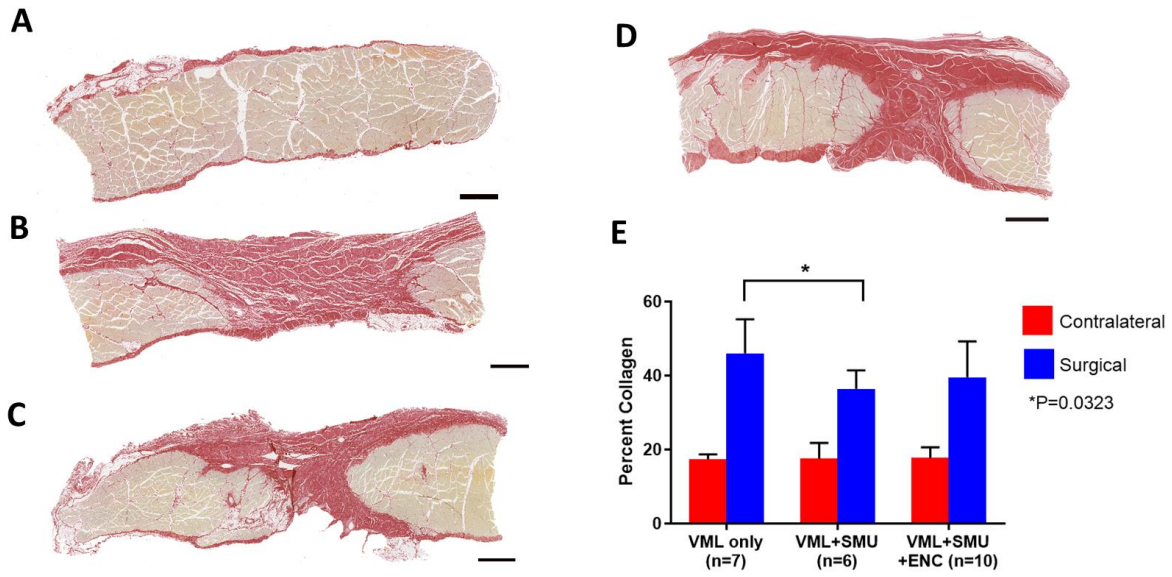

Figure 19. Analysis of Collagen Content in Explanted Muscle.

Midbelly PT cross-sections of the surgical sites of muscles in the (B) VML only, (C) VML +SMU, and (D) VML+SMU+ENC groups were stained with Picrosirius Red to evaluate the collagen content in the surgical site relative to (A) the uninjured contralateral muscle. (E) The percentage of positive Picrosirius Red staining relative to the total cross-sectional area (percentage of collagen) was measured using ImageJ. The surgical PT of the VML only group had a significantly greater percentage of collagen than the VML+SMU group (P=0.0323). * indicates P<0.05. Scale bars = 2mm.

Discussion

Currently, there is a lack of large animal models of volumetric muscle loss. Large animal models are especially important for both clinical relevance and to address the limitations of rodent models. Specifically, rodents do not typically present the clinical manifestations of fibrosis seen

in humans, and the small sizes of rodent models do not pose a significant challenge to vascular and neural regeneration and growth into the injury site [71, 81, 110]. Furthermore, the FDA recommends testing in both large and small animal models when seeking regulatory approval for a new technology [111]. Currently, the only large animal volumetric muscle loss models that exist are pigs [80, 112, 113], and dogs [114]. This study is novel in that it contributes a sheep model of volumetric muscle loss.

Much effort has been made to fabricate tissues on a scale that is clinically relevant to humans; however, scale-up remains one of the most significant technological challenges of tissue engineering to date [86]. The primary obstacle to scale-up is the nutrient requirements of the tissue. In larger, avascular engineered tissues, nutrient availability is limited by diffusion which can result in the formation of a necrotic core if nutrients cannot adequately penetrate the entire thickness of the construct [153, 217, 218]. Our approach utilizes a modular tissue scale-up in which individual engineered tissue units are combined just prior to implantation and allowed to fuse together which we have shown prevents the formation of a necrotic core *in vitro.* We combine this strategy with the concept of the "body as a bioreactor" to drive vascularization of our constructs *in vivo* to eliminate the need for pre-vascularization. Overall, this study constitutes a significant step towards development of a VML treatment that overcomes many of the obstacles associated with the scale-up of engineered tissues and which restores both muscle mass and force production to a level that is statistically indistinguishable from the uninjured contralateral muscles after only three months.

Specifically, we were able to use a larger culture surface and our modular fusion approach to scale-up and fabricate engineered muscles that were 14 ± 1cm long and approximately 1cm in diameter. Qualitatively, the monolayers showed a highly aligned and dense myotube network. Elongated and networking myotubes indicate native-like skeletal muscle cell differentiation.

Immunohistochemistry revealed that *in vitro* the SMUs contained a population of satellite cells after 3D formation. The presence of these Pax7+ cells may have improved the myogenic potential of our SMUs *in vivo* and contributed to the regeneration observed in these groups.

In addition, the presence of positively-stained DAPI cells throughout the *in vitro* construct indicated that the construct core was not necrotic which supports the use of the larger culture surface to fabricate larger single scaled-up SMUs. Evaluation of the contractile properties of our SMUs prior to implantation showed that the isometric force production consistently met our release criteria. In fact, many of the constructs far exceeded our expected release criteria for force production by 20 to 40-fold. Potential explanations for the considerable variation in tetanic forces may be due to the alignment of the myofibers since contractile function of the construct is determined by the muscle architecture. We are currently developing techniques to predict the functional potential our constructs non-invasively using methods previously described by Syverud et al. [208].

Notably, despite the allogeneic nature of the SMUs and ENCs used in this experiment, the animals receiving engineered tissues exhibited no signs of rejection. Furthermore, the *in vivo* results demonstrate the ability of our SMUs to restore both muscle mass and force production to a level that was statistically indistinguishable from the uninjured contralateral muscle after only 3 months. As a percentage of the contralateral, there was no significant difference in the percentage of mass recovery between the experimental groups. In contrast, as a percentage of the contralateral, the VML+SMU+ENC group experienced a significantly higher percent force recovery than the VML only group which suggests that the mass recovery experienced in all experimental groups cannot solely be attributed to connective tissue deposition in the defect site. This is further supported by the immunohistochemical analysis which revealed the presence of small muscle

fibers in the injury site of VML+SMU and VML+SMU+ENC groups to a higher degree than what was qualitatively observed in the VML only group.

The animals did experience skeletal growth during the 3-month recovery period as evidenced by changes in muscle dimensions, including increased muscle length, between the time of implantation and the time of explant. As the majority of sheep gained weight during the recovery period, this increase in muscle size may also be attributable to hypertrophy of the muscles as a result of increased weight load. The growth of the muscle may have influenced its recovery from the VML injury; however, the effect of the animals' growth would be equivalent in all experimental groups.

We also found that the VML only group had a significantly greater percentage of collagen within the muscle cross-section than the VML+SMU group. This suggests that the quality of the repair was lower in the VML only group and corroborates the greater force deficit observed in the VML only group compared to the VML+SMU group and the VML+SMU+ENC groups. Thus, when accounting for the expected mass deficit of the VML only group (as this group received no mass to fill the defect), the quality of the repair of the VML+SMU and VML+SMU+ENC groups is highlighted.

Notably, our results also demonstrate the ability of the ENCs to effectively treat a concomitant peripheral nerve injury by bridging the gap between the re-routed nerve and the repair site, as evidenced by direct stimulation of the re-routed nerve which elicited an action potential to the injury site in the majority of animals in the VML+SMU+ENC group. In particular, we were able to stimulate the re-routed nerve in a greater percentage of animals in the VML+SMU+ENC group (75% versus 25% in the VML+SMU group). We speculate that the reason the VML+SMU+ENC animals experienced greater success could be due to the fact that the re-routed

nerve was isolated from the inflammatory environment of the VML injury for some period of time compared to the VML+SMU group. In the VML+SMU group, it is possible that immediately placing the re-routed nerve in the inflammatory environment of the injury site may have promoted neuroma formation which occurs when neuronal regeneration takes place in the presence of fibrotic tissue formation [205]. In contrast, the additional time it took for the re-routed nerve in the VML+SMU+ENC group to grow into the injury site may have kept it sufficiently isolated from the inflammatory microenvironment of the VML injury and may have contributed to its success.

Conclusions

In conclusion, these results demonstrate a significant advancement to the field of skeletal muscle tissue engineering. We successfully scaled-up our technology by fabricating tissues of clinically relevant sizes and demonstrated their potential for mass and force recovery in an ovine model of volumetric muscle loss. In future experiments, we would like to explore the inclusion of additional functional assessments, such as gait analysis, range of motion assessments, and functional benchmarking prior to surgery. Any changes in gait, although not noted in this study, could have influenced the force-generating capacity of the PTs in both the uninjured contralateral muscle as well as the surgical PT, thereby skewing functional results. Future experiments will also aim to better understand the mechanism by which our constructs are aiding the repair process by tracking the migration of endogenous and exogenous cells in the repair site.

Chapter IV – A Tissue Engineering Approach to Repairing Craniofacial Volumetric Muscle Loss in Sheep

Introduction

Craniofacial disorders are often more complex and manifest differently compared to disorders of the trunk and extremities [96]. These facial disorders are often accompanied by a severe loss of skeletal muscle referred to as volumetric muscle loss. Volumetric muscle loss is the loss of 20-30% or more of muscle volume which exceeds the body's inherent capacity for regeneration and often results in persistent functional deficits and cosmetic deformity [72, 81, 176]. Craniomaxillofacial disorders including VML often necessitate surgical intervention. In fact, reconstructive maxillofacial surgery is the third most common reconstructive procedure performed in the US with over 200,000 surgeries performed annually [171]. Additionally, craniomaxillofacial injuries are common in both military and civilian medicine [172, 173, 219]. Soft tissue injuries including VML make up over half of the craniomaxillofacial injuries sustained by civilians [173] and the majority of craniomaxillofacial injuries sustained in combat [172]. Furthermore, craniomaxillofacial injuries make up over a quarter of all injuries sustained on the battlefield injuries and are often life threatening [172, 220].

Compared to extremity VML, craniofacial VML presents additional challenges to repair. Craniofacial muscle contributes to facial expression and requires more complex motion and synchrony than trunk and extremity muscles and is characterized by differences in both its extracellular matrix (ECM) and its satellite cell populations [104, 106, 178, 179, 181]. This

complexity in tissue structure likely contributes to the reduced regenerative capacity of craniofacial muscle compared to trunk and limb muscle [107]. In addition, the difference in embryonic origin between craniofacial muscles (derived from pharyngeal arch mesoderm) and muscles of the trunk and limbs (derived from somatic mesoderm) leads to differences in the muscle stem cell niche and differences in satellite cell phenotype. For example, all satellite cell populations express Pax7 but only those derived from trunk and limb muscles additionally express Pax3 [109]. Despite these differences, there are currently no animal models of craniofacial VML; studies to date have solely involved VML of the trunk and extremities [98].

Treatments for craniofacial VML have significant limitations. These options include muscle flaps and grafts, as well as fillers and prostheses [86, 87]. Muscle grafts and flaps involve the transplantation of healthy muscle tissue from an autogenic or allogenic donor and are limited by tissue availability and donor site morbidity [86, 87]. These approaches are also often limited by size and shape mismatches between the grafted muscle, generally obtained from the leg, and the defect site. The use of fillers and prostheses can address the size-shape mismatch by injecting or implanting biomaterials into the face to correct contour deformities or to bridge functional gaps in the muscle. However, the use of fillers and prostheses can be limited by suboptimal integration of the material and sustained inflammatory response at the repair site [87]. Significantly, despite this multitude of options, no treatments exist that can fully restore normal sensation, expression, and function of craniofacial muscle following VML [96]. Thus, novel treatments need to be developed to reduce the negative structural and psychological effects of facial VML as well as restore normal mechanical function.

In many facial reconstruction surgeries involving the treatment of VML, the zygomaticus major muscle (ZM) is targeted for repair or replacement. This is because of its role in facial

expression and its contribution to psychological wellbeing. The zygomaticus major is a superficial muscle that is responsible for pulling the corners of the mouth upward and backward during facial expression. Thus, reduced function of the ZM limits a person's ability to smile, and the impaired ability to smile has been associated with increased levels of depression [221]. Additionally, VML injuries of the ZM are often accompanied by cosmetic disfigurements which are associated with low self-esteem and increased apprehension about appearance [222]. This lack of satisfaction with physical appearance has a significant effect on social functioning, including a lower frequency of interpersonal behavior [74], making the repair or replacement of the ZM essential for improving quality of life in patients with facial VML.

In this study, we sought to address the gap in craniofacial VML knowledge by creating a large animal model of facial VML. We also sought to modularly scale our engineered skeletal muscle tissues and test their efficacy in repairing VML in a non-mechanically loaded facial muscle. We have previously demonstrated the effectiveness of the modular approach in large animal (sheep) models of tendon [167], ligament [168, 169], and skeletal muscle [170] repair. Herein, we sought to repair a 30% VML deficit in the ovine zygomaticus major muscle and assessed the structural and functional effects of the repair after a 2-month, 4-month, or 6-month recovery period.

Methods

Animal Care

All animal care procedures followed The Guide for Care and Use of Laboratory Animals [191], according to a protocol approved by the University of Michigan's Institutional Animal Care & Use Committee. In all instances, animals were first sedated through the administration of intramuscular xylazine (0.2 mg/kg) and then anesthetized through the administration of

intravenous propofol (8 mg/kg) and gaseous isoflurane at concentrations between 2-5% to maintain a deep plane of anesthesia. For survival procedures, the animals were fasted and a fentanyl patch (75 mcg/hr) was administered 24hrs prior to surgery. Additionally, the animals received a subcutaneous dose of carprofen (4 mg/kg) immediately after surgery with a subsequent dose administered 24hrs post-op as supplementary analgesia if needed. Perioperatively, an intravenous dose of cefazolin (20 mg/kg) was administered. The fentanyl patch was removed 48hrs after surgery. The animals were monitored daily for 10-14 days after surgery by University of Michigan veterinary staff. As a part of this daily health monitoring, the animals were monitored for signs of pain and changes in eating habits. Surgical staples were removed 10-14 days after surgery. For terminal procedures, all animals were euthanized through the administration of a lethal dose of sodium pentobarbital (195mg/kg) and subsequent bilateral pneumothorax.

Muscle Biopsy Collection

A single 4-month-old female Polypay sheep (Oswalt Farms, Vicksburg, MI) was the sole tissue donor for all engineered tissues in this experiment. The animal was euthanized as described above and the semimembranosus muscles were dissected under aseptic conditions. Biopsies were transported to the laboratory in chilled Dulbecco's phosphate-buffered saline (DPBS) supplemented with 2% antibiotic-antimycotic (ABAM) (Gibco, cat. no. 15240-062).

Cell Isolation

Muscle progenitor cells including satellite cells were isolated as described previously [126-128, 166, 170, 206-208]. Briefly, muscle biopsies between 3g and 3.5g were sanitized in 70% ethanol and finely minced with a razor blade. The minced muscle was placed under UV light for 5 minutes and subsequently added to a digestion solution composed of 2.3 mg/mL dispase (Thermo Fisher, cat. no. 17105-041) and 0.3 mg/mL collagenase type IV (Thermo Fisher, cat. no. 17104-

019). The mixture was incubated for a total of 2.5 hours at 37°C with constant agitation. Following enzymatic digestion, the resulting suspension was then filtered through a 100 µm mesh filter (Fisher Scientific, cat. no. 22-363-549) followed by filtration through a 40 µm mesh filter (Fisher Scientific, cat. no. 22-363-547) and centrifuged. The supernatant was discarded, and the cells were re-suspended in freezing medium (50% Dulbecco's Modified Eagle's Medium (DMEM), 40% fetal bovine serum, 10% dimethyl sulfoxide (DMSO), supplemented with 1% ABAM) at a concentration of 5,000,000 cells/mL. The cells were slowly frozen to -80ºC at a rate of -1ºC/minute and subsequently stored in liquid nitrogen until plating.

Establishment of Design Parameters

Zygomaticus major samples were taken from n=7 Polypay wethers (castrated males) that were euthanized as part of an unrelated study. Gross measurements of the muscle were taken. The whole muscle was dissected, weighed, and frozen for histology. We calculated the 95% confidence interval for the ZM weights and set the SMU weight goal to be 30% of that confidence interval. A set of SMUs was fabricated to establish a 95% confidence interval for SMU weights. Using these values, we calculated the number of single SMU units that would have to be modularly combined to completely fill the VML defect.

Construct Fabrication

Frozen cells were removed from liquid nitrogen and quickly thawed in a 37ºC water bath. The cell suspension was re-suspended in muscle growth medium (MGM) (60% F-12 Kaighn's Modification Nutrient Mixture (F12K; Gibco, cat. no. 21127-022), 24% DMEM, 15% fetal bovine serum (FBS; Gibco, cat. no. 10437-028), 2.4 ng/mL basic fibroblast growth factor (FGFb; PeproTech, Rocky Hill, NJ, cat. no. 100-18B), 1% ABAM, supplemented with an additional 10µL/mL of 1µM dexamethasone (DEX; Sigma, cat. No. D4902)) [126-128, 140, 206, 207] and

seeded at a density of 10,000 cells/cm^2 onto 150mm tissue culture dishes embedded with stainless steel pins positioned 9cm apart. The culture media was changed for the first time on day 4 followed by a Monday-Wednesday-Friday feeding schedule thereafter. On day 6, the media was switched to muscle differentiation media (MDM) (70% M199 (Gibco, cat. no. 11150-059), 23% DMEM, 6% FBS, 1% ABAM, 10μL/mL 1μM DEX, 1μL/mL insulin–transferrin–selenium-X (ITSX; Sigma, cat. no. I1884), and 0.72μL/mL of 50mM ascorbic acid 2-phosphate (Sigma, cat. no. A8960)) to promote differentiation [126-128, 140, 206, 207]. Monolayers began to spontaneously delaminate on days 10-12 and were fully rolled up by day 15. On day 15, two SMUs were combined onto one plate and pinned at 7cm to allow them to shrink down in length and fuse together. On day 18 or day 20 of the fabrication process, the constructs were implanted into the recipient sheep. Alternatively, a subset of SMUs was reserved for *in vitro* characterization.

In Vitro *Assessments of SMUs*

A subset of the SMUs was reserved for *in vitro* characterization including biomechanical testing and histology. Approximately 24-48 hours after 3D formation, contractile properties of the single SMUs (not modularly fused) were measured as described previously [126-128, 134, 140, 206-208]. Briefly, contractions were elicited through field stimulation with a platinum electrode and measured by an optical force transducer (World Precision Instruments, cat. no. SI-KG7A) secured to one end of the construct. Tetanic forces were elicited using a 1s train of 2.5ms pulses at 800, 900mA, and 1000mA and 90, 100, and 120 Hz and measured using custom LabVIEW 2012 software. After biomechanical testing, SMUs were coated in Tissue Freezing Medium (Fisher Scientific, cat. no. 15-183-13), frozen in dry ice-chilled isopentane, and subsequently cryosectioned at 10μm. Cryosections of SMUs were stained with hematoxylin and eosin (H&E) and Masson's trichrome (Polysciences Inc., cat. no. 25088-1) to examine morphological

characteristics of the SMUs, as well as immunohistochemically stained to identify the presence of myosin heavy chain (1:200 dilution, DSHB, cat. no. MF-20c), laminin (1:200 dilution, Abcam, cat. no. ab7463), desmin (1:200 dilution; Abcam, cat. no. 6322), and α-smooth muscle actin (1:100 dilution; Abcam, cat. no. ab5694) as described previously [127, 140, 166, 208].

Surgical Implantation

Animals used for the surgical implant procedures were 6-7-month-old Polypay wethers weighing 45-55kg. The animals were divided into two experimental groups: VML only (negative control, n=15) and VML+SMU (n=15) (Figure 20). The positive control used in this study was the uninjured contralateral ZM. On the day of surgery, the animals were weighed and then placed under a deep plane of anesthesia. A 10cm incision was made along the lateral aspect of the left side of the face (surgical side) and the platysma was reflected to expose the zygomaticus major muscle and the mandibular branch of the facial nerve. Gross measurements of the muscle were taken and a full-thickness longitudinal portion of the ZM constituting 30% of the total muscle volume was dissected (Figure 20A). This value was calculated by taking length, width, and thickness measurements of the muscle, converting volume to mass using the density of skeletal muscle ($1.06 g/cm^3$), and then removing mass until 30% of the total muscle mass was reached. In both groups, the mandibular branch of the facial nerve was transected and re-routed to site of injury and sutured in with 8-0 prolene suture (Ethicon Inc., cat. no 2775G). The VML Only animals (negative control) received the injury and nerve re-route without any additional repair (Figure 20B). In the VML+SMU group, the injury was immediately repaired by suturing a modularly fused SMU (2 individual tissue units) within the defect with 6-0 PDS II suture (Ethicon Inc., cat. no. Z432H) (Figure 20C-D). In the same way, the nerve was re-routed to the SMU, splayed, and sutured in with 8-0 prolene suture. In both groups, the skin was sutured closed with 4-0 PDS II

suture and the skin was stapled along the incision. All animals were monitored daily for 10-14 days after surgery and then returned to herd housing. The animals were allowed to recover for either two months (2mo.), four months (4mo.), or six months (6mo.) before explant procedures were conducted (n=10 animals per time point).

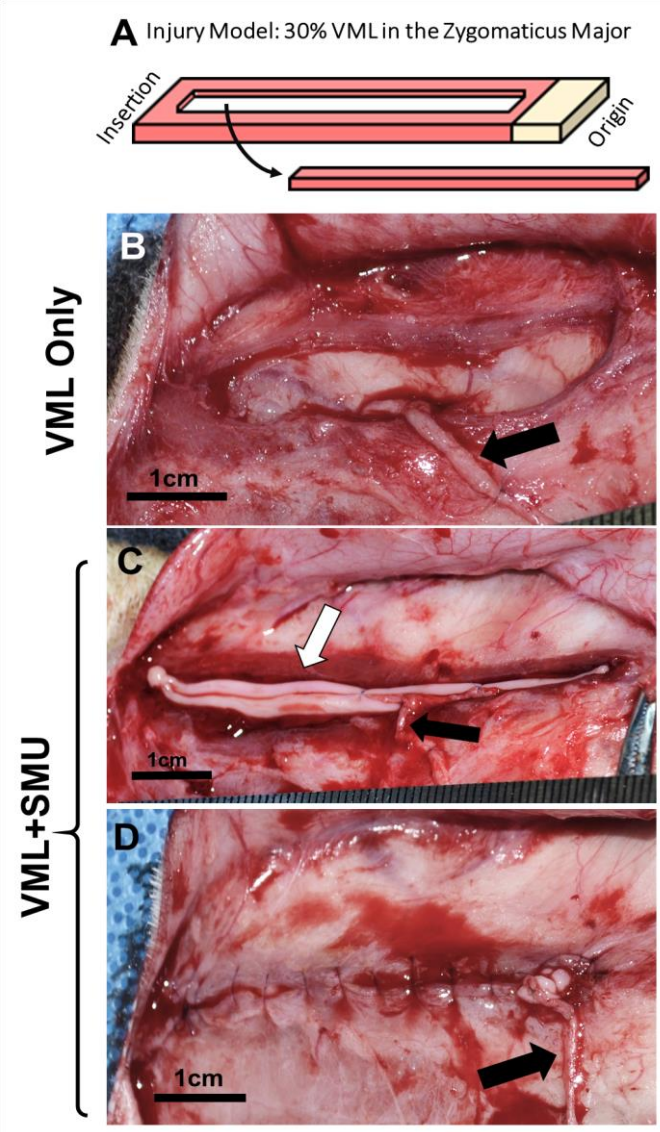

Figure 20. Sheep ZM Study: Experimental Groups.

(A) A full-thickness longitudinal portion of the ZM constituting 30% of the total mass was dissected to simulate a VML injury. (B) The VML Only group (negative control) received the injury and nerve re-route without any additional repair. (C) In the VML+SMU group, the injury was immediately repaired by placing n=2 single SMUs within the defect (white arrow). The re-routed nerve was splayed and sutured to the SMU. (D) The SMU was then sutured into defect site. Black arrows in B-D represent re-routed nerve.

In Situ Biomechanical Testing

Following the recovery period, animals were weighed and then placed under anesthesia. We conducted *in situ* biomechanical testing of both the contralateral and surgical ZMs using a custom biomechanical testing system. Both the contralateral and surgical ZMs were dissected leaving the proximal origin intact. The distal end of the ZM was secured to a strain gauge force transducer (World Precision Instruments, cat. no. FORT1000) to measure the force of the muscle contractions. Contractions were elicited through whole-muscle stimulation using a custom bipolar platinum bezel strip electrode. Biomechanical testing of the muscles was conducted as described previously [127, 170, 215, 216]. Briefly, the muscle was placed in the slack position and single 0.1ms pulses of increasing current amplitudes (i.e. 70, 80, 90, 100, 110, and 120mA) were delivered until peak twitch force was reached. Maintaining the current, the muscle length was subsequently adjusted to the length at which twitch force was maximal. The length of the muscle at which twitch force was maximal was defined as the optimal length (Lo). The stimulus was then switched to a tetanus in which a 600ms train of 0.1ms pulses were delivered. The frequency of these pulses was increased (i.e. 60, 80, 100, 120Hz) until isometric tetanic force was maximal. Data was recorded using custom LabVIEW 2018 software. This process was then repeated on the contralateral (uninjured) ZM muscle. Immediately after biomechanical testing, both the contralateral and surgical ZMs were fully dissected, weighed, and prepared for histology. The animals were subsequently euthanized.

Histology

After dissection, the muscles were weighed, and gross measurements were taken. The muscles were then divided into segments, coated in tissue freezing medium, and frozen in dry ice-chilled isopentane. Frozen samples were cryosectioned at 10μm and then stained with hematoxylin

and eosin (H&E) and Masson's trichrome (Polysciences Inc., cat. no. 25088-1) to examine morphological characteristics of the SMUs. Cross-sectional samples were also immunohistochemically stained to identify myosin heavy chain (1:200 dilution, DSHB, cat. no. MF-20c), laminin (1:200 dilution, Abcam, cat. no. ab7463), perilipin (1:200 dilution, Abcam cat. no. ab3526), fast myosin isoform (1:200 dilution, Abcam cat. no. ab91506), and slow myosin isoform (1:200 dilution, Abcam cat. no. ab11083) using a protocol described previously [127, 140, 166, 208]. Longitudinal samples were immunohistochemically stained for acetylcholine receptors (α-bungarotoxin, 1:2000 dilution, Life Technologies, cat. no. B1601), synaptic vesicle protein-2 (1:300 dilution, DSHB, cat. no. SV2c), and neurofilament (1:1000 dilution, BioLegend, cat. no. 837904) to identify the presence of neuromuscular junctions.

MF20+ Cross-Sectional Area and Specific Force

Midbelly cross-sections were stained for myosin heavy chain (MF20) to identify the presence of skeletal muscle fibers. The total area (cm^2) that was positively stained with MF20 was measured using ImageJ/Fiji. Because the ZM muscle fibers have no pennation angle [223], the physiological cross-sectional area used to calculate the specific force is equal to the cross-sectional area of the muscle. To calculate the specific force, the maximum tetanic force (N) of the muscles was divided by the MF20+ cross-sectional area (cm^2) to calculate the specific force (N/cm^2) of the muscle. These same images were also used to evaluate the small fibers present in the injury site. The number and cross-sectional area of all of the small fibers in the injury site was measured using ImageJ/Fiji in the 6-month recovery group animals.

Fiber Typing

A midbelly cross-section of each ZM was immunohistochemically stained for fast myosin isoform to identify the type II muscle fibers and slow myosin isoform to identify type I fibers. To

evaluate the percentage of the total muscle cross-sectional area that was type I fibers, the amount of area positively stained for slow myosin isoform was measured using ImageJ/Fiji. This value was divided by the total area of all muscle fibers which was also quantified using ImageJ/Fiji. To calculate the number of type I fibers relative to the total number of fibers, four regions that were 9.6mm^2 in area were chosen at random. In total, these areas constituted ~30% of the total muscle cross-sectional area. The number of fibers expressing slow myosin isoform (type I fibers) and the number of fibers expressing fast myosin isoform (type II fibers) were enumerated. This data was presented as the total number of slow fibers as a percentage of the total number of fibers enumerated. For this analysis, only animals in the 6-month recovery group were evaluated.

Intramuscular Fat

Midbelly cross-sections were also stained for perilipin to identify the presence of adipose within the muscle and within the repair site. The total area that was positively stained with perilipin was measured using ImageJ/Fiji. This value was divided by the cross-sectional area of the muscle to calculate the percentage of the area that was positively stained for perilipin.

Statistical Analysis

Statistical analyses were performed using GraphPad Prism software. To evaluate the effects of recovery timepoint and experimental group, values were first normalized to the contralateral muscle and differences were assessed with a two-way ANOVA with Sidak's multiple comparisons test (SMC). If no significant differences between recovery timepoints were present, statistical differences between experimental groups and between the contralateral and surgical muscles were assessed with a two-way repeated measures ANOVA (two-way RM ANOVA) and post-hoc Sidak's multiple comparisons test (SMC). The P-values for interaction and subject were not reported unless significant. Alternatively, a one-way ANOVA and Tukey's multiple

comparisons tests (TMC) were used to determine differences between groups. Results were significant at $P<0.05$. Bars on graphs indicate mean ± standard deviation.

Results

Establishing SMU Design Parameters

Native zygomaticus major samples were taken to inform the design parameters for this study and to determine the number of single SMUs that would have to be modularly combined to fill a 30% VML defect. The 95% confidence interval for the total ZM weights of n=7 animals was 2.0-2.4g. A group of n=12 SMUs was used to determine the 95% confidence interval for SMU weight which was 0.31-0.39g. Thus, we modularly combined n=2 SMUs to fill a 30% defect. The modular assembly is depicted in Figure 21A.

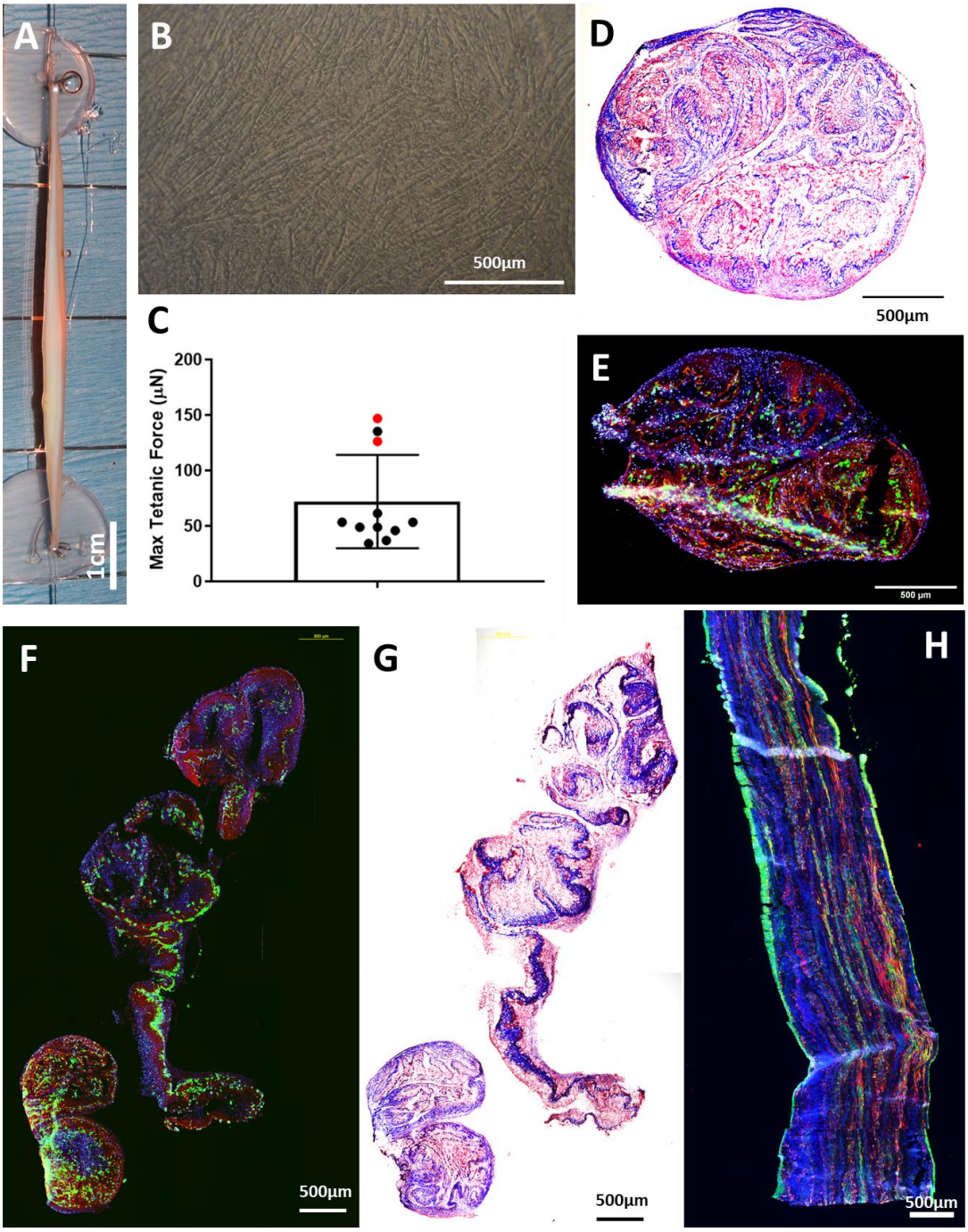

Figure 21. Characterization of In Vitro SMUs.

(A) The final modular assembly of n=2 SMUs was 7cm long. (B) SMU monolayers prior to delamination showed abundant, networking myotubes. (C) Tetanic forces produced by sentinel SMUs were 72.0 ± 42.1µN on average. Masson's trichrome staining of a single SMU cross-section (D) and modularly fused SMU cross-section (G) revealed an extracellular matrix composed of collagen. Immunohistochemical staining of a single SMU cross-section (E) and a modularly fused SMU (F) revealed the presence of muscle fibers (MF20, green) and laminin (red), as well as the absence of a necrotic core as evidenced by the present of DAPI-stained nuclei (blue) throughout the thickness of the construct. (H) Immunostaining of a longitudinal section of a single SMU for desmin (red), α-smooth muscle actin (green), and DAPI (blue) revealed a parallel, linear arrangement of these proteins. Scale bars on B, D-H = 500µm.

Evaluations of SMUs

Light microscopy of SMU monolayers revealed extensive myotube networking on day 11 just prior to delamination and 3D formation (Figure 21B). We evaluated the histological characteristics of SMUs through staining of both individual SMUs (Figure 21D-E,H) and modularly combined SMUs (Figure 21F-G). 24-48 hours after 3D formation, we evaluated the force production of n=11 single unit SMUs. The average tetanic force production of a single SMU was 72.0 ± 42.1μN, with the 95% confidence interval being 43.7-100.3μN. However, this is likely an underestimation of the maximum force production of the SMUs, as only n=2 SMUs peaked below the maximum current and/or frequency allowed by our force testing system (denoted in red, Figure 21C). It should be noted that all sentinel SMUs produced force and contracted following electrical stimulation.

Histological analyses of SMUs revealed muscle fibers present throughout both the single SMU units (Figure 21E) and modular SMUs (Figure 21F) indicating that the modular assembly of the SMUs did not negatively impact the presence of muscle fibers. The SMUs' extracellular matrix was composed of laminin which was identified immunohistochemically (Figure 21E-F) and collagen which was identified by the blue Masson's trichrome staining (Figure 21D,G). Immunohistochemical staining also revealed the absence of a necrotic core, as DAPI-stained nuclei were present throughout the full thickness of the construct. In longitudinal sections of a single SMU, we noted the presence of desmin and α-smooth muscle actin arranged linearly, parallel to the longitudinal axis of the SMU (Figure 21H). Positive staining for α-smooth muscle actin without desmin co-staining indicates the presence of myofibroblasts within the SMU.

Surgical Procedures

Across all timepoints, the average percentage of VML was 31.8 ± 7.1% in the VML Only group and 30.4 ± 6.1% in the VML+SMU group. A two-way ANOVA revealed that there were no significant differences in the size of the VML injuries between timepoints (P=0.5207, n=10 animals per timepoint) or between experimental groups (P=0.1424, n=15 animals per group) (Figure 22A). There were significant differences in the size of the modular SMUs across timepoints (one-way ANOVA: P=0.0002, n=5 modular SMUs per timepoint), with the 6mo. animals receiving significantly larger SMUs than the 2mo. (TMC: P=0.0006) or 4mo. (TMC: P=0.0003) animals (Figure 22B). On average, the weight of the modular SMUs was 0.41 ± 0.07g, 0.35 ± 0.02g, and 1.1 ± 0.35g for the 2mo., 4mo., and 6mo. groups, respectively. With regards to how much of the VML defect was replaced with an SMU, the defect was filled 106.6 ± 10.4%, 101.7 ± 4.7%, and 169.0 ± 25.7% in the 2mo., 4mo., and 6mo. groups, respectively (Figure 22C). The modular SMUs in the 6mo. group contributed significantly more mass to the defect compared to the SMUs in the 2mo. (TMC: P=0.0001) or 4mo. (TMC: P<0.0001) groups; however, only n=3 animals had a mass deficit remaining after SMU implantation, and this deficit was 6.5 ± 2.5%.

Although the SMUs implanted into the 6mo. animals were significantly larger than the other SMU cohorts, the fabrication protocol was identical for each cohort of SMUs and the cells used in their fabrication all came from the same donor animal. The difference in SMU size was due to faster cell growth such that after the monolayer delaminated to form an SMU, a subsequent monolayer grew and delaminated around the existing SMU by the time of implantation. Because the 6mo. cohort of SMUs was fabricated first, the cells spent the least amount of time frozen prior to SMU fabrication which likely accounts for the difference in the cells' growth rate.

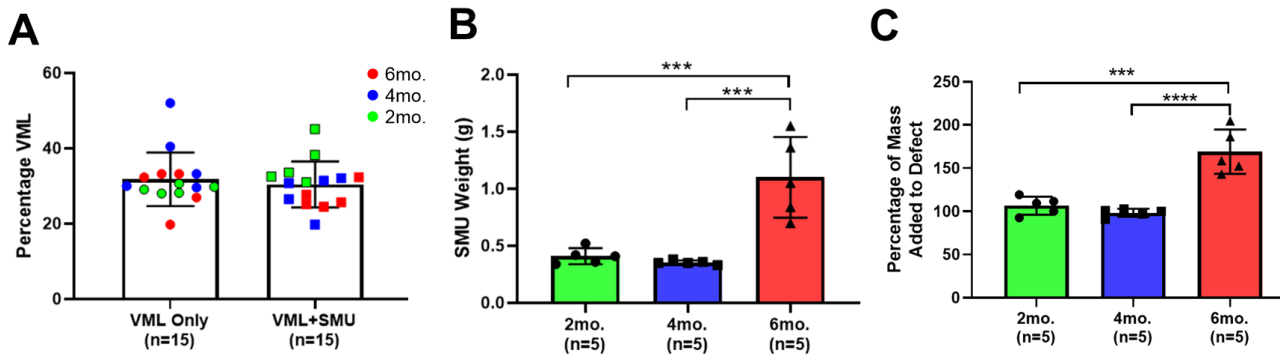

Figure 22. VML Injury and Size of SMUs.

(A) The average percentage of the VML injury was 31.8 ± 7.1% in the VML Only group and 30.41 ± 6.1% in the VML+SMU group. There were no significant differences in the size of the VML injuries between timepoints or between experimental groups (two-way ANOVA: P=0.5207 and P=0.1424, respectively). (B) The modular SMUs implanted into the 6mo. animals were significantly larger than those in the 2mo. (P=0.0006) or 4mo. (P=0.0003) groups and (C) contributed significantly more mass to the defect those in the 2mo. (P=0.0006) or 4mo. (P=0.0003) groups. *** indicates P ≤ 0.001; **** indicates P ≤ 0.0001.

Animal Health

Animals were awake, alert, and eating within two hours of completing surgery. None of the animals were observed to have abnormal eating habits after surgery, although n=9 out of 30 animals did exhibit signs of low-level amounts of pain, specifically evidenced by bruxism. All animals in the 4mo. and 6mo. recovery groups gained weight normally between the time of implantation and the time of explant. A paired two-way ANOVA performed for each recovery timepoint showed that the experimental group did not significantly affect the animals' body weight (P=0.6224 for the 2mo. group, P=0.4439 for the 4mo. group, P= 0.3054 for the 6mo. group, n=10 per group) (Figure 23). This implies that the surgical procedure was not significantly more stressful for one experimental group over another. As could be expected with growing animals, there was a significant difference in body weight between the time of implantation and the time of explant in the 4mo. (two-way RM ANOVA: P=0.0003) and 6mo. (two-way RM ANOVA: P<0.0001) groups, but not the 2mo. group (two-way RM ANOVA: P=0.6206). Notably, none of the animals exhibited

signs of a chronic immune response at the time of explant (i.e. white blood cell counts were within normal limits).

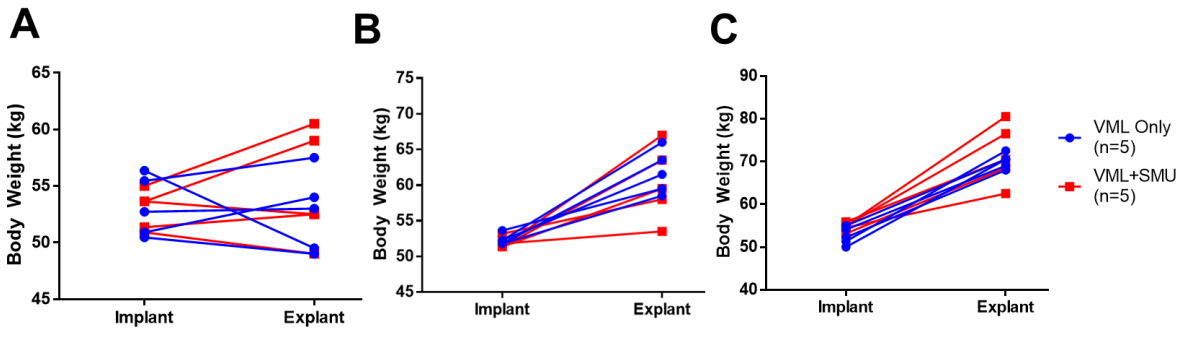

Figure 23. Animal Body Weight.

We measured the animals' body weight at the time of implantation and the time of explant for the (A) 2-month, (B) 4-month, and (C) 6-month recovery groups. A paired two-way ANOVA performed for each recovery timepoint showed that the experimental group did not significantly affect the animals' body weight (P=0.6224 for the 2mo. group, P=0.4439 for the 4mo. group, P= 0.3054 for the 6mo. group, n=10 per group). However, there was a significant difference in body weight between the time of implantation and the time of explant in the 4mo. (P=0.0003) and 6mo. (P<0.0001) groups, but not the 2mo. group (P=0.6206).

Gross Observations at Explant

In all animals at the time of explant, there was an abundance of connective tissue surrounding the surgical ZM and tethering it to surrounding tissues. The tethering was also evident during biomechanical testing. In some instances, we also noted severe atrophy and changes in gross morphology of the ZM muscle. A total of n=5 animals experienced severe muscle wasting in which histological analyses revealed there were little to no muscle fibers present in the midbelly of the muscle. This was likely the result of ischemia which led to coagulative necrosis [224] and would have been caused by damage to the vasculature supplying the ZM when the initial VML injury was created. These animals were excluded from biomechanical and histological analyses.

Mechanical Properties of Explanted Muscles

To evaluate the force capabilities of the injured ZMs, we measured the maximum tetanic force of the surgical ZM and that of the uninjured contralateral ZM (Figure 24A-B). We

represented the force production of the surgical ZM as a percentage of the force produced by the uninjured contralateral to evaluate the effect of the recovery timepoints and experimental group (Figure 24A). A two-way ANOVA showed there was no significant difference in force between timepoints (P=0.3576) or between experimental groups (P=0.3041). After removing 30% of the muscle, one might expect a minimum force production of 70% of the contralateral; however the force deficits were much more severe, with the average percentage of force being 51.2 ± 16.3% in the VML Only group (n=11) and 61.1 ± 24.6% in the VML+SMU group (n=12). Notably, n=4 animals in the VML+SMU group exceeded this 70% force capability, while no animals in the VML Only group exceeded this 70% force capability (Figure 24A). Given that the timepoints did not significantly affect the force, we used a paired two-way ANOVA and combined all recovery timepoints for the next statistical analysis. This analysis found that there was a significant difference in the force capabilities between the surgical and contralateral ZMs (P<0.0001) and no significant differences between experimental groups (P=0.1830) (Figure 24B). A Sidak's multiple comparisons test showed that in both experimental groups, the maximum tetanic force of the surgical ZM was significantly lower than the uninjured contralateral (P<0.0001 in both groups, n=11 for VML Only, n=12 for VML+SMU) (Figure 24B).

Interestingly, the percentage of the defect that the SMUs filled was not correlated with the percentage of force measured (Figure 24E). Although the SMUs in the 6mo. recovery group were significantly larger than the SMUs in the 2mo. or 4mo. groups, the was no correlation between the SMU weight as a percentage of the VML mass deficit and the percentage of force recovery (r = 0.1082, P=0.7379, n=12).

To evaluate any changes in the optimal length (Lo) of the muscle fibers within the injured ZMs muscles, we compared the Lo of the surgical and contralateral ZM muscles (Figure 24C-D).

Because fibers run from origin to insertion in facial muscle, the Lo of the muscle fibers is equal to the optimal length of the whole ZM muscle [223]. We represented the optimal length of the surgical ZM as a percentage of the optimal length of the uninjured contralateral muscle to evaluate the effect of the recovery timepoints and experimental group (Figure 24C). A paired two-way ANOVA revealed that there was no significant difference in optimal length between timepoints (P=0.2270) or between experimental groups (P=0.1905). Given there was no significant differences between recovery timepoints, we used a paired two-way ANOVA and combined all recovery timepoints for the next statistical analysis. This analysis found that there was a significant difference in the muscle's optimal length between the surgical and contralateral ZMs (P=0.0428) and no significant differences between experimental groups (P=0.2308) (Figure 24D). A Sidak's multiple comparisons test showed that in the VML+SMU group, the optimal length of the surgical ZM was significantly lower than the uninjured contralateral (P=0.0318, n=12), but there was no significant difference in the VML Only group (P=0.8424, n=10).

Regarding the frequency-force relationship, there were no significant differences in the frequency required to produce a maximum tetanus between injured and the uninjured ZMs. For the uninjured contralateral ZM, maximum tetanus was achieved at 114.0 ± 22.7 Hz. In the injured ZMs, maximum tetanus was achieved at a frequency of 113.6 ± 15.7Hz and 113.3 ± 22.3Hz in the VML Only and VML+SMU groups, respectively. Statistically, there was no significant difference between these groups (one-way ANOVA: P=0.9956), indicating that the force-frequency relationship of the muscles was unchanged.

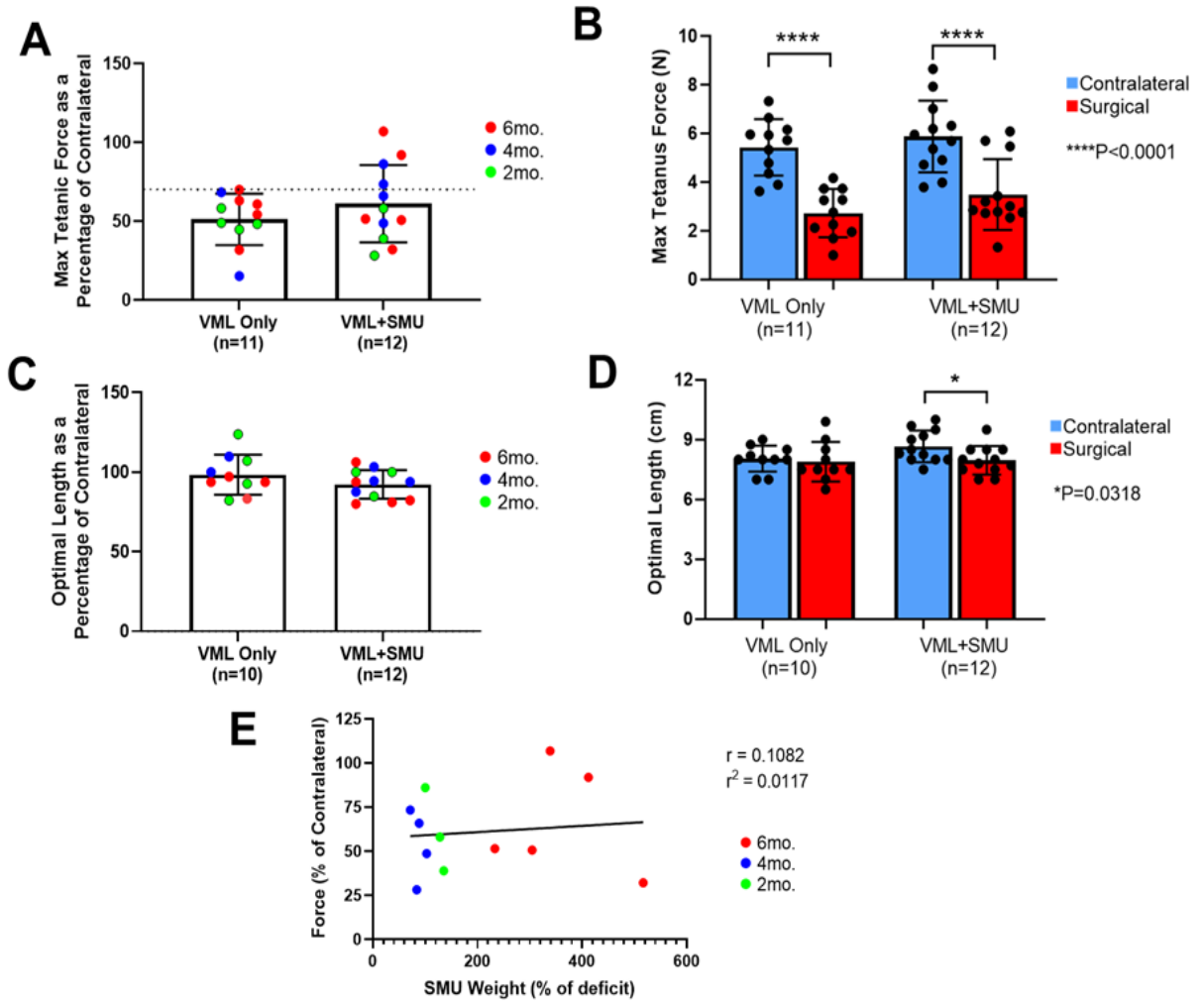

Figure 24. Mechanical Properties of Explanted Muscles.

(A) A two-way ANOVA showed there was no significant difference in force of the injured ZMs as a percentage of the contralalteral between timepoints (P=0.3576) or between experimental groups (P=0.3041). Notably, n=4 animals in the VML+SMU group exceeded 70% force capability (hashed line), while n=0 animals in the VML Only group exceeded 70% force capability. (B) In both experimental groups, the maximum tetanic force of the surgical ZM was significantly lower than the uninjured contralateral (P<0.0001 in both groups). (C) As a percentage of the contralateral, there was no difference in the optimal lengths of the muscle between recovery timepoints (P=0.2270) or experimental groups (P=0.1905). (D) There was no siginificant difference in the optimal length of the VML Only group realtive to the contralateral (P=0.8424), but the optimal length of the VML+SMU group was significantly lower than the contralateral (P=0.0318). (E) Interestingly, there was no correlation (r=0.1082) between the SMU weight (as a percentage of the mass deficit) and the percentage of force recovery (P=0.7379).

Muscle Cross-Sectional Area and Specific Force

To evaluate the quantity of muscle fibers present after the recovery period, we measured the cross-sectional area of the muscle by staining midbelly cross-sections of both the contralateral

and surgical ZMs for myosin heavy chain (MF20). We then calculated the area that was positively stained for MF20 using ImageJ/Fiji (Figure 25A-B). We normalized the MF20+ area of the surgical ZM to the contralateral and found that there was no significant difference in normalized MF20+ area between recovery timepoints (P=0.3462) or between experimental groups (P=0.7293). The average normalized MF20+ area was 57.4 ± 20.9% in the VML Only group (n=12) and 54.9 ± 13.4% in the VML+SMU group (n=13) (Figure 25A). Combining all timepoints, there was no significant difference between the experimental groups (two-way RM ANOVA: P=0.7481), but there was a significant difference between the contralateral and surgical ZMs (two-way RM ANOVA: P<0.0001) (Figure 25B). Using a Sidak's multiple comparisons test, there was a significant difference between the MF20+ area in the contralateral and surgical ZMs of both experimental groups (P<0.0001 for each group; n=12 for VML Only, n=13 for VML+SMU) indicating a deficit in the muscle CSA in both groups at the time of explant.

Because native ZM muscle fibers have no pennation angle [223], the physiological cross-sectional area used to calculate the specific force is equal to the cross-sectional area of the muscle. Thus, the MF20+ cross-sectional area discussed in the previous paragraph was used to calculate the specific force of the ZMs (Figure 25C-D). Normalized to the specific force of the contralateral, the mean normalized specific force was 96.8 ± 37.3% in the VML Only group (n=11) and 107.8 ± 34.3% in the VML+SMU group (n=12). A two-way ANOVA showed that there was no significant difference in the specific force as a percentage of the contralateral between timepoints (P=0.2247) or between experimental groups (P=0.3608). Given that the timepoints did not significantly affect normalized specific force, we combined all timepoints and found there was no significant difference in the specific force between experimental groups (P=0.1689) and between the contralateral and surgical ZMs (P=0.7789) using a paired two-way ANOVA. Notably, there was

no significant difference in the specific force between the surgical ZM and the uninjured contralateral ZM in both the VML Only (P=0.7653, n=11) and the VML+SMU (P=0.9529, n=12) group. Explicitly, the mean specific force of the contralateral, VML Only, and VML+SMU groups were 18.1 ± 4.8N/cm^2, 16.0 ± 5.0 N/cm^2, and 19.4 ± 6.3 N/cm^2, respectively.

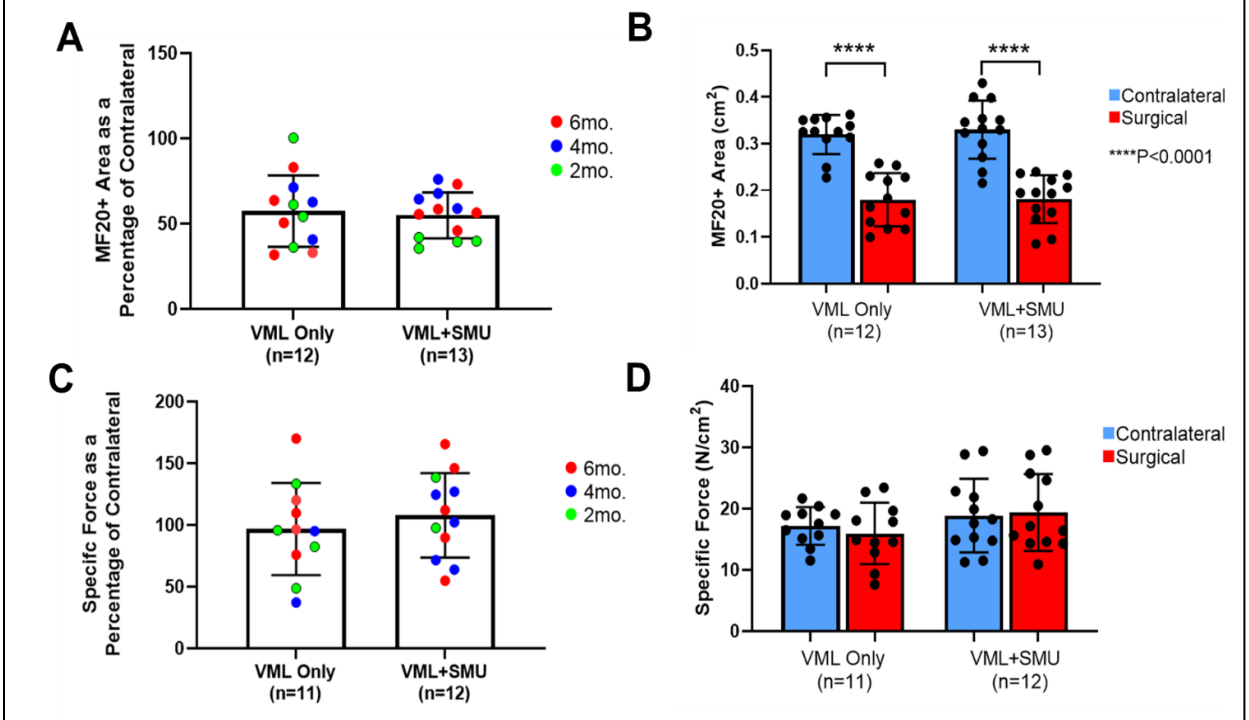

Figure 25. Specific Force.

(A) A two-way ANOVA showed there was no significant difference in normalized MF20+ area between recovery timepoints (P=0.3462) or between experimental groups (P=0.7293). (B) In both experimental groups, the MF20+ area of the surgical ZM was significantly lower than the uninjured contralateral (P<0.0001 in both groups, n=12 for VML Only, n=13 for VML+SMU). (C) There was no significant difference in normalized specific force between recovery timepoints (P=0.2247) or between experimental groups (P=0.3608). (D) Interestingly, in both experimental groups, there was no significant difference in specific force between the contralateral and surgical ZMs (P=0.7653, n=11 for VML Only; P=0.9529, n=12 for VML+SMU).

Histology of Explanted Muscles

We performed qualitative and quantitative histological analyses on midbelly ZM cross-sections of both the contralateral and surgical ZMs. Figure 26 depicts representative histology of animals in the 6mo. timepoint; we did not qualitatively observe differences in the histology across timepoints and for this reason chose to only present histology from the 6mo. recovery group;

however, histology of the 2mo. and 4mo. recovery groups can be found in the Appendix. In all surgical groups and at all timepoints, the injury site was characterized by a fibrotic region, as noted by the H&E staining (Figure 26A-C) and the Masson's trichrome staining (Figure 26D-F). The blue regions in Masson's trichrome-stained sections depict the collagen deposition in the injury site. Immunostaining for myosin heavy chain (MF20) and laminin (Figure 26G-I) showed that there were small muscle fibers and laminin in the injury site. The amount of MF20 staining was quantified and is depicted in Figure 25.

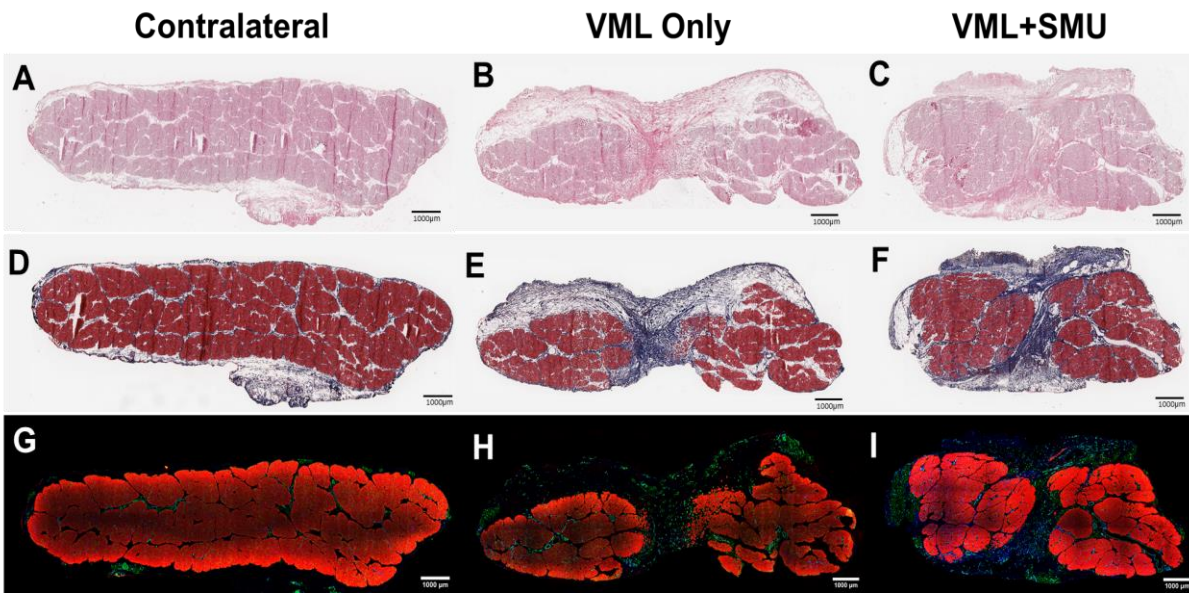

Figure 26. Histology at the 6-Month Recovery Timepoint.

Cross sections of explants from contralateral (A,D,G), VML only (B,E,H), and VML+SMU (C,F,I) groups were taken from the midbelly of the muscle. Tissues stained with H&E (A-C) show that the surgical site is characterized by the presence of disorganized, hypercellular tissue. Serial sections stained with Masson's trichrome (D-F) indicates that there are large fibrotic regions in the injury site, evidenced by positive collagen staining (blue) that spans between the native muscle (red) in the surgical groups (E,F). Immunostaining for myosin heavy chain (MF20, red) and laminin (green) (G-I) show that muscle is absent in a large portion of the surgical site.

We noted the presence of small muscle fibers in the injury site of all experimental groups and all recovery timepoints (Figure 27). Using the MF20 and laminin-stained sections, we quantified the number and size of the small fibers in the injury site of animals in the 6mo. recovery group. There were 58 ± 49 fibers in the injury site of animals in the VML Only group versus 183

± 197 fibers in the VML+SMU group; however, these values were not significantly different (P=0.1407, n=5 for VML Only, n=4 for VML+SMU). The cross-sectional area of these regenerated fibers was 672 ± 692μm^2 in the VML Only group and 560 ± 7510μm^2 in the VML+SMU group with the VML Only group having significantly larger fibers in the injury site than the VML+SMU group (P=0.0029, n=289 fibers for VML Only, n=916 fibers for VML+SMU). Although the VML Only group's fibers were larger, the origin of these fibers is unknown and these fibers could be from disrupted fascicles, rather than regenerating muscle. At the 6mo. timepoint, we also noted the presence of central nuclei in 80% of the animals in the VML only group (n=4/5 animals) and 100% of the animals in the VML+SMU group (n=5/5 animals) indicating that these muscle fibers were still regenerating even 6months after the initial injury.

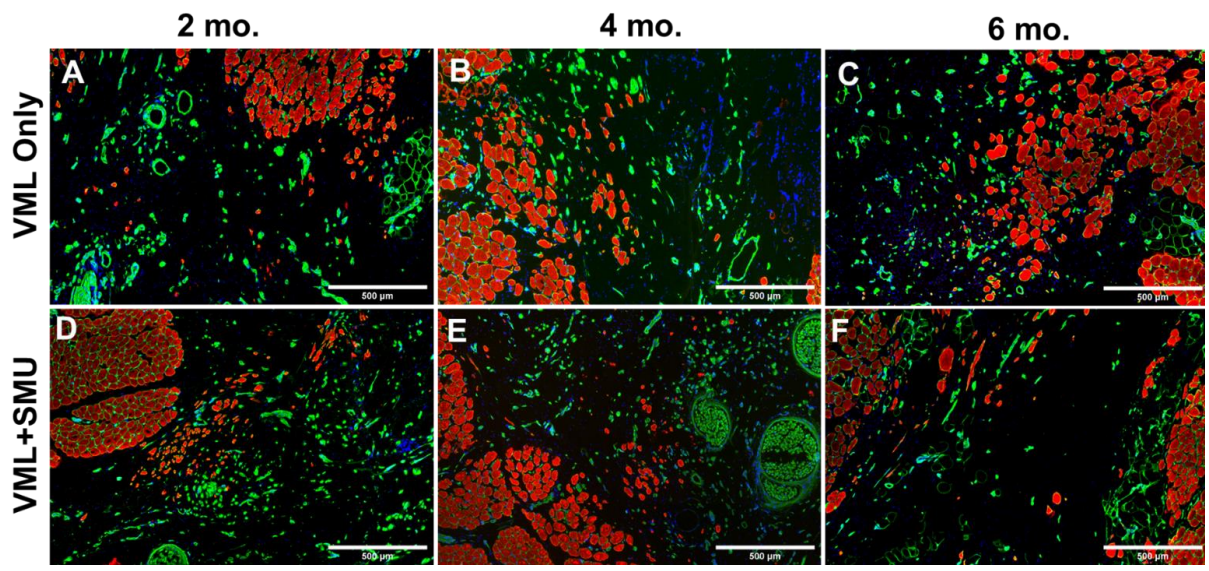

Figure 27. Small Muscle Fibers in the Injury Site.

Immunohistochemical staining for myosin heavy chain (MF20, red), laminin (green), and DAPI (blue) revealed the presence of small muscle fibers within the injury site in both the VML only (A-C) and VML+SMU (D-F) groups. These small fibers were noted at the 2-month (A,D), 4-month (B,E), and 6-month (C,F) recovery timepoints.

To evaluate innervation in the injury site, we immunohistochemically stained for the presence of neuromuscular junctions (NMJs) in the injury site and in the uninjured contralateral muscles (Figure 28). NMJs were observed in the contralateral ZM at all recovery timepoints, as well as both the VML Only and the VML+SMU groups at the 6mo. timepoint. Although acetyl choline receptors and neurofilament were present at earlier timepoints, small muscle fibers in the injury site do not appear to be fully reinnervated in the 2mo. and 4mo. recovery groups.

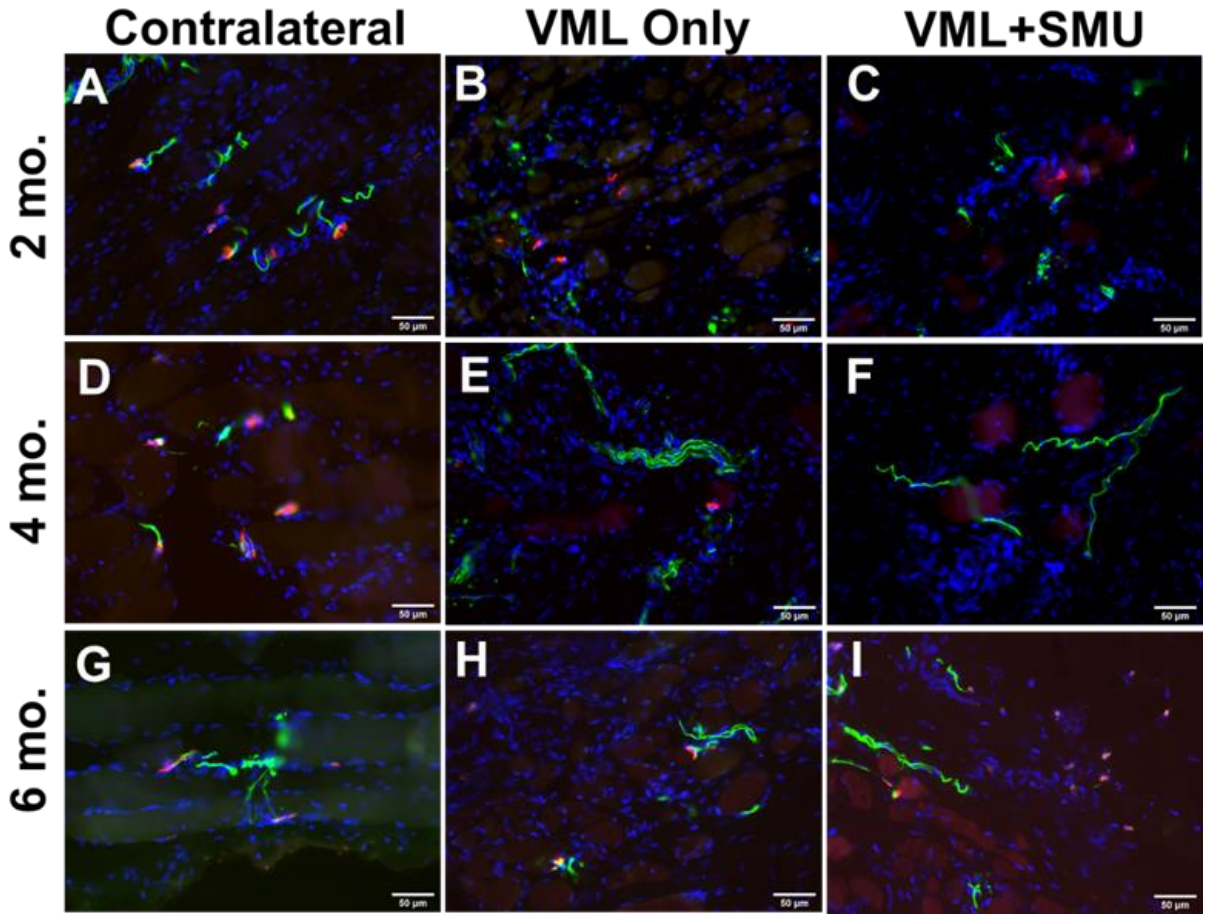

Figure 28. Neuromuscular Junctions in the Injury Site.

Immunostaining of longitudinal sections for acetylcholine receptors (red), synaptic vesicle protein-2 (green), and neurofilament (green) was performed to identify the presence of neuromuscular junctions. We noted the presence of neuromuscular junctions in the contralateral muscles (A,D,G) as well as the injury site of the (H) VML Only group and (I) VML+SMU group at the 6mo. timpeoint. The small muscle fibers in the injury site do not appear to be fully innvervated at the (B-C) 2mo. and (E-F) 4mo. timpeoints. Scale bars = 50 μm.

We also stained the muscles in the 6mo. recovery group for fast and slow myosin isoforms to see if there was any difference in the fiber type percentage and distribution relative to the contralateral. Histology revealed that there appears to be some difference in the fiber type composition in both the VML Only group and VML+SMU group relative to the contralateral (Figure 29A-C). We quantified the number of slow fibers as a percentage of the total number of fibers in n=5 animals per experimental group in the 6mo. recovery timepoint. We found that the mean percentage of the number of slow fibers was 37.1 ± 10.0% in the VML Only group and 40.0 ± 8.6% in the VML+SMU group, compared to the contralateral which was 27.9 ± 4.2%. However, these values were not significantly different (one-way ANOVA: P=0.0807, n=5 per group) (Figure 29D).

We also sought to determine the percentage of slow fibers constituting the total area of the muscle to give an indication as to the size of the fibers. The percentage of the area of slow fibers was 34.9 ± 15.5% in the VML Only group and 35.7 ± 11.6% in the VML+SMU group, compared to the contralateral which was 26.1 ± 6.2%. Again, these values were not significantly different (P=0.3852, n=5 per group) (Figure 29E). We also noticed considerable slow (type I) fiber grouping in 40% of animals (n=2/5) in the VML Only group and 100% of animals in the VML+SMU group (n=5/5). Fiber grouping indicates that portions of the muscle that remained after VML were denervated at the time of injury and explains the force deficits greater than 70%. A greater number of animals exhibited fiber type grouping in the VML+SMU group compared to the VML Only group which suggests that the denervation was more prevalent in this group, and thus the initial VML injury could have been more severe.

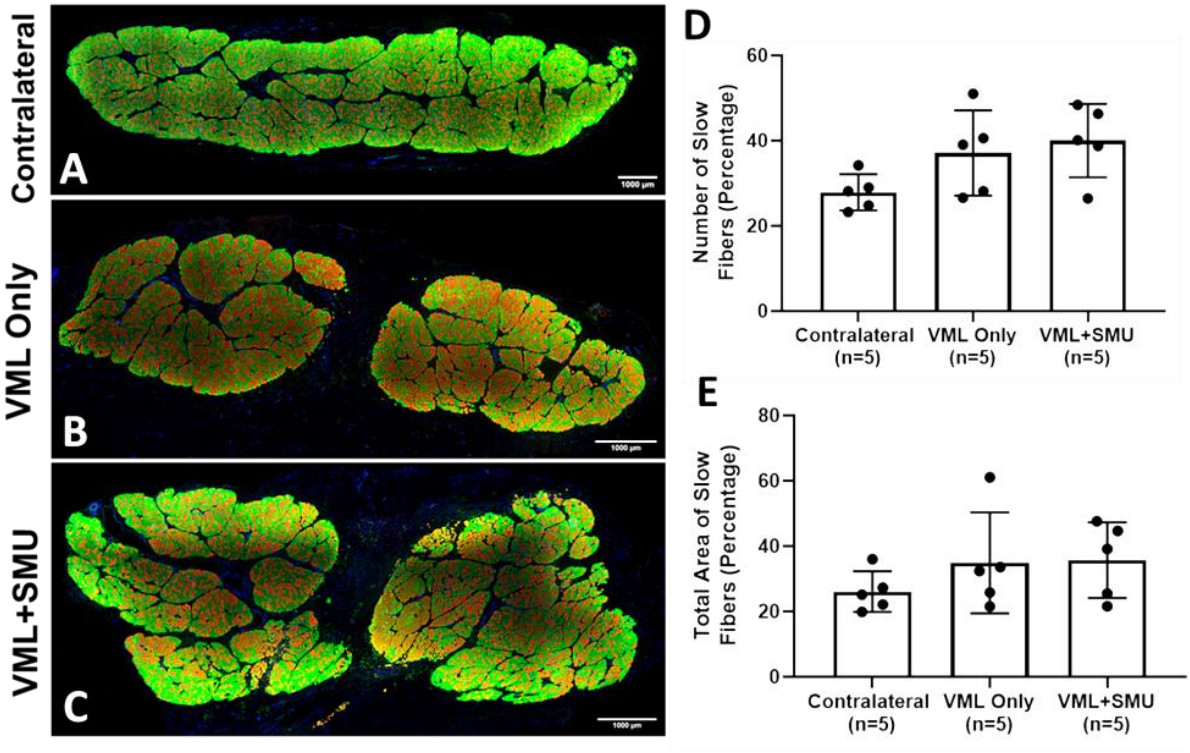

Figure 29. Fiber Type Analysis at the 6-Month Recovery Timepoint.

To note any changes to the fiber type of the msucle at the 6-month recovery timepoint, we performed immunostaining for fast myosin isoform (type II fibers, green) and slow myosin isoform (type I fibers, red) in the (A) contralateral, (B) VML Only, and (C) VML+SMU groups. Scale bars on A-C = 1000μm. (D) There was no significant difference in the percentage of the number of slow fibers between groups (P=0.0807). (E) There was no significant difference in the percentage of the total area made up by slow fibers between groups (P=0.3852).

To evaluate the abundance of intramuscular fat, we performed immunostaining for perilipin (Figure 30A-I). A two-way ANOVA revealed that the recovery timepoint did not significantly affect the fat content of the muscles (P=0.1396). Combining the recovery timepoints, differences in fat content between experimental groups were significant (one-way ANOVA: P=0.0224), and the VML+SMU group had a significantly higher fat content than the contralateral muscles (TMC: P=0.0334) (Figure 30J). Specifically, the fat content in the VML+SMU group was 2.07 ± 1.4% (n=13), while the fat content was 1.09 ± 0.58% in the contralateral muscles (n=12) and 1.18 ± 0.46% in the VML Only group (n=12). Because increased intramuscular fat content is associated with various pathologies including denervation [83], the significantly higher fat content

in the VML+SMU group corroborates the hypothesis that the denervation in the VML+SMU group was more severe than the denervation of the VML Only group.

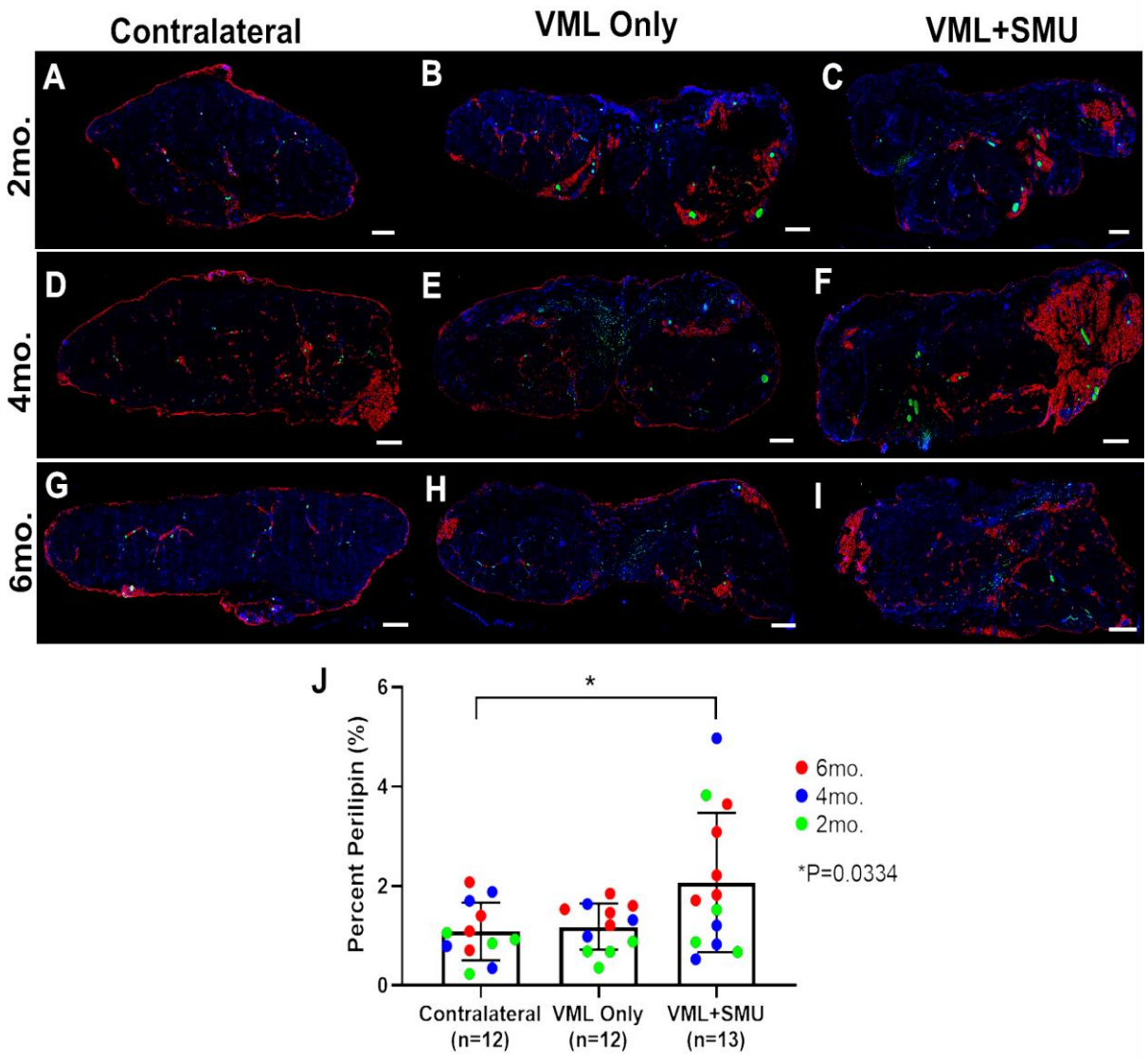

Figure 30. Intramuscular Fat.

(A-I) Immunostaining for neurofilament (SMI312, green) and fat (perilipin, red) in muscle cross-sections showed the presence of intramuscular fat and nerve in the explanted muscles. Scale bars = 1000μm. (J) There was a significantly higher amount of intramuscular fat in the VML+SMU group compared to the contralateral muscle (P=0.0334), while there was no significant difference in the amount of intramuscular fat between the VML Only group and the contralateral (P=0.9666).

Discussion

This study aimed to evaluate the effects of our engineered skeletal muscle tissue in repairing a craniofacial VML injury. The literature suggests that craniofacial VML would manifest differently than trunk and extremity VML for reasons including heterogeneity of both satellite cell populations [178, 179] and ECM [104, 106], differences in regenerative capacities [107], and differences in embryonic origin between craniofacial and trunk and limb muscle [109], as well as the documented complexity of craniofacial disorders relative to trunk and limb disorders [1]. Despite the notable differences between craniofacial muscle and trunk and limb muscle, all VML studies to date have involved VML models in trunk and extremity muscles [98]. This study sought to address this knowledge gap by introducing a large animal model of facial VML. Explicitly, the model used in this study was a 30% VML injury in the ovine zygomaticus major muscle.

While the SMU grafts did not result in significantly improved outcomes relative to the VML Only group, the SMUs did not negatively impact the functional recovery. In fact, the mean force production and specific force (both as a percentage of the contralateral) was higher in the VML+SMU group compared to the VML Only group. Furthermore, a total of n=4 VML+SMU animals versus n=0 VML Only animals achieved force capabilities greater than 70% of the force generated by the contralateral. This suggests that our SMUs are positively contributing to the functional recovery of the muscle, and the efficacy would likely be more apparent in a less severe injury model (i.e. without the comorbidities of ischemia and denervation).

Although 30% of the muscle was removed, force capabilities ranged from 15% to 70% of the uninjured contralateral in the VML Only group compared to 28% to 107% in the VML+SMU group. The presence of strength deficits exceeding the percentage of tissue removed was unsurprising, as strength deficits greater than the loss of tissue are a hallmark of VML injuries and

are evident both clinically and in animal models of VML [71, 81]. Muscle tethering and increased tissue stiffness are noted contributors to these strength deficits and were qualitatively observed to varying degrees during biomechanical testing of the injured tissues. The significantly lower optimal length of the muscle fibers within the ZM in the VML+SMU group relative to the contralateral muscles was also expected, as decreased fiber length is suspected to occur following VML injury and decreasing the number of sarcomeres in series decreases the optimal length of the muscle as a whole [30, 81].

Our results also reaffirm that a nerve re-route alone is not sufficient to recover muscle structure and function following VML injury. A previous study in a rat VML model showed that even with a nerve re-route, the unrepaired VML group exhibited significantly lower maximum force production compared to the uninjured contralateral muscles [127]. Similarly, all animals in this study received a nerve re-route directly to the injury site, but this treatment was not enough to recover force production to the level of the contralateral. Furthermore, fully formed neuromuscular junctions were not present at the 2mo. or 4mo. recovery timepoints but were noted at the 6mo. recovery point in both experimental groups, suggesting that a minimum of 6 months of recovery is necessary to obtain functional reinnervation in this facial VML model. Studies have shown that inflammatory environments can prevent nerve growth and result in the formation of neuromas if regeneration occurs during fibrotic tissue deposition [205]. Thus, inflammation may have prevented reinnervation and contributed to the notable force deficits regardless of the length of the recovery period.

Despite an identical volume of muscle removed in our previous study [170], the geometry and location of the VML injury induced in this study may have created comorbidities that increased the severity of the injury and contributed to variability within groups. Specifically, as is common

in extremity models, we chose to dissect a full thickness longitudinal portion of the ZM constituting 30% of the muscle mass (Figure 20A). In the native ZM, the vasculature inserts on the deep side of the muscle which made it difficult to create the VML injury without damaging the vascular bundle. Indeed, despite our attempts to avoid injuring native vasculature, in some instances, bleeding occurred during the muscle removal. We believe this injury led to ischemia that caused coagulative necrosis of the muscle in n=5/30 animals, resulting in virtually no muscle fibers present in the midbelly of the ZM at the time of explant. It is well understood that ischemia leads to muscle necrosis, and total muscle necrosis can occur if ischemia occurs for prolonged periods of time [224, 225]. Thus, the variability within groups may be related to variability in the severity of damage to the native vasculature. Moreover, if vascular damage led to necrosis of the remaining native muscle, it could have prevented survival of the SMU as well, as viability of implanted engineered tissues is dependent on rapid vascularization of the construct by the surrounding tissue [156].

Additionally, the results showed evidence of peripheral nerve damage. A study on the location of motor end plates (MEPs) in human facial muscle samples found that MEPs are located at four different places along the ZM (see Figure 2b of reference [223]). The location of our VML injury relative to the MEPs suggests that the muscle resection potentially created a denervation injury in the remaining muscle. This is corroborated by the notable type I fiber grouping, an indication of denervation and subsequent reinnervation, that was observed in n=7/10 animals in the 6mo. recovery group. Because there are microscopic variations in the locations of native MEPs between individuals, the extent of the damage to the nerve was likely variable between animals which could explain the variability in the functional recovery of the animals within experimental groups.

Overall, our results suggest that variability in the severity of the initial injury may have differentially affected the experimental groups. Although there was no significant difference in the volume of muscle removed between experimental groups and between timepoints, it is possible that there were differences in the degree of denervation and/or ischemia both between and within groups. Specifically, the more prevalent type I fiber grouping in the 6mo. VML+SMU group and the significantly higher fat content of the VML+SMU group than the VML Only group implies that the denervation injury may have been more severe in the VML+SMU group. Variability in the severity of the injury could also explain why SMU mass did not correlate with functional outcomes and why the larger mass of the 6mo. SMUs did not result in improved functional recovery compared to the 2mo. and 4mo. groups.

Although the data showed high variability within experimental groups, inconsistency in the therapeutic response of VML treatments involving engineered muscle tissue is not unique to this study. A study by Corona et al. showed that only 46% of the animals treated with their engineered tissue exhibited significant functional recovery compared to the unrepaired controls [226]. They believe the reason for this variability was damage to the construct during handling and implantation [226]; however, this was addressed in a follow-up study and a variable response to VML repair was observed once again, despite improved outcomes (67% of animals demonstrated significant functional recovery) [227]. They suggested the reason for this was due to a change in the geometry of the VML injury model which used the same percentage of VML but changed the dimensions of the injury to make it more shallow [227]. They believe this geometry led to improved cell migration and nutrient flow; however, it is also possible that a shallower injury may have simply disrupted the native nerve and vasculature to a lesser extent than in their previous

study. This highlights the difficulties associated with controlling the severity of a VML injury and with creating a model with a geometry that minimizes damage to native nerve and vasculature.

Conclusions

In sum, while our injury model was representative of clinical manifestations of VML, the ischemia and denervation in addition to the loss of muscle was likely too severe of an injury for our engineered tissues to overcome. While the inclusion of comorbidities is more clinically realistic, they create additional variables to control for and can create a source of variation that makes it difficult to evaluate the efficacy of a therapy. For this reason, the majority of researchers choose not to include common comorbidities such as peripheral nerve injuries in their VML models [71]. In fact, a meta-analysis of the efficacy of various VML therapies chose not to consider the effects of denervation or vascular disruption in their analysis [98]. As a result, it is difficult to truly understand how engineered skeletal muscle tissue would perform in the treatment of clinical manifestations of craniofacial VML. This study highlights the importance of balancing the use of a clinically realistic model while also maintaining control over variables related to the severity of the injury. These variables include the volume of muscle removed, the location of the VML injury, and the geometry of the injury, as these affect both the muscle's ability to self-regenerate as well as the probability of success of the treatment. Future directions will move away from full-thickness VML models and utilize an injury geometry that avoids the bulk of native nerve and vasculature.

Chapter V – Conclusions

The overall goal of my thesis was to conduct translational research that would bring our tissue-engineered skeletal muscle a step closer to reaching the clinic. Although our SMUs have shown promising regenerative potential in rat models of VML, we had not previously attempted to scale the SMUs to human sizes. Additionally, the regenerative potential of SMUs in a large animal VML model was unknown. Herein, we identified the effect of cell source on SMU structure and function, applied a modular method of scale up to engineered skeletal muscle tissues while avoiding necrosis, and tested our SMUs in two large animal implantation studies. In doing so, we introduced the sheep as a new large animal VML model, and we introduced the first craniofacial model of VML.

Contributions to the Field of Skeletal Muscle Tissue Engineering

In my thesis work, one aspect we sought to consider was the noted differences in satellite cell populations, developmental programs, and regenerative capacities of craniofacial muscle compared to trunk and limb muscle sources [107, 146, 178-181]. Despite the abundance of research regarding these substantial differences, engineered skeletal muscle tissues are almost exclusively fabricated from cells derived from hindlimb muscle, making the effect of cell source on engineered muscle tissue unknown. Thus, we conducted an empirical comparison of SMUs fabricated from both craniofacial and hindlimb muscle sources and evaluated the effects of the cell source on SMU structure and function (Chapter II). Ultimately, our results showed that the cell source significantly affected the structure and function of our SMUs. Specifically, the study

demonstrated that the zygomaticus major, a craniofacial muscle, produced SMUs with the lowest average force production and was hence not an appropriate cell source for engineered tissue. Conversely, the semimembranosus (SM), a hindlimb muscle, was the most clinically relevant muscle source, and SMUs fabricated from the SM exhibited the highest myotube density. This information led to the decision to use the SM as the cell source in both of the large animal implantation studies described herein.

For the field of tissue engineering, one of the most significant technical obstacles is the fabrication of the tissues of clinically relevant sizes. Tissue scale-up is a challenge because diffusive nutrient penetration is limited to several hundred microns in avascular tissue [152]. Thus, a necrotic core forms when the tissue is sufficiently large and nutrients cannot adequately diffuse to the center. There are several methods of scale-up that address nutrient availability to the core of the tissue including *in vitro* prevascularization [156, 159, 228], the use of oxygen-generating biomaterials [229, 230], and the use of decellularized cadaveric or xenogenic organs that have preserved vascular architecture [158, 231]; however, these methods can be costly, time-consuming, and inefficient [156, 231]. In this work, we addressed these limitations by implementing a low-cost modular approach to scale-up which avoids the formation of a necrotic core. To our knowledge, this method has led to the *in vitro* fabrication of the largest engineered skeletal muscle tissues to date and has made a significant contribution to the field of tissue engineering by providing an alternative method of scale-up that can be applied to a range of different tissue engineered technologies.

The successful scale-up of our SMU technology allowed us to transition to a large animal model for implantation studies that would address the limitations of rodent models. Rodent-sized SMUs are not only too small to be suitable in most human VML cases, but aspects of rodent

regeneration and wound healing prevent them from being accurate representations of VML in human patients. Specifically, the small sizes of rodent models and their relatively high innate capacity for regeneration do not sufficiently challenge vascular, neural, and muscular regeneration [71, 81, 110]. For example, rodents require a 40% VML to result in sustained functional deficits after 3 months, compared to 20-30% in humans, and do not present the clinical manifestation of fibrosis seen in human patients [71, 81, 110]. Thus, it was necessary to transition to a more clinically relevant animal model to address these concerns.

Despite the obvious need for large animal VML models, there are surprisingly few large animal studies of VML. A single research group is responsible for all of the pig VML studies that have been performed [80, 112, 113], and the only other large animal VML study was performed using a dog model [114]. Limitations of these models include ethical concerns, ease of handling, and cost. Additionally, our institution has a unique facility that is entirely devoted to sheep research which allows sheep to be housed in a farm-like environment that permits greater freedom of motion that would have not been possible with pigs. Thus, the choice of a sheep model not only addressed the limitations of other animal models, but our sheep facility allows for a more realistic mechanical loading environment during the animals' recovery. Contributing another large animal model to VML research is also beneficial because research conducted using a variety of animal models yields more thorough insights into pathology and regenerative mechanisms that can better predict what occurs in human patients [232].

The results of the muscle cell source study (Chapter II) further emphasized the heterogeneity of cell populations between muscle sources; however there are also reported differences in regenerative capacity and the manifestation of disease between craniofacial muscle and trunk and limb muscle [233-235]. Despite these differences, there are currently no models of

craniofacial VML in either large or small animal models. Thus, we sought to address this gap by introducing the first model of craniofacial VML and by documenting its pathophysiology. Indeed, differences in pathophysiology between craniofacial and limb VML were stark in the two implantation studies. Despite the use of the same injury and repair model in both studies (i.e. the same percentage of VML and the same injury geometry), there was a much stronger fibrotic response in the facial muscle. We also observed tissue tethering and intramuscular fat deposition in the facial muscle study that was not observed in the hindlimb study. Hopefully, the results from our first craniofacial VML study will prompt more studies that will specifically address the unique pathophysiology of craniofacial VML.

This work has also shown that our SMUs were able to restore muscle function to an even greater extent than what we have demonstrated in previous rat studies. In our previous rat study, the SMU-treated group experienced significantly greater force recovery than the VML only group after a 28-day recovery; however, forces were still significantly lower than the uninjured control muscles [127]. In contrast, SMU treatment was even more efficacious in the sheep PT study (Chapter III) in that SMU-treated groups were able to restore both muscle mass and force production to a level that was statistically indistinguishable from the uninjured contralateral muscles. To put the efficacy of SMU-treatment into perspective, our rat study was evaluated as part of a systematic review and meta-analysis performed by Greising et al. [98]. This study compared the efficacy of novel VML therapies from 44 different studies and found that less than 10% of therapies have high effect sizes, meaning treatment made a significant impact on force recovery. Our previous rat study is one of these high effect size treatments. The magnitude of recovered force was even greater in the PT study, making SMUs one the most efficacious novel therapies currently being developed.

Overall, the success of our technology demonstrates its potential for treating clinical VML in the future. In addition to the efficacy of SMU repair, the technology addresses the significant issues of donor site morbidity and tissue availability that are limitations of current treatments and also provides an opportunity for personalized medicine. Specifically, our fabrication method provides an opportunity for the tissue to be manufactured to the exact geometry of the patient's defect, thereby eliminating the issue of size and shape mismatch. Furthermore, the technology could be fabricated as an autograft, eliminating the possibility of an immune response and making it subject to fewer FDA safety regulations.

Future Directions in the Development of SMU Technology

Total recapitulation of native tissue structure and function remains a challenge across all methods of tissue engineering [236, 237]. Indeed, our SMUs do not exhibit the precise structural organization or functional capacity of native adult skeletal muscle; however, modifications to our fabrication process could make the SMUs more native-like in their phenotype. Other research groups have used dynamic and/or static mechanical conditioning [238-240], electrical stimulation [241, 242], chemical cues such as growth factors [128, 133, 243], and topographical features [129, 130, 132, 136] to alter cell behavior and direct the tissue towards a more native-like phenotype. While there are many ways to improve the phenotype of engineered tissues, using topographical cues to enhance myotube alignment is a promising option.

The use of topographical cues involves the incorporation of patterns into the tissue culture substratum to organize cell development in a direction parallel to the force-producing axis. Promoting adequate myotube alignment not only helps recapitulate native muscle structure, but it also has important physiological ramifications. For example, promoting alignment *in vitro* has been shown to enhance myogenic differentiation, upregulate contractile proteins, and promote the

formation of advanced sarcomeric structure [131, 132, 244, 245]. Functionally, alignment is important because misaligned myotube networks can produce contractile forces in opposing directions, reducing the net contractility of the engineered tissue. Currently, our technology promotes myotube alignment through passive tension of the constraint pins on the 3D tissue, but we do not specifically direct myotube alignment prior to delamination of the monolayer. Thus, it is possible that SMU phenotype could be enhanced if alignment was promoted prior to 3D formation of SMUs and it should be explored as a potential next step.

With regards to *in vivo* research, currently a third of VML studies utilize a "full-thickness" VML injury model [98]. Results from our studies have suggested that a full-thickness model can create concomitant denervation and ischemia injuries that increase the severity of the model and contribute to variability within experimental groups (see Chapter IV). While the inclusion of comorbidities is more clinically realistic, they create additional variables to control for and can create a source of variation that makes it difficult to evaluate the efficacy of a therapy. Standardizing the injury model to avoid damage to native nerve and vasculature will help better evaluate therapeutic outcomes by reducing variability within experimental groups. Thus, future implantation studies should move away from full-thickness injury models and explore the effects of injury size, location, and geometry without the confounding denervation and ischemia injuries.

Additionally, in future SMU implantation studies, we also hope to more thoroughly evaluate the animals' immune and inflammatory responses throughout the recovery period. In both of the implantation studies (Chapters III and IV), no signs of tissue rejection were observed and there were no signs of a chronic adaptive immune response at the time of explant. This was surprising, as SMUs were allografts and were not devitalized prior to implantation. However, although white blood cell counts were within normal limits at the time of explant and the animal's

health was monitored throughout the recovery period, we did not specifically monitor immune response prior to the time of explant, so an acute inflammatory response at earlier timepoints could have gone unnoticed (i.e. before 3-months in the hindlimb study and before 2-months in the facial muscle study). In future studies, we will monitor immune and inflammatory responses throughout the recovery period to better understand the host's response to the implanted tissue. Furthermore, future work should explore the effects of an autograft versus an allograft in treating VML in a sheep model to see if improved regeneration or differences in immune or inflammatory response is observed.

Clinical Future Directions

Although adaptive immune responses were not observed in our implantation studies, it is unclear if an allograft could be used in human patients without producing an immune response. Typically, the possibility of immune rejection of allogenic tissues necessitates modulation of the patient's immune system. This includes the use of immunosuppressive drugs or the inclusion of immunomodulatory components in the engineered tissue [246]. For example, some groups have incorporated immunomodulatory growth factors or cytokines into their biomaterials [247, 248] or used ECM scaffolds to promote the switching of innate immune cells to an anti-inflammatory phenotype [249, 250], but it is unclear if these methods would be sufficient to prevent an immune response in human patients. In contrast, autogenic therapies avoid the issue of immune rejection entirely; however, the choice between an autogenic or allogenic cell source has considerable implications for commercialization.

In general, the choice between an autogenic or allogenic engineered tissue also has implications for both FDA regulations and manufacturing. From a regulatory standpoint, autogenic tissues typically have greater difficulty meeting quality and efficacy standards than allogenic

tissues [251]. This is partly because regulations related to quality assurance of autografts cannot be fully standardized due to the nature of autogenic products which are inherently affected by many sources of variability, including donor variability [252, 253]. Conversely, allogenic technologies allow for “off-the-shelf” products and thus have improved quality assurance but are subject to increased regulations because of safety concerns associated with immune rejection [251]. Additionally, there remains a lack of clear standards for regulatory approval of personalized medicine products despite attempts by the FDA to enact regulatory reform [254, 255].

The quality standards set by the FDA apply to not only the final commercial product but also the manufacturing process. Specifically, the FDA requires companies to follow good manufacturing practices (GMP) which is a system that ensures quality standards are maintained throughout all aspects of the manufacturing process. This includes cell sourcing and expansion, as well as large scale tissue fabrication, shelf-life, and storage. Thus, these aspects should be considered even at preclinical stages of technology development. Costs associated with manufacturing also differentially affect autogenic and allogenic products. In general, autogenic tissues are typically more difficult and costly to manufacture, whereas allogenic technologies have comparatively lower production costs [251]. Thus, regulatory and manufacturing issues necessitate careful consideration of both the technical and commercial advantages and disadvantages associated with autogenic versus allogenic engineered tissues.

Barriers to commercialization present a major hurdle for tissue engineered technologies in general, even to those that show great preclinical potential. The majority of medical product commercialization efforts ultimately fail, and this high failure rate is at least partially attributable to the high costs associated with running clinical trials and with meeting FDA quality and safety standards. To put these costs into perspective, access to capital has been consistently identified by

both academic institutions and companies as a significant hurdle to commercialization [123]. On average, a pharmaceutical company spends over $850 million to bring a new product to market [124], and this cost is further inflated by high failure rates of clinical trials which creates a significant economic burden [256]. Specifically, 86% of all clinical trials fail to result in FDA approval [256]. Thus, barriers to commercialization should be addressed even in preclinical development of the technology to maximize the probability of success.

Summary

In sum, my thesis work contributed to the field of tissue engineering by introducing a fabrication method that yielded the largest engineered skeletal muscle tissues to date. Our technology not only addresses the limitations of current treatment options, but also demonstrates great potential for treating clinical VML in the future. The studies described herein highlight the importance of cell source in the fabrication of engineered skeletal muscle tissues, the differences in regenerative capacities between craniofacial and limb muscle, and the effect of the VML injury model, including size, location, and geometry. Notably, this work also contributed a new large animal model of VML and first craniofacial VML model, and in doing so, our lab became only the third research group to perform a large animal VML study. Future work will involve further development of the technology by influencing myotube alignment to promote a more native-like skeletal muscle phenotype and will compare the regenerative potential and immunological effects of autogenic and allogenic SMUs. In moving towards the clinic, commercial and regulatory aspects of development should be considered to increase the probability of successful commercialization.

Appendix

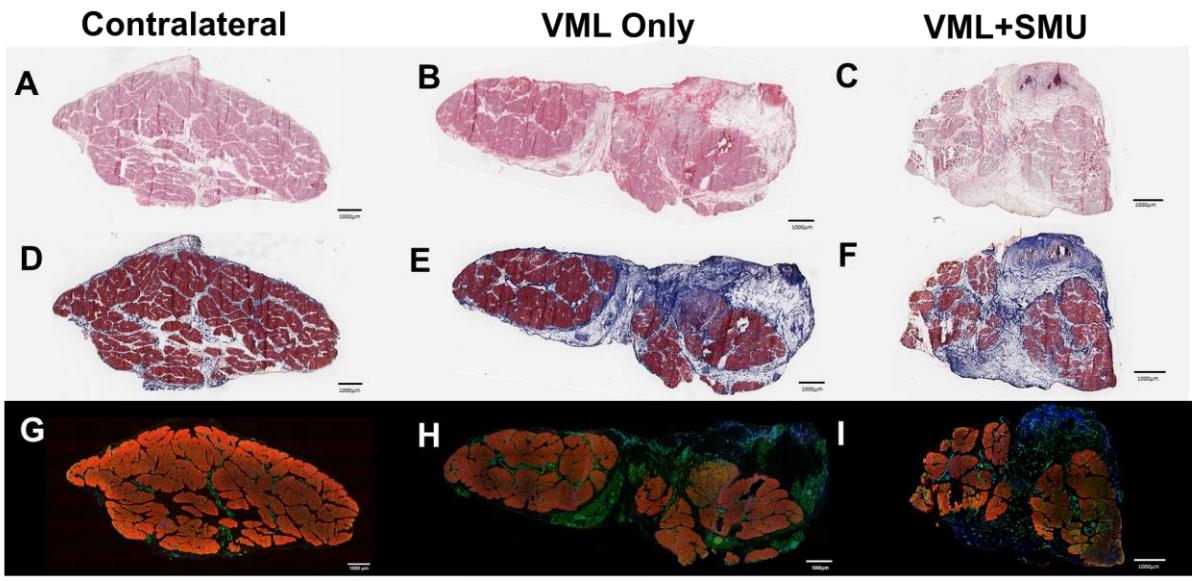

Figure 31. Histology at the 2-Month Recovery Timepoint.

Cross sections of muscles from contralateral (A,D,G), VML only (B,E,H), and VML+SMU (C,F,I) groups were taken from the midbelly of the muscle. Tissues stained with H&E (A-C) and Masson's trichrome (D-F) indicates that there are large fibrotic regions in the injury site. Immunostaining for myosin heavy chain (MF20, red) and laminin (green) (G-I) show that muscle is absent in a large portion of the surgical site.

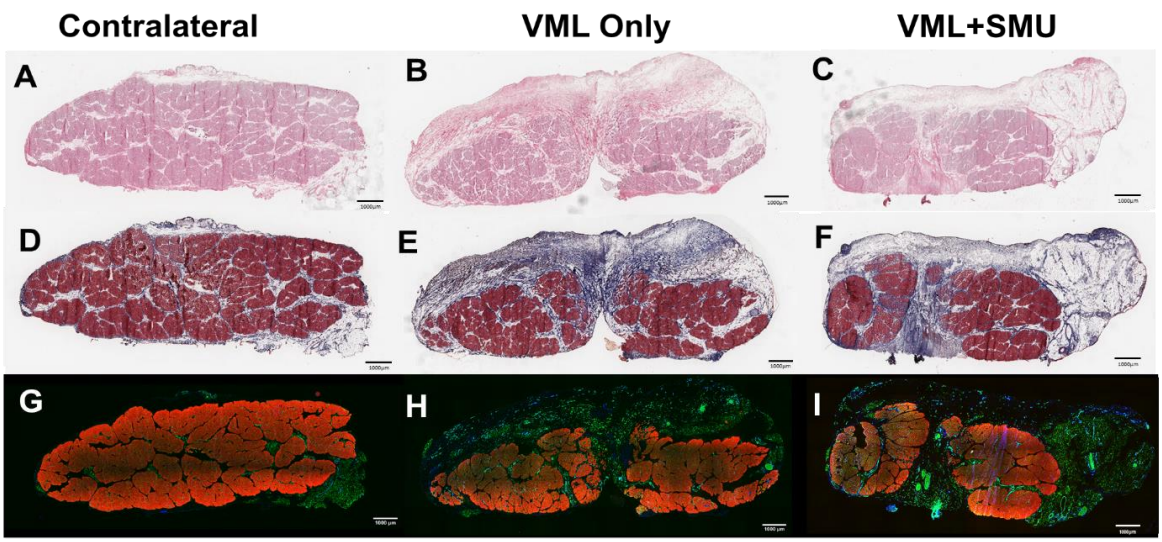

Figure 32. Histology at the 4-Month Recovery Timepoint.

Cross sections of muscles from contralateral (A,D,G), VML only (B,E,H), and VML+SMU (C,F,I) groups were taken from the midbelly of the muscle. Tissues stained with H&E (A-C) and Masson's trichrome (D-F) indicates that there are large fibrotic regions in the injury site. Immunostaining for myosin heavy chain (MF20, red) and laminin (green) (G-I) show that muscle is absent in a large portion of the surgical site.

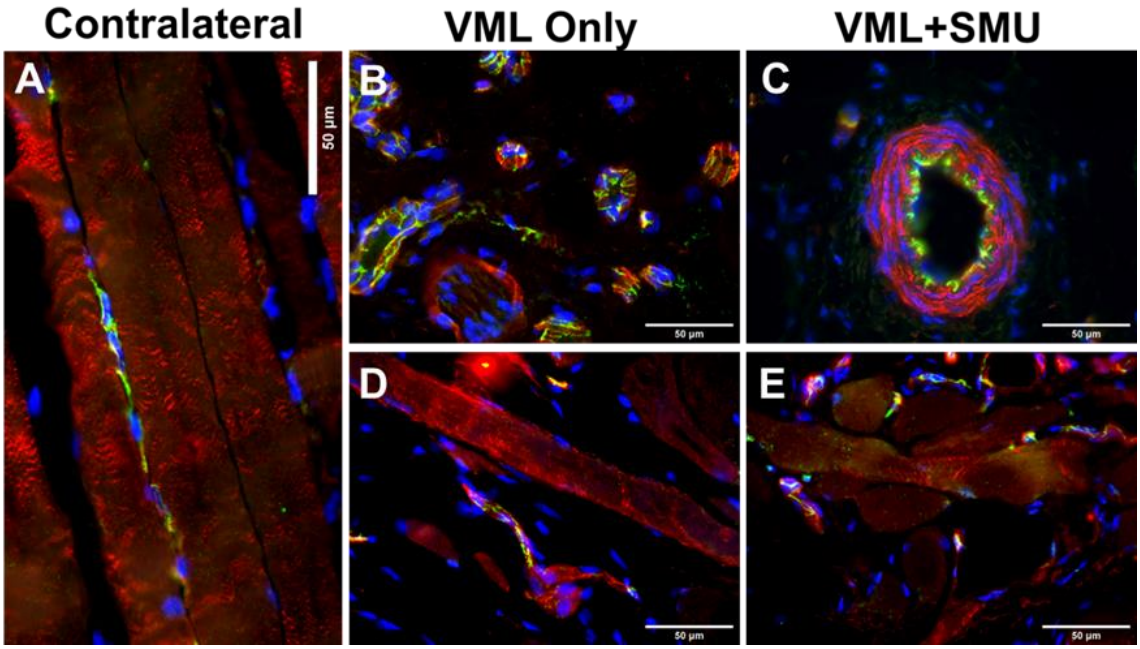

Figure 33. Vasculature and Sarcomeric Organization at the 6-Month Recovery Timepoint.

Immunostaining for α-actinin (red), CD31 (green), and DAPI (blue), reveals the presence of z-discs, endothelial cells, and nuclei, respectively. The presence of vasculature (green) is noted in (A) the ininjured contralateral muscle and in the the repair site of the (B) VML Only and (C) VML+SMU groups. Sarcomeric organization (red) is present in the muscle fibers of (A) the uninjured contralateral, as well as in the small muscle fibers in the repair site of the (D) VML Only and (E) VML+SMU groups.

Bibliography

1. Rodriguez, B.L. and L.M. Larkin, Functional three-dimensional scaffolds for skeletal **muscle** tissue engineering, in Functional 3D Tissue Engineering Scaffolds, Y. Deng and J. Kuiper, Editors. 2017, Elsevier. p. 279-304.

2. Grasman, J.M., et al., Biomimetic scaffolds for regeneration of volumetric muscle loss in skeletal muscle injuries. Acta Biomater, 2015. **25**: p. 2-15.

3. Listrat, A., et al., How Muscle Structure and Composition Influence Meat and Flesh Quality. ScientificWorldJournal, 2016. **2016**: p. 3182746.

4. Romero, N.B. and M. Bitoun, Centronuclear myopathies. Semin Pediatr Neurol, 2011. **18**(4): p. 250-6.

5. Folker, E.S. and M.K. Baylies, Nuclear positioning in muscle development and disease. Front Physiol, 2013. **4**: p. 363.

6. Josephson, R.K., Extensive and intensive factors determining the performance of striated muscle. J Exp Zool, 1975. **194**(1): p. 135-53.

7. Sacks, R.D. and R.R. Roy, Architecture of the hind limb muscles of cats: functional significance. J Morphol, 1982. **173**(2): p. 185-95.

8. Close, R.I., Dynamic properties of mammalian skeletal muscles. Physiol Rev, 1972. **52**(1): p. 129-97.

9. Powell, P.L., et al., Predictability of skeletal muscle tension from architectural determinations in guinea pig hindlimbs. J Appl Physiol Respir Environ Exerc Physiol, 1984. **57**(6): p. 1715-21.

10. Geiger, P.C., et al., Effect of unilateral denervation on maximum specific force in rat diaphragm muscle fibers. J Appl Physiol (1985), 2001. **90**(4): p. 1196-204.

11. van der Meulen, J.H., et al., Denervated muscle fibers explain the deficit in specific force following reinnervation of the rat extensor digitorum longus muscle. Plast Reconstr Surg, 2003. **112**(5): p. 1336-46.

12. Roberts, B.M., et al., Cancer cachexia decreases specific force and accelerates fatigue in limb muscle. Biochem Biophys Res Commun, 2013. **435**(3): p. 488-92.

13. Gumucio, J.P., et al., Rotator cuff tear reduces muscle fiber specific force production and induces macrophage accumulation and autophagy. J Orthop Res, 2012. **30**(12): p. 1963-70.

14. Zhong, S., D.A. Lowe, and L.V. Thompson, Effects of hindlimb unweighting and aging on rat semimembranosus muscle and myosin. J Appl Physiol (1985), 2006. **101**(3): p. 873-80.

15. Thompson, L.V., S.A. Johnson, and J.A. Shoeman, Single soleus muscle fiber function after hindlimb unweighting in adult and aged rats. J Appl Physiol (1985), 1998. **84**(6): p. 1937-42.

16. Fukunaga, T., et al., Specific tension of human plantar flexors and dorsiflexors. J Appl Physiol (1985), 1996. **80**(1): p. 158-65.

17. Buchanan, T.S., Evidence that maximum muscle stress is not a constant: differences in specific tension in elbow flexors and extensors. Med Eng Phys, 1995. **17**(7): p. 529-36.

18. Maganaris, C.N., et al., In vivo specific tension of human skeletal muscle. J Appl Physiol (1985), 2001. **90**(3): p. 865-72.

19. Faulkner, J.A., et al., Contractile properties of transplanted extensor digitorum longus muscles of cats. Am J Physiol, 1980. **238**(3): p. C120-6.

20. Murphy, R.A. and A.C. Beardsley, Mechanical properties of the cat soleus muscle in situ. Am J Physiol, 1974. **227**(5): p. 1008-13.

21. Spector, S.A., et al., Muscle architecture and force-velocity characteristics of cat soleus and medial gastrocnemius: implications for motor control. J Neurophysiol, 1980. **44**(5): p. 951-60.

22. Kawakami, Y., et al., Training-induced changes in muscle architecture and specific tension. Eur J Appl Physiol Occup Physiol, 1995. **72**(1-2): p. 37-43.

23. Reeves, N.D., M.V. Narici, and C.N. Maganaris, Effect of resistance training on skeletal muscle-specific force in elderly humans. J Appl Physiol (1985), 2004. **96**(3): p. 885-92.

24. Erskine, R.M., et al., Resistance training increases in vivo quadriceps femoris muscle specific tension in young men. Acta Physiol (Oxf), 2010. **199**(1): p. 83-9.

25. Erskine, R.M., et al., What causes in vivo muscle specific tension to increase following resistance training? Exp Physiol, 2011. **96**(2): p. 145-55.

26. Erskine, R.M., et al., Inter-individual variability in the adaptation of human muscle specific tension to progressive resistance training. Eur J Appl Physiol, 2010. **110**(6): p. 1117-25.

27. Morse, C.I., et al., Gastrocnemius muscle specific force in boys and men. J Appl Physiol (1985), 2008. **104**(2): p. 469-74.

28. Phillips, S.K., et al., Muscle weakness in women occurs at an earlier age than in men, but strength is preserved by hormone replacement therapy. Clin Sci (Lond), 1993. **84**(1): p. 95-8.

29. Lowe, D.A., D.D. Thomas, and L.V. Thompson, Force generation, but not myosin ATPase activity, declines with age in rat muscle fibers. Am J Physiol Cell Physiol, 2002. **283**(1): p. C187-92.

30. Wisdom, K.M., S.L. Delp, and E. Kuhl, Use it or lose it: multiscale skeletal muscle adaptation to mechanical stimuli. Biomech Model Mechanobiol, 2015. **14**(2): p. 195-215.

31. Asakura, A., M. Komaki, and M. Rudnicki, Muscle satellite cells are multipotential stem cells that exhibit myogenic, osteogenic, and adipogenic differentiation. Differentiation, 2001. **68**(4-5): p. 245-53.

32. Zouraq, F., et al., Skeletal Muscle Regeneration for Clinical Application. Regenerative Medicine and Tissue Engineering, 2013: p. 679-712.

33. Lepper, C., T.A. Partridge, and C.M. Fan, An absolute requirement for Pax7-positive satellite cells in acute injury-induced skeletal muscle regeneration. Development, 2011. **138**(17): p. 3639-46.

34. Bautch, V.L., Stem cells and the vasculature. Nat Med, 2011. **17**(11): p. 1437-43.

35. Dellavalle, A., et al., Pericytes of human skeletal muscle are myogenic precursors distinct from satellite cells. Nat Cell Biol, 2007. **9**(3): p. 255-67.

36. Crisan, M., et al., Perivascular cells for regenerative medicine. J Cell Mol Med, 2012. **16**(12): p. 2851-60.

37. Allt, G. and J.G. Lawrenson, Pericytes: cell biology and pathology. Cells Tissues Organs, 2001. **169**(1): p. 1-11.

38. Liebner, S., C.J. Czupalla, and H. Wolburg, Current concepts of blood-brain barrier development. Int J Dev Biol, 2011. **55**(4-5): p. 467-76.

39. Fakhrejahani, E. and M. Toi, Tumor angiogenesis: pericytes and maturation are not to be ignored. J Oncol, 2012. **2012**: p. 261750.

40. Birbrair, A., et al., Skeletal muscle pericyte subtypes differ in their differentiation potential. Stem Cell Res, 2013. **10**(1): p. 67-84.

41. Winkler, E.A., R.D. Bell, and B.V. Zlokovic, Central nervous system pericytes in health and disease. Nat Neurosci, 2011. **14**(11): p. 1398-1405.

42. Dellavalle, A., et al., Pericytes resident in postnatal skeletal muscle differentiate into muscle fibres and generate satellite cells. Nat Commun, 2011. **2**: p. 499.

43. Crisan, M., et al., A perivascular origin for mesenchymal stem cells in multiple human organs. Cell Stem Cell, 2008. **3**(3): p. 301-13.

44. Rodriguez, B.L., et al., A Comparison of Ovine Facial and Limb Muscle as a Primary Cell Source for Engineered Skeletal Muscle. Tissue Eng Part A, 2019.

45. Péault, B., et al., Stem and progenitor cells in skeletal muscle development, maintenance, and therapy. Mol Ther, 2007. **15**(5): p. 867-77.

46. Charg é , S.B.P. and M.A. Rudnicki, Cellular and Molecular Regulation of Muscle Regeneration. Physiological Reviews, 2004. **84**(1): p. 209-238.

47. Tedesco, F.S., et al., Repairing skeletal muscle: regenerative potential of skeletal muscle stem cells. J Clin Invest, 2010. **120**(1): p. 11-9.

48. Chargé , S.B.P. and M.A. Rudnicki, Cellular and Molecular Regulation of Muscle Regeneration. Physiological Reviews, 2004. **84**(1): p. 209-238.

49. Cossu, G., Unorthodox myogenesis: possible developmental significance and implications for tissue histogenesis and regeneration. Histol Histopathol, 1997. **12**(3): p. 755-60.

50. Ferrari, G., et al., Muscle regeneration by bone marrow-derived myogenic progenitors. Science, 1998. **279**(5356): p. 1528-30.

51. Gussoni, E., et al., Dystrophin expression in the mdx mouse restored by stem cell transplantation. Nature, 1999. **401**(6751): p. 390-4.

52. Zuk, P.A., et al., Human adipose tissue is a source of multipotent stem cells. Mol Biol Cell, 2002. **13**(12): p. 4279-95.

53. Zuk, P., Adipose-Derived Stem Cells in Tissue Regeneration: A Review. 2013. **2013**.

54. Fiore, D., et al., Pharmacological blockage of fibro/adipogenic progenitor expansion and suppression of regenerative fibrogenesis is associated with impaired skeletal muscle regeneration. Stem Cell Res, 2016. **17**(1): p. 161-9.

55. Biferali, B., et al., Fibro-Adipogenic Progenitors Cross-Talk in Skeletal Muscle: The Social Network. Front Physiol, 2019. **10**: p. 1074.

56. Joe, A.W., et al., Muscle injury activates resident fibro/adipogenic progenitors that facilitate myogenesis. Nat Cell Biol, 2010. **12**(2): p. 153-63.

57. Wosczyna, M.N., et al., Mesenchymal Stromal Cells Are Required for Regeneration and Homeostatic Maintenance of Skeletal Muscle. Cell Rep, 2019. **27**(7): p. 2029-2035.e5.

58. Heredia, J.E., et al., Type 2 innate signals stimulate fibro/adipogenic progenitors to facilitate muscle regeneration. Cell, 2013. **153**(2): p. 376-88.

59. Uezumi, A., et al., Fibrosis and adipogenesis originate from a common mesenchymal progenitor in skeletal muscle. J Cell Sci, 2011. **124**(Pt 21): p. 3654-64.

60. Lounev, V.Y., et al., Identification of progenitor cells that contribute to heterotopic skeletogenesis. J Bone Joint Surg Am, 2009. **91**(3): p. 652-63.

61. Judson, R.N., et al., Isolation, Culture, and Differentiation of Fibro/Adipogenic Progenitors (FAPs) from Skeletal Muscle. Methods Mol Biol, 2017. **1668**: p. 93-103.

62. Darby, I.A., et al., Fibroblasts and myofibroblasts in wound healing. Clin Cosmet Investig Dermatol, 2014. **7**: p. 301-11.

63. Watsky, M.A., et al., Chapter Four - New Insights into the Mechanism of Fibroblast to Myofibroblast Transformation and Associated Pathologies, in International Review of Cell and Molecular Biology. 2010, Academic Press. p. 165-192.

64. Lowe, J.S. and P.G. Anderson, Chapter 5 - Contractile Cells. 2015, Mosby: Philadelphia. p. 71-83.

65. Kwan, P., A. Desmoulière, and E.E. Tredget, Molecular and cellular basis of hypertrophic scarring. 2012: p. 495-505.e5.

66. Petreaca, M., et al., Chapter 2 - Cell-ECM Interactions in Repair and Regeneration. 2011, Academic Press: San Diego. p. 19-65.

67. Yelin, E., S. Weinstein, and T. King, The burden of musculoskeletal diseases in the United States. Semin Arthritis Rheum, 2016. **46**(3): p. 259-260.

68. Woolf, A.D. and B. Pfleger, Burden of major musculoskeletal conditions. Bull World Health Organ, 2003. **81**(9): p. 646-56.

69. Briggs, A.M., et al., Reducing the global burden of musculoskeletal conditions. Bull World Health Organ, 2018. **96**(5): p. 366-368.

70. Corona, B.T., et al., Volumetric muscle loss leads to permanent disability following extremity trauma. J Rehabil Res Dev, 2015. **52**(7): p. 785-92.

71. Corona, B.T., J.C. Wenke, and C.L. Ward, Pathophysiology of Volumetric Muscle Loss Injury. Cells Tissues Organs, 2016. **202**(3-4): p. 180-188.

72. Grogan, B.F., J.R. Hsu, and S.T.R. Consortium, Volumetric muscle loss. J Am Acad Orthop Surg, 2011. **19 Suppl 1**: p. S35-7.

73. MacKenzie, E.J., et al., Characterization of patients with high-energy lower extremity trauma. J Orthop Trauma, 2000. **14**(7): p. 455-66.

74. van den Elzen, M.E., et al., Adults with congenital or acquired facial disfigurement: impact of appearance on social functioning. J Craniomaxillofac Surg, 2012. **40**(8): p. 777-82.

75. Caldwell, C.J., D.L. Mattey, and R.O. Weller, Role of the basement membrane in the regeneration of skeletal muscle. Neuropathol Appl Neurobiol, 1990. **16**(3): p. 225-38.

76. Lefaucheur, J.P. and A. Sébille, The cellular events of injured muscle regeneration depend on the nature of the injury. Neuromuscul Disord, 1995. **5**(6): p. 501-9.

77. Thomas, K., A.J. Engler, and G.A. Meyer, Extracellular matrix regulation in the muscle satellite cell niche. Connect Tissue Res, 2015. **56**(1): p. 1-8.

78. Dodson, M.V., et al., Skeletal muscle stem cells from animals I. Basic cell biology. Int J Biol Sci, 2010. **6**(5): p. 465-74.

79. Aguilar, C.A., et al., Multiscale analysis of a regenerative therapy for treatment of volumetric muscle loss injury. Cell Death Discov, 2018. **4**: p. 33.

80. Greising, S.M., et al., Unwavering Pathobiology of Volumetric Muscle Loss Injury. Sci Rep, 2017. **7**(1): p. 13179.

81. Garg, K., et al., Volumetric muscle loss: persistent functional deficits beyond frank loss of tissue. J Orthop Res, 2015. **33**(1): p. 40-6.

82. Rivera, J.C. and B.T. Corona, Muscle-related Disability Following Combat Injury Increases With Time. US Army Med Dep J, 2016: p. 30-4.

83. Carlson, B.M., The Biology of Long-Term Denervated Skeletal Muscle. Eur J Transl Myol, 2014. **24**(1): p. 3293.

84. Chu, J., F. Bruyninckx, and D.V. Neuhauser, Chronic refractory myofascial pain and denervation supersensitivity as global public health disease. BMJ Case Rep, 2016. **2016**.

85. Gunn, C.C., 'Prespondylosis' and some pain syndromes following denervation supersensitivity. Spine, 1980. **5**(2): p. 185-192.

86. Mertens, J.P., et al., Engineering muscle constructs for the creation of functional engineered musculoskeletal tissue. Regen Med, 2014. **9**(1): p. 89-100.

87. Mao, J.J., et al., Facial reconstruction by biosurgery: cell transplantation versus cell homing. Tissue Eng Part B Rev, 2010. **16**(2): p. 257-62.

88. Aurora, A., et al., Physical rehabilitation improves muscle function following volumetric muscle loss injury. BMC Sports Sci Med Rehabil, 2014. **6**(1): p. 41.

89. Bianchi, B., et al., Free flaps: outcomes and complications in head and neck reconstructions. J Craniomaxillofac Surg, 2009. **37**(8): p. 438-42.

90. Huh, J., et al., Infectious complications and soft tissue injury contribute to late amputation after severe lower extremity trauma. J Trauma, 2011. **71**(1 Suppl): p. S47-51.

91. Corona, B.T., et al., The promotion of a functional fibrosis in skeletal muscle with volumetric muscle loss injury following the transplantation of muscle-ECM. Biomaterials, 2013. **34**(13): p. 3324-35.

92. Dziki, J., et al., An acellular biologic scaffold treatment for volumetric muscle loss: results of a 13-patient cohort study. NPJ Regen Med, 2016. **1**: p. 16008.

93. Gentile, N.E., et al., Targeted rehabilitation after extracellular matrix scaffold transplantation for the treatment of volumetric muscle loss. Am J Phys Med Rehabil, 2014. **93**(11 Suppl 3): p. S79-87.

94. Sicari, B.M., J.L. Dziki, and S.F. Badylak, Strategies for functional bioscaffold-based skeletal muscle reconstruction. Ann Transl Med, 2015. **3**(17): p. 256.

95. Valentin, J.E., et al., Functional skeletal muscle formation with a biologic scaffold. Biomaterials, 2010. **31**(29): p. 7475-84.

96. Garland, C. and J. Pomerantz, Regenerative Strategies for Craniofacial Disorders. Frontiers in Physiology, 2012. **3**(453).

97. Rose, L.F., et al., The convergence of regenerative medicine and rehabilitation: federal perspectives. NPJ Regen Med, 2018. **3**: p. 19.

98. Greising, S.M., et al., Therapeutic Approaches for Volumetric Muscle Loss Injury: A Systematic Review and Meta-Analysis. Tissue Eng Part B Rev, 2019. **25**(6): p. 510-525.

99. Borselli, C., et al., Functional muscle regeneration with combined delivery of angiogenesis and myogenesis factors. Proc Natl Acad Sci U S A, 2010. **107**(8): p. 3287-92.

100. Shvartsman, D., et al., Sustained delivery of VEGF maintains innervation and promotes reperfusion in ischemic skeletal muscles via NGF/GDNF signaling. Mol Ther, 2014. **22**(7): p. 1243-53.

101. Hammers, D.W., et al., Controlled release of IGF-I from a biodegradable matrix improves functional recovery of skeletal muscle from ischemia/reperfusion. Biotechnol Bioeng, 2012. **109**(4): p. 1051-9.

102. Wang, L., et al., Minimally invasive approach to the repair of injured skeletal muscle with a shape-memory scaffold. Mol Ther, 2014. **22**(8): p. 1441-9.

103. Stratos, I., et al., Open blunt crush injury of different severity determines nature and extent of local tissue regeneration and repair. J Orthop Res, 2010. **28**(7): p. 950-7.

104. Lewis, M.P., et al., The extracellular matrix of muscle--implications for manipulation of the craniofacial musculature. Eur J Oral Sci, 2001. **109**(4): p. 209-21.

105. Broughton, M. and G.M. Fyfe, The superficial musculoaponeurotic system of the face: a model explored. Anat Res Int, 2013. **2013**: p. 794682.

106. Hwang, K. and J.H. Choi, Superficial Fascia in the Cheek and the Superficial Musculoaponeurotic System. J Craniofac Surg, 2018. **29**(5): p. 1378-1382.

107. Pavlath, G.K., et al., Heterogeneity among muscle precursor cells in adult skeletal muscles with differing regenerative capacities. Dev Dyn, 1998. **212**(4): p. 495-508.

108. Kim, J., et al., Muscle tissue engineering for partial glossectomy defects. Arch Facial Plast Surg, 2003. **5**(5): p. 403-7.

109. Noden, D.M. and P. Francis-West, The differentiation and morphogenesis of craniofacial muscles. Dev Dyn, 2006. **235**(5): p. 1194-218.

110. Vega-Soto, E., et al., A 30% Volumetric Muscle Loss Does Not Result in Sustained Functional Deficits After a 90-Day Recovery in Rats. Regenerative Engineering and Translational Medicine, 2019.

111. US Food and Drug Administration. Guidance for Industry: Preclinical Assessment of Investigational Cellular and Gene Therapy Products. 2014 09/15/2014 Available from: http://www.fda.gov/BiologicsBloodVaccines/GuidanceComplianceRegulatoryInformation/Guidances/CellularandGeneTherapy/ucm376136.htm.

112. Corona, B.T., et al., Pharmacological Mitigation of Fibrosis in a Porcine Model of Volumetric Muscle Loss Injury. Tissue Eng Part A, 2019.

113. Ward, C.L., et al., Autologous Minced Muscle Grafts Improve Muscle Strength in a Porcine Model of Volumetric Muscle Loss Injury. J Orthop Trauma, 2016. **30**(12): p. e396-e403.

114. Turner, N.J., et al., Biologic scaffold remodeling in a dog model of complex musculoskeletal injury. J Surg Res, 2012. **176**(2): p. 490-502.

115. National Institutes of Health. Tissue Engineering and Regenerative Medicine. [cited 2017 January 26]; Available from: https://www.nibib.nih.gov/science-education/science-topics/tissue-engineering-and-regenerative-medicine.

116. Sicari, B.M., C.L. Dearth, and S.F. Badylak, Tissue engineering and regenerative medicine approaches to enhance the functional response to skeletal muscle injury. Anat Rec (Hoboken), 2014. **297**(1): p. 51-64.

117. Thorrez, L., et al., Growth, differentiation, transplantation and survival of human skeletal myofibers on biodegradable scaffolds. Biomaterials, 2008. **29**(1): p. 75-84.

118. Hill, E., T. Boontheekul, and D.J. Mooney, Designing scaffolds to enhance transplanted myoblast survival and migration. Tissue Eng, 2006. **12**(5): p. 1295-304.

119. Beauchamp, J.R., et al., Dynamics of myoblast transplantation reveal a discrete minority of precursors with stem cell-like properties as the myogenic source. J Cell Biol, 1999. **144**(6): p. 1113-22.

120. Qu, Z., et al., Development of approaches to improve cell survival in myoblast transfer therapy. J Cell Biol, 1998. **142**(5): p. 1257-67.

121. Skuk, D., et al., Successful myoblast transplantation in primates depends on appropriate cell delivery and induction of regeneration in the host muscle. Exp Neurol, 1999. **155**(1): p. 22-30.

122. McKeon-Fischer, K.D., et al., In vivo skeletal muscle biocompatibility of composite, coaxial electrospun, and microfibrous scaffolds. Tissue Eng Part A, 2014. **20**(13-14): p. 1961-70.

123. Bertram, T.A., et al., Hurdles in tissue engineering/regenerative medicine product commercialization: a pilot survey of governmental funding agencies and the financial industry. Tissue Eng Part A, 2012. **18**(21-22): p. 2187-94.

124. Paul, S.M., et al., How to improve R&D productivity: the pharmaceutical industry's grand challenge. Nat Rev Drug Discov, 2010. **9**(3): p. 203-14.

125. Webber, M.J., et al., A perspective on the clinical translation of scaffolds for tissue engineering. Ann Biomed Eng, 2015. **43**(3): p. 641-56.

126. Williams, M.L., et al., Effect of implantation on engineered skeletal muscle constructs. J Tissue Eng Regen Med, 2013. **7**(6): p. 434-42.

127. VanDusen, K.W., et al., Engineered skeletal muscle units for repair of volumetric muscle loss in the tibialis anterior muscle of a rat. Tissue Eng Part A, 2014. **20**(21-22): p. 2920-30.

128. Syverud, B.C., K.W. VanDusen, and L.M. Larkin, Effects of Dexamethasone on Satellite Cells and Tissue Engineered Skeletal Muscle Units. Tissue Eng Part A, 2016. **22**(5-6): p. 480-9.

129. Takahashi, H., et al., The use of anisotropic cell sheets to control orientation during the self-organization of 3D muscle tissue. Biomaterials, 2013. **34**(30): p. 7372-80.

130. Takahashi, H. and T. Okano, Cell Sheet-Based Tissue Engineering for Organizing Anisotropic Tissue Constructs Produced Using Microfabricated Thermoresponsive Substrates. Adv Healthc Mater, 2015. **4**(16): p. 2388-407.

131. Kim, S.J., et al., Multifunctional cell-culture platform for aligned cell sheet monitoring, transfer printing, and therapy. ACS Nano, 2015. **9**(3): p. 2677-88.

132. Chen, S., et al., Engineering multi-layered skeletal muscle tissue by using 3D microgrooved collagen scaffolds. Biomaterials, 2015. **73**: p. 23-31.

133. Huang, Y.C., et al., Rapid formation of functional muscle in vitro using fibrin gels. J Appl Physiol (1985), 2005. **98**(2): p. 706-13.

134. Dennis, R.G. and P.E. Kosnik, Excitability and isometric contractile properties of mammalian skeletal muscle constructs engineered in vitro. In Vitro Cell Dev Biol Anim, 2000. **36**(5): p. 327-35.

135. Dennis, R.G., et al., Excitability and contractility of skeletal muscle engineered from primary cultures and cell lines. Am J Physiol Cell Physiol, 2001. **280**(2): p. C288-95.

136. Yan, W., et al., Tissue engineering of skeletal muscle. Tissue Eng, 2007. **13**(11): p. 2781-90.

137. Larkin, L.M., et al., Functional evaluation of nerve-skeletal muscle constructs engineered in vitro. In Vitro Cell Dev Biol Anim, 2006. **42**(3-4): p. 75-82.

138. Larkin, L.M., et al., Structure and functional evaluation of tendon-skeletal muscle constructs engineered in vitro. Tissue Eng, 2006. **12**(11): p. 3149-58.

139. Ma, J., et al., Three-dimensional engineered bone-ligament-bone constructs for anterior cruciate ligament replacement. Tissue Eng Part A, 2012. **18**(1-2): p. 103-16.

140. Rodriguez, B.L., et al., The Maturation of Tissue-Engineered Skeletal Muscle Units Following 28-Day Ectopic Implantation in a Rat. Regenerative Engineering and Translational Medicine, 2018.

141. Service, R.F., Tissue engineering. Technique uses body as 'bioreactor' to grow new bone. Science, 2005. **309**(5735): p. 683.

142. Jana, T., et al., The body as a living bioreactor: a feasibility study of pedicle flaps for tracheal transplantation. Eur Arch Otorhinolaryngol, 2013. **270**(1): p. 181-6.

143. Naujokat, H., et al., Man as a living bioreactor: Long-term histological aspects of a mandibular replacement engineered in the patient's own body. Int J Oral Maxillofac Surg, 2018. **47**(11): p. 1481-1487.

144. Yap, K.K., et al., The Vascularised Chamber as an In Vivo Bioreactor. Trends Biotechnol, 2018. **36**(10): p. 1011-1024.

145. Rodriguez, B.L., et al., The Maturation of Tissue-Engineered Skeletal Muscle Units following 28-Day Ectopic Implantation in a Rat. Regen Eng Transl Med, 2018. **5**(1): p. 86-94.

146. Koning, M., et al., Current opportunities and challenges in skeletal muscle tissue engineering. J Tissue Eng Regen Med, 2009. **3**(6): p. 407-15.

147. Ikada, Y., Challenges in tissue engineering. J R Soc Interface, 2006. **3**(10): p. 589-601.

148. Grounds, M.D., Obstacles and challenges for tissue engineering and regenerative medicine: Australian nuances. Clin Exp Pharmacol Physiol, 2018. **45**(4): p. 390-400.

149. Hentze, H., et al., Teratoma formation by human embryonic stem cells: evaluation of essential parameters for future safety studies. Stem Cell Res, 2009. **2**(3): p. 198-210.

150. Herberts, C.A., M.S. Kwa, and H.P. Hermsen, Risk factors in the development of stem cell therapy. J Transl Med, 2011. **9**: p. 29.

151. Anderson, J.M., A. Rodriguez, and D.T. Chang, Foreign body reaction to biomaterials. Semin Immunol, 2008. **20**(2): p. 86-100.

152. Jain, R.K., et al., Engineering vascularized tissue. Nat Biotechnol, 2005. **23**(7): p. 821-3.

153. Silva, M.M., et al., The effect of anisotropic architecture on cell and tissue infiltration into tissue engineering scaffolds. Biomaterials, 2006. **27**(35): p. 5909-17.

154. Rouwkema, J., et al., Supply of nutrients to cells in engineered tissues. Biotechnol Genet Eng Rev, 2010. **26**: p. 163-78.

155. Folkman, J. and M. Hochberg, Self-regulation of growth in three dimensions. J Exp Med, 1973. **138**(4): p. 745-53.

156. Laschke, M.W. and M.D. Menger, Prevascularization in tissue engineering: Current concepts and future directions. Biotechnol Adv, 2016. **34**(2): p. 112-21.

157. Fuoco, C., et al., Matrix scaffolding for stem cell guidance toward skeletal muscle tissue engineering. J Orthop Surg Res, 2016. **11**(1): p. 86.

158. Rustad, K.C., et al., Strategies for organ level tissue engineering. Organogenesis, 2010. **6**(3): p. 151-7.

159. Levenberg, S., et al., Engineering vascularized skeletal muscle tissue. Nat Biotechnol, 2005. **23**(7): p. 879-84.

160. Auger, F.A., L. Gibot, and D. Lacroix, The pivotal role of vascularization in tissue engineering. Annu Rev Biomed Eng, 2013. **15**: p. 177-200.

161. Kant, R.J. and K.L.K. Coulombe, Integrated approaches to spatiotemporally directing angiogenesis in host and engineered tissues. Acta Biomater, 2018. **69**: p. 42-62.

162. Watson, E.C., Z.L. Grant, and L. Coultas, Endothelial cell apoptosis in angiogenesis and vessel regression. Cell Mol Life Sci, 2017. **74**(24): p. 4387-4403.

163. Nichol, J.W. and A. Khademhosseini, Modular Tissue Engineering: Engineering Biological Tissues from the Bottom Up. Soft Matter, 2009. **5**(7): p. 1312-1319.

164. Khan, O.F., et al., A novel high-speed production process to create modular components for the bottom-up assembly of large-scale tissue-engineered constructs. Adv Healthc Mater, 2015. **4**(1): p. 113-20.

165. Sladkova, M., et al., Segmental Additive Tissue Engineering. Sci Rep, 2018. **8**(1): p. 10895.

166. Syverud, B.C., et al., A Transgenic tdTomato Rat for Cell Migration and Tissue Engineering Applications. Tissue Eng Part C Methods, 2018. **24**(5): p. 263-271.

167. Novakova, S.S., et al., Tissue-engineered tendon constructs for rotator cuff repair in sheep. J Orthop Res, 2018. **36**(1): p. 289-299.

168. Mahalingam, V.D., et al., Allogeneic versus autologous derived cell sources for use in engineered bone-ligament-bone grafts in sheep anterior cruciate ligament repair. Tissue Eng Part A, 2015. **21**(5-6): p. 1047-54.

169. Mahalingam, V.D., et al., Fresh versus frozen engineered bone-ligament-bone grafts for sheep anterior cruciate ligament repair. Tissue Eng Part C Methods, 2015. **21**(6): p. 548-56.

170. Novakova, S.S. and Rodriguez, B. L., et al., Repairing Volumetric Muscle Loss in the Ovine Peroneus Tertius Following a 3-Month Recovery. Tissue Eng Part A, 2020.

171. American Society of Plastic Surgeons, 2018 National Plastic Surgery Statistics. 2018.

172. Lew, T.A., et al., Characterization of craniomaxillofacial battle injuries sustained by United States service members in the current conflicts of Iraq and Afghanistan. J Oral Maxillofac Surg, 2010. **68**(1): p. 3-7.

173. Gassner, R., et al., Cranio-maxillofacial trauma: a 10 year review of 9,543 cases with 21,067 injuries. J Craniomaxillofac Surg, 2003. **31**(1): p. 51-61.

174. Carlson, B.M. and J.A. Faulkner, The regeneration of skeletal muscle fibers following injury: a review. Med Sci Sports Exerc, 1983. **15**(3): p. 187-98.

175. Carlson, B.M., Regeneration of the completely excised gastrocnemius muscle in the frog and rat from minced muscle fragments. J Morphol, 1968. **125**(4): p. 447-72.

176. Mase, V.J., et al., Clinical application of an acellular biologic scaffold for surgical repair of a large, traumatic quadriceps femoris muscle defect. Orthopedics, 2010. **33**(7): p. 511.

177. Leckenby, J. and A. Grobbelaar, Smile restoration for permanent facial paralysis. Arch Plast Surg, 2013. **40**(5): p. 633-8.

178. Harel, I., et al., Distinct origins and genetic programs of head muscle satellite cells. Dev Cell, 2009. **16**(6): p. 822-32.

179. Ono, Y., et al., Muscle satellite cells are a functionally heterogeneous population in both somite-derived and branchiomeric muscles. Dev Biol, 2010. **337**(1): p. 29-41.

180. Michailovici, I., T. Eigler, and E. Tzahor, Craniofacial Muscle Development. Curr Top Dev Biol, 2015. **115**: p. 3-30.

181. Collins, C.A., et al., Stem cell function, self-renewal, and behavioral heterogeneity of cells from the adult muscle satellite cell niche. Cell, 2005. **122**(2): p. 289-301.

182. Gollnick, P.D., et al., Human soleus muscle: a comparison of fiber composition and enzyme activities with other leg muscles. Pflugers Arch, 1974. **348**(3): p. 247-55.

183. Dodson, M.V., B.A. Mathison, and B.D. Mathison, Effects of medium and substratum on ovine satellite cell attachment, proliferation and differentiation in vitro. Cell Differ Dev, 1990. **29**(1): p. 59-66.

184. Dodson, M.V., et al., Isolation of Satellite Cells from Ovine Skeletal Muscles. Journal of Tissue Culture Methods, 1986. **10**(4): p. 233 - 237.

185. Burton, N.M., et al., Methods for animal satellite cell culture under a variety of conditions. Methods Cell Sci, 2000. **22**(1): p. 51-61.

186. Garrett, W.E., J.C. Califf, and F.H. Bassett, Histochemical correlates of hamstring injuries. Am J Sports Med, 1984. **12**(2): p. 98-103.

187. Osterlund, C., L.E. Thornell, and P.O. Eriksson, Differences in fibre type composition between human masseter and biceps muscles in young and adults reveal unique masseter fibre type growth pattern. Anat Rec (Hoboken), 2011. **294**(7): p. 1158-69.

188. Stål, P., Characterization of human oro-facial and masticatory muscles with respect to fibre types, myosins and capillaries. Morphological, enzyme-histochemical, immuno-histochemical and biochemical investigations. Swed Dent J Suppl, 1994. **98**: p. 1-55.

189. Schwarting, S., et al., Enzyme histochemical and histographic data on normal human facial muscles. ORL J Otorhinolaryngol Relat Spec, 1982. **44**(1): p. 51-9.

190. Hawke, T.J. and D.J. Garry, Myogenic satellite cells: physiology to molecular biology. J Appl Physiol (1985), 2001. **91**(2): p. 534-51.

191. Committee for the Update of the Guide for the Care and Use of Laboratory Animals, Guide for the Care and use of Laboratory Animals. 2010. Washington D.C.: National Academies Press.

192. Syverud, B.C., et al., Isolation and Purification of Satellite Cells for Skeletal Muscle Tissue Engineering. J Regen Med, 2014. **3**(2).

193. Cancellara, L., et al., Age-dependent variations in the expression of myosin isoforms and myogenic factors during the involution of the proximal sesamoidean ligament of sheep. Res Vet Sci, 2019. **124**: p. 270-279.

194. Popkin, P.R.W., et al., The Sheep Project (1): determining skeletal growth, timing of epiphyseal fusion and morphometric variation in unimproved Shetland sheep of known age, sex, castration status and nutrition. Journal of Archaeological Science, 2012. **39**(6): p. 1775-1792.

195. Melotti, L., et al., The natural involution of the sheep proximal sesamoidean ligament is due to depletion of satellite cells and simultaneous proliferation of fibroblasts: Ultrastructural evidence. Res Vet Sci, 2019. **124**: p. 106-111.

196. McCormick, R. and A. Vasilaki, Age-related changes in skeletal muscle: changes to life-style as a therapy. Biogerontology, 2018. **19**(6): p. 519-536.

197. Day, K., et al., The depletion of skeletal muscle satellite cells with age is concomitant with reduced capacity of single progenitors to produce reserve progeny. Dev Biol, 2010. **340**(2): p. 330-43.

198. Chakkalakal, J.V., et al., The aged niche disrupts muscle stem cell quiescence. Nature, 2012. **490**(7420): p. 355-60.

199. Shefer, G., et al., Satellite-cell pool size does matter: defining the myogenic potency of aging skeletal muscle. Dev Biol, 2006. **294**(1): p. 50-66.

200. Verdijk, L.B., et al., Satellite cells in human skeletal muscle; from birth to old age. Age (Dordr), 2014. **36**(2): p. 545-7.

201. Garg, K., C.L. Ward, and B.T. Corona, Asynchronous inflammation and myogenic cell migration limit muscle tissue regeneration mediated by a cellular scaffolds. Inflamm Cell Signal, 2014. **1**(4).

202. Deumens, R., et al., Repairing injured peripheral nerves: Bridging the gap. Prog Neurobiol, 2010. **92**(3): p. 245-76.

203. Wood, M.D. and S.E. Mackinnon, Pathways regulating modality-specific axonal regeneration in peripheral nerve. Exp Neurol, 2015. **265**: p. 171-5.

204. Oliveira, K.M.C., et al., Time course of traumatic neuroma development. PLoS One, 2018. **13**(7): p. e0200548.

205. Foltán, R., et al., Mechanism of traumatic neuroma development. Med Hypotheses, 2008. **71**(4): p. 572-6.

206. Larson, A.A., et al., Effects of Dexamethasone Dose and Timing on Tissue-Engineered Skeletal Muscle Units. Cells Tissues Organs, 2018. **205**(4): p. 197-207.

207. Syverud, B.C., et al., Label-Free, High-Throughput Purification of Satellite Cells Using Microfluidic Inertial Separation. Tissue Eng Part C Methods, 2018. **24**(1): p. 32-41.

208. Syverud, B.C., M.A. Mycek, and L.M. Larkin, Quantitative, Label-Free Evaluation of Tissue-Engineered Skeletal Muscle Through Multiphoton Microscopy. Tissue Eng Part C Methods, 2017. **23**(10): p. 616-626.

209. Florida, S.E., et al., In vivo structural and cellular remodeling of engineered bone-ligament-bone constructs used for anterior cruciate ligament reconstruction in sheep. Connect Tissue Res, 2016: p. 1-13.

210. Mahalingam, V., et al., Fresh and Frozen Tissue-Engineered Three-Dimensional Bone-Ligament-Bone Constructs for Sheep Anterior Cruciate Ligament Repair Following a 2-Year Implantation. Biores Open Access, 2016. **5**(1): p. 289-298.

211. Ma, J., et al., Morphological and functional characteristics of three-dimensional engineered bone-ligament-bone constructs following implantation. J Biomech Eng, 2009. **131**(10): p. 101017.

212. van Breda, E., et al., Use of the intact mouse skeletal-muscle preparation for metabolic studies. Evaluation of the model. Biochem J, 1990. **267**(1): p. 257-60.

213. Bonen, A., M.G. Clark, and E.J. Henriksen, Experimental approaches in muscle metabolism: hindlimb perfusion and isolated muscle incubations. Am J Physiol, 1994. **266**(1 Pt 1): p. E1-16.

214. Croes, S.A. and C.S. von Bartheld, Measurement of contractile force of skeletal and extraocular muscles: effects of blood supply, muscle size and in situ or in vitro preparation. J Neurosci Methods, 2007. **166**(1): p. 53-65.

215. Larkin, L.M., et al., Skeletal muscle weakness due to deficiency of CuZn-superoxide dismutase is associated with loss of functional innervation. Am J Physiol Regul Integr Comp Physiol, 2011. **301**(5): p. R1400-7.

216. Larkin, L.M., et al., Effect of age and neurovascular grafting on the mechanical function of medial gastrocnemius muscles of Fischer 344 rats. J Gerontol A Biol Sci Med Sci, 1998. **53**(4): p. B252-8.

217. Freed, L.E., I. Martin, and G. Vunjak-Novakovic, Frontiers in tissue engineering. In vitro modulation of chondrogenesis. Clin Orthop Relat Res, 1999(367 Suppl): p. S46-58.

218. Ishaug, S.L., et al., Bone formation by three-dimensional stromal osteoblast culture in biodegradable polymer scaffolds. J Biomed Mater Res, 1997. **36**(1): p. 17-28.

219. Farber, S.J., et al., Reconstructing the Face of War. Mil Med, 2019. **184**(7-8): p. e236-e246.

220. Lee, L., et al., The Burden of Dental Emergencies, Oral-Maxillofacial, and Cranio-Maxillofacial Injuries in US Military Personnel. Mil Med, 2019. **184**(7-8): p. e247-e252.

221. VanSwearingen, J.M., J.F. Cohn, and A. Bajaj-Luthra, Specific impairment of smiling increases the severity of depressive symptoms in patients with facial neuromuscular disorders. Aesthetic Plast Surg, 1999. **23**(6): p. 416-23.

222. Versnel, S.L., et al., Satisfaction with facial appearance and its determinants in adults with severe congenital facial disfigurement: a case-referent study. J Plast Reconstr Aesthet Surg, 2010. **63**(10): p. 1642-9.

223. Happak, W., et al., Human facial muscles: dimensions, motor endplate distribution, and presence of muscle fibers with multiple motor endplates. Anat Rec, 1997. **249**(2): p. 276-84.

224. Harris, K., et al., Metabolic response of skeletal muscle to ischemia. Am J Physiol, 1986. **250**(2 Pt 2): p. H213-20.

225. Labbe, R., T. Lindsay, and P.M. Walker, The extent and distribution of skeletal muscle necrosis after graded periods of complete ischemia. J Vasc Surg, 1987. **6**(2): p. 152-7.

226. Corona, B.T., et al., Implantation of in vitro tissue engineered muscle repair constructs and bladder acellular matrices partially restore in vivo skeletal muscle function in a rat model of volumetric muscle loss injury. Tissue Eng Part A, 2014. **20**(3-4): p. 705-15.

227. Mintz, E.L., et al., Long-Term Evaluation of Functional Outcomes Following Rat Volumetric Muscle Loss Injury and Repair. Tissue Eng Part A, 2020.

228. Novosel, E.C., C. Kleinhans, and P.J. Kluger, Vascularization is the key challenge in tissue engineering. Adv Drug Deliv Rev, 2011. **63**(4-5): p. 300-11.

229. Farris, A.L., A.N. Rindone, and W.L. Grayson, Oxygen Delivering Biomaterials for Tissue Engineering. J Mater Chem B, 2016. **4**(20): p. 3422-3432.

230. Gholipourmalekabadi, M., et al., Oxygen-Generating Biomaterials: A New, Viable Paradigm for Tissue Engineering? Trends Biotechnol, 2016. **34**(12): p. 1010-1021.

231. Badylak, S.F., D. Taylor, and K. Uygun, Whole-organ tissue engineering: decellularization and recellularization of three-dimensional matrix scaffolds. Annu Rev Biomed Eng, 2011. **13**: p. 27-53.

232. Barré-Sinoussi, F. and X. Montagutelli, Animal models are essential to biological research: issues and perspectives. Future Sci OA, 2015. **1**(4): p. FSO63.

233. Randolph, M.E. and G.K. Pavlath, A muscle stem cell for every muscle: variability of satellite cell biology among different muscle groups. Front Aging Neurosci, 2015. **7**: p. 190.

234. Porter, J.D., et al., Distinctive morphological and gene/protein expression signatures during myogenesis in novel cell lines from extraocular and hindlimb muscle. Physiol Genomics, 2006. **24**(3): p. 264-75.

235. Emery, A.E., The muscular dystrophies. Lancet, 2002. **359**(9307): p. 687-95.

236. Wobma, H. and G. Vunjak-Novakovic, Tissue Engineering and Regenerative Medicine 2015: A Year in Review. Tissue Eng Part B Rev, 2016. **22**(2): p. 101-13.

237. Pellegata, A.F., A.M. Tedeschi, and P. De Coppi, Whole Organ Tissue Vascularization: Engineering the Tree to Develop the Fruits. Front Bioeng Biotechnol, 2018. **6**: p. 56.

238. Ahmed, W.W., et al., Myoblast morphology and organization on biochemically micro-patterned hydrogel coatings under cyclic mechanical strain. Biomaterials, 2010. **31**(2): p. 250-8.

239. De Deyne, P.G., Formation of sarcomeres in developing myotubes: role of mechanical stretch and contractile activation. Am J Physiol Cell Physiol, 2000. **279**(6): p. C1801-11.

240. Powell, C.A., et al., Mechanical stimulation improves tissue-engineered human skeletal muscle. Am J Physiol Cell Physiol, 2002. **283**(5): p. C1557-65.

241. Fujita, H., T. Nedachi, and M. Kanzaki, Accelerated de novo sarcomere assembly by electric pulse stimulation in C2C12 myotubes. Exp Cell Res, 2007. **313**(9): p. 1853-65.

242. Jun, I., S. Jeong, and H. Shin, The stimulation of myoblast differentiation by electrically conductive sub-micron fibers. Biomaterials, 2009. **30**(11): p. 2038-47.

243. Syverud, B.C., K.W. VanDusen, and L.M. Larkin, Growth Factors for Skeletal Muscle Tissue Engineering. Cells Tissues Organs, 2016. **202**(3-4): p. 169-179.

244. Liao, I.C., et al., Effect of Electromechanical Stimulation on the Maturation of Myotubes on Aligned Electrospun Fibers. Cell Mol Bioeng, 2008. **1**(2-3): p. 133-145.

245. Wang, L., et al., Nanofiber Yarn/Hydrogel Core-Shell Scaffolds Mimicking Native Skeletal Muscle Tissue for Guiding 3D Myoblast Alignment, Elongation, and Differentiation. ACS Nano, 2015. **9**(9): p. 9167-79.

246. Andorko, J.I. and C.M. Jewell, Designing biomaterials with immunomodulatory properties for tissue engineering and regenerative medicine. Bioeng Transl Med, 2017. **2**(2): p. 139-155.

247. Hotaling, N.A., et al., Biomaterial Strategies for Immunomodulation. Annu Rev Biomed Eng, 2015. **17**: p. 317-49.

248. Vishwakarma, A., et al., Engineering Immunomodulatory Biomaterials To Tune the Inflammatory Response. Trends Biotechnol, 2016. **34**(6): p. 470-482.

249. Dziki, J.L., et al., Extracellular Matrix Bioscaffolds as Immunomodulatory Biomaterials. Tissue Eng Part A, 2017. **23**(19-20): p. 1152-1159.

250. Dziki, J.L., et al., Immunomodulation and Mobilization of Progenitor Cells by Extracellular Matrix Bioscaffolds for Volumetric Muscle Loss Treatment. Tissue Eng Part A, 2016. **22**(19-20): p. 1129-1139.

251. O'Donnell, B.T., et al., Beyond the Present Constraints That Prevent a Wide Spread of Tissue Engineering and Regenerative Medicine Approaches. Front Bioeng Biotechnol, 2019. **7**: p. 95.

252. Tsokas, K., et al., Reducing Risks and Delays in the Translation of Cell and Gene Therapy Innovations into Regulated Products. NAM Perspectives, 2019.

253. National Academies of Sciences, Engineering, and Medicine; Health and Medicine Division; Board on Health Sciences Policy; Forum on Regenerative Medicine; Beachy SH, Wizemann T, Hackmann M, editors. Exploring Sources of Variability Related to the Clinical Translation of Regenerative Engineering Products: Proceedings of a Workshop. Washington (DC): National Academies Press (US); 2019 Mar 21. Addressing Variability in Donor Tissues and Cells. Available from: https://www.ncbi.nlm.nih.gov/books/NBK544028/

254. Knowles, L., W. Luth, and T. Bubela, Paving the road to personalized medicine: recommendations on regulatory, intellectual property and reimbursement challenges. J Law Biosci, 2017. **4**(3): p. 453-506.

255. Haddock, R., et al., Manufacturing Cell Therapies: The Paradigm Shift in Health Care of This Century. NAM Perspectives, 2017.

256. Wong, C.H., K.W. Siah, and A.W. Lo, Estimation of clinical trial success rates and related parameters. Biostatistics, 2019. **20**(2): p. 273-286.